PHYSICAL REVIEW D **108,** 034512 (2023)

Octet baryon isovector charges from $N_f = 2 + 1$ lattice QCD

Gunnar S. Bali,[1,*] Sara Collins,[1,†] Simon Heybrock,[2] Marius Löffler,[1] Rudolf Rödl,[1]
Wolfgang Söldner,[1,‡] and Simon Weishäupl[1,§]

(RQCD Collaboration)

[1]*Institut für Theoretische Physik, Universität Regensburg, 93040 Regensburg, Germany*
[2]*European Spallation Source ERIC, Data Management and Software Centre (DMSC), Box 176, 22100 Lund, Sweden*

(Received 15 May 2023; accepted 7 August 2023; published 29 August 2023)

We determine the axial, scalar and tensor isovector charges of the nucleon, sigma and cascade baryons as well as the difference between the up and down quark masses, $m_u - m_d$. We employ gauge ensembles with $N_f = 2 + 1$ nonperturbatively improved Wilson fermions at six values of the lattice spacing in the range $a \approx (0.039\text{–}0.098)$ fm, generated by the coordinated lattice simulations (CLS) effort. The pion mass M_π ranges from around 430 MeV down to a near physical value of 130 MeV and the linear spatial lattice extent L varies from $6.5M_\pi^{-1}$ to $3.0M_\pi^{-1}$, where $LM_\pi \geq 4$ for the majority of the ensembles. This allows us to perform a controlled interpolation/extrapolation of the charges to the physical mass point in the infinite volume and continuum limit. Investigating SU(3) flavor symmetry, we find moderate symmetry breaking effects for the axial charges at the physical quark mass point, while no significant effects are found for the other charges within current uncertainties.

DOI: 10.1103/PhysRevD.108.034512

I. INTRODUCTION

A charge of a hadron parameterizes the strength of its interaction at small momentum transfer with a particle that couples to this particular charge. For instance, the isovector axial charge determines the β decay rate of the neutron. At the same time, this charge corresponds to the difference between the contribution of the spin of the up quarks minus the spin of the down quarks to the total longitudinal spin of a nucleon in the light front frame that is used in the collinear description of deep inelastic scattering. This intimate connection to spin physics at large virtualities and, more specifically, to the decomposition of the longitudinal proton spin into contributions of the gluon total angular momentum and the spins and angular momenta for the different quark flavors [1,2] opens up a whole area of intense experimental and theoretical research: the first Mellin moment of the helicity structure functions $g_1(x)$ is related to the sum of the individual spins of the quarks within the proton. For lattice determinations of the individual quark contributions to its first and third moments, see, e.g., Refs. [3–8], respectively. Due to the lack of experimental data on $g_1(x)$, in particular at small Bjorken-x, and difficulties in the flavor separation, usually additional information is used in determinations of the helicity parton distribution functions (PDFs) from global fits to experimental data [9–13]. In addition to the axial charge g_A of the proton, this includes information from hyperon decays, in combination with SU(3) flavor symmetry relations whose validity need to be checked.

In this article we establish the size of the corrections to SU(3) flavor symmetry in the axial sector and also for the scalar and the tensor isovector charges of the octet baryons: in analogy to the connection between axial charges and the first moments of helicity PDFs, the tensor charges are related to first moments of transversity PDFs. This was exploited recently in a global fit by the JAM Collaboration [14,15]. Since no tensor or scalar couplings contribute to tree-level Standard Model processes, such interactions may hint at new physics and it is important to constrain new interactions (once discovered) using lattice QCD input, see, e.g., Ref. [16] for a detailed discussion. SU(3) flavor symmetry among the scalar charges is also instrumental regarding recent tensions between different determinations

---

[*] gunnar.bali@ur.de
[†] sara.collins@ur.de
[‡] wolfgang.soeldner@ur.de
[§] simon.weishaeupl@ur.de

of the pion nucleon σ term, see Ref. [17] for a summary of latest phenomenological and lattice QCD results and, e.g., the discussion in Sec. 10 of Ref. [18] about the connection between Okubo-Zweig-Iizuka (OZI) rule violation, (approximate) SU(3) flavor symmetry and the value of the pion nucleon σ term. Finally, the scalar isovector charges relate the QCD part of the mass splitting between isospin partners to the difference of the up and down quark masses.

Assuming SU(3) flavor symmetry, the charges for the whole baryon octet in a given channel only depend on two independent parameters. For the proton and the axial charge, this relation reads $g_A = F_A + D_A$, where in the massless limit F_A and D_A correspond to the chiral perturbation theory (ChPT) low energy constants (LECs) F and D, respectively. Already in the first lattice calculations of the axial charge of the proton [19–21], that were carried out in the quenched approximation, F_A and D_A have been determined separately. However, in spite of the long history of nucleon structure calculations, SU(3) flavor symmetry breaking is relatively little explored using lattice QCD: only very few investigations of axial charges of the baryon octet exist to date [22–26] and only one of these includes the scalar and tensor charges [26]. Here we compute these charges for the light baryon octet. We also predict the difference between the up and down quark masses, the QCD contributions to baryon isospin mass splittings and isospin differences of pion baryon σ terms.

This article is organized as follows. In Sec. II we define the octet baryon charges and some related quantities of interest. In Sec. III the lattice setup is described, including the gauge ensembles employed, the computational methods used to obtain two- and three-point correlation functions and the excited state analysis performed to extract the ground state matrix elements of interest. We continue with details on the nonperturbative renormalization and order a improvement, before explaining our infinite volume, continuum limit and quark mass extrapolation strategy. Our results for the charges in the infinite volume, continuum limit at physical quark masses are then presented in Sec. IV. Subsequently, in Sec. V we discuss SU(3) symmetry breaking effects, determine the up and down quark mass difference from the scalar charge of the Σ baryon, split isospin breaking effects on the baryon masses into QCD and QED contributions and determine isospin breaking corrections to the pion baryon σ terms. Throughout this section we also compare our results to literature values, before we give a summary and an outlook in Sec. VI. In the appendices further details regarding the stochastic three-point function method are given and additional data tables and figures are provided.

II. OCTET BARYON CHARGES

All light baryons (i.e., baryons without charm or bottom quarks) with strangeness $S < 0$, i.e., with a net difference between the numbers of strange (s) antiquarks and quarks are usually called hyperons. The spin-1/2 baryon octet, depicted in Fig. 1, contains the nucleons $N \in \{p, n\}$, besides the $S = -1$ hyperons Λ^0 and $\Sigma \in \{\Sigma^+, \Sigma^0, \Sigma^-\}$ and the $S = -2$ hyperons $\Xi \in \{\Xi^0, \Xi^-\}$ (cascades). We assume isospin symmetry $m_\ell = m_u = m_d$, where m_ℓ corresponds to the average mass of the physical up (u) and down (d) quarks. In this case, the baryon masses within isomultiplets are degenerate and simple relations exist between matrix elements that differ in terms of the isospin I_3 of the baryons and of the local operator (current).

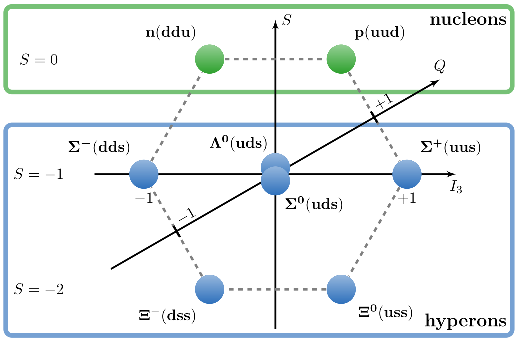

FIG. 1. The spin-1/2 baryon octet where S, I_3 and $Q = (1 + S)/2 + I_3$ label strangeness, isospin and charge, respectively.

Baryon charges $g_J^{B'B}$ are obtained from matrix elements of the form

$$\langle B'(p', s')|\bar{u}\Gamma_J d|B(p, s)\rangle = g_J^{B'B}\bar{u}_{B'}(p', s')\Gamma_J u_B(p, s) \tag{1}$$

at zero four-momentum transfer $q^2 = (p' - p)^2 = 0$. Above, $u_B(p, s)$ denotes the Dirac spinor of a baryon B with four momentum p and spin s. We restrict ourselves to $\Delta I_3 = 1$ transitions within the baryon octet. In this case $p' = p$, since in isosymmetric QCD $m_{B'} = m_B$, and it is sufficient to set $\mathbf{p} = \mathbf{0}$. Rather than using the above $I_3 = 1$ currents $\bar{u}\Gamma_J d$ (where the vector and axial currents couple to the W^- boson), it is convenient to define $I_3 = 0$ isovector currents,

$$\mathcal{O}_J(x) = \bar{u}(x)\Gamma_J u(x) - \bar{d}(x)\Gamma_J d(x), \tag{2}$$

and the corresponding charges g_J^B,

$$\langle B(p, s)|\mathcal{O}_J|B(p, s)\rangle = g_J^B \bar{u}_B(p, s)\Gamma_J u_B(p, s), \tag{3}$$

which, in the case of isospin symmetry, are trivially related to the $g_J^{B'B}$:

$$g_J^N \coloneqq g_J^p = g_J^{pn}, \tag{4}$$

$$g_J^\Sigma \coloneqq g_J^{\Sigma^+} = -\sqrt{2} g_J^{\Sigma^+\Sigma^0}, \tag{5}$$

$$g_J^\Xi \coloneqq g_J^{\Xi^0} = -g_J^{\Xi^0\Xi^-}. \tag{6}$$

Note that we do not include the Λ baryon here since in this case the isovector combination trivially gives zero. We consider vector (V), axial-vector (A), scalar (S) and tensor (T) operators which are defined through the Dirac matrices $\Gamma_J = \gamma_4, \gamma_i\gamma_5, \mathbb{1}, \sigma_{ij}$ for $J \in \{V, A, S, T\}$, with $\sigma_{\mu\nu} = \frac{1}{2}[\gamma_\mu, \gamma_\nu]$, where $i, j \in \{1, 2, 3\}$ and $i < j$.

The axial charges in the $m_s = m_\ell = 0$ chiral limit are important parameters in SU(3) ChPT and enter the expansion of every baryonic quantity. These couplings can be decomposed into two LECs F and D which appear in the first order meson-baryon Lagrangian for three light quark flavors (see, e.g., Ref. [27]):

$$g_A^N = F + D, \qquad g_A^\Sigma = 2F, \qquad g_A^\Xi = F - D. \tag{7}$$

Due to group theoretical constraints, see, e.g., Refs. [28,29], such a decomposition also holds for $m_s = m_\ell > 0$, for the axial as well as for the other charges. We define for $m = m_s = m_\ell$

$$g_J^N(m) = F_J(m) + D_J(m), \tag{8}$$

$$g_J^\Sigma(m) = 2F_J(m), \tag{9}$$

$$g_J^\Xi(m) = F_J(m) - D_J(m), \tag{10}$$

where $F = F_A(0)$, $D = D_A(0)$. The vector Ward identity (conserved vector current, CVC relation) implies that $g_V^N = g_V^\Xi = F_V = 1$ and $g_V^\Sigma = 2F_V$, i.e., in this case the above relations also hold for $m_s \neq m_\ell$, with $F_V(m) = 1$ and $D_V(m) = 0$.

In this article we determine the charges at many different positions in the quark mass plane and investigate SU(3) flavor symmetry breaking, i.e., the extent of violation of Eqs. (8)–(10). Due to this, other than for $J \neq V$ where $D_V/F_V = 0$, the functions $D_J(m)$ and $F_J(m)$ are not uniquely determined at the physical point, where $m_s \gg m_\ell$. At this quark mass point we will find the approximate ratios $D_A/F_A \approx (1.55 - 1.95)$, $D_S/F_S \approx -(0.2 - 0.5)$ and $D_T/F_T \approx 1.5$. The first ratio can be compared to the SU(6) quark model expectation $D_A(m)/F_A(m) = 3/2$ (see, e.g., Ref. [30]), which is consistent with the large-N_c limit [31].

III. LATTICE SETUP

In this section we present the details of our lattice setup. First, we describe the gauge ensembles employed and the construction of the correlation functions. The computation of the three-point correlation functions via a stochastic approach is briefly discussed. Following this, we present the fitting analysis and treatment of excited state contributions employed to extract the ground state baryon matrix elements. The renormalization factors used to match to the continuum $\overline{\text{MS}}$ scheme and the improvement factors utilized to ensure leading $O(a^2)$ discretization effects are then given. Finally, the strategy for interpolation/extrapolation to the physical point in the infinite volume and continuum limit is outlined.

A. Gauge ensembles

We employ ensembles generated with $N_f = 2 + 1$ flavors of nonperturbatively $\mathcal{O}(a)$ improved Wilson fermions and a tree-level Symanzik improved gauge action, which were mostly produced within the coordinated lattice simulations (CLS) [32] effort. Either periodic or open boundary conditions in time [33] are imposed, where the latter choice is necessary for ensembles with $a < 0.06$ fm in order to avoid freezing of the topological charge and thus to ensure ergodicity [34]. The hybrid Monte Carlo (HMC) simulations are stabilized by introducing a twisted mass term for the light quarks [35], whereas the strange quark is included via the rational hybrid Monte Carlo (RHMC) algorithm [36]. The modifications of the target action are corrected for by applying the appropriate reweighting, see Refs. [17,32,37] for further details.

In total 47 ensembles were analyzed spanning six lattice spacings a in the range $0.039\ \text{fm} \lesssim a \lesssim 0.098$ fm, with pion masses between 430 MeV and 130 MeV (below the physical pion mass), as shown in Fig. 2. The lattice spatial extent L is kept sufficiently large, where $LM_\pi \geq 4$ for the majority of the ensembles. A limited number of smaller volumes are employed to enable finite volume effects to be investigated, with the spatial extent varying across all the ensembles in the range $3.0 \leq LM_\pi \leq 6.5$. Further details are given in Table I. The ensembles lie along three trajectories in the quark mass plane, as displayed in Fig. 3:

(i) The symmetric line: the light and strange quark masses are degenerate ($m_\ell = m_s$) and SU(3) flavor symmetry is exact.
(ii) The $\operatorname{tr} M =$ const line: starting at the $m_\ell = m_s$ flavor symmetric point, the trajectory approaches the physical point holding the trace of the quark mass matrix ($2m_\ell + m_s$, i.e., the flavor averaged quark mass) constant such that $2M_K^2 + M_\pi^2$ is close to its physical value.
(iii) The $m_s =$ const line: the renormalized strange quark mass is kept near to its physical value [38].

The latter two trajectories intersect close to the physical point, whereas the symmetric line approaches the SU(3) chiral limit. In figures where data from different lines are shown, we will distinguish these, employing the symbol shapes of Fig. 2 (triangle, circle, diamond). The excellent coverage of the quark mass plane enables the interpolation/extrapolation of the results for the charges to the physical point to be tightly constrained. In addition, considering the wide range of lattice spacings and spatial volumes and the high statistics available for most ensembles, all sources of systematic uncertainty associated with simulating at unphysical quark mass, finite lattice spacing and finite

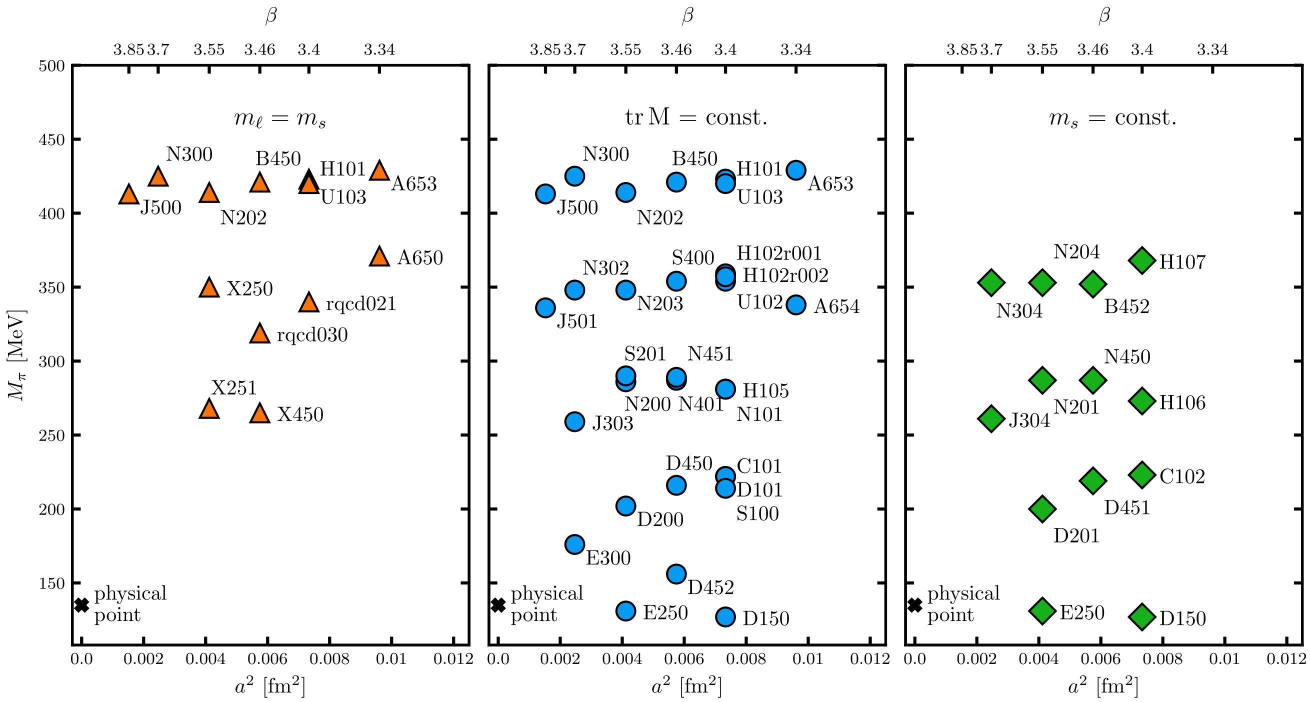

FIG. 2. Parameter landscape of the ensembles listed in Table I. The ensembles are grouped according to the three quark mass trajectories (see the text and Fig. 3): (left) the symmetric line ($m_\ell = m_s$), (middle) the tr M = const line and (right) the m_s = const line.

TABLE I. List of the gauge ensembles analyzed in this work. The rqcd `xyz` ensembles were generated by the RQCD group using the BQCD code [39], whereas all other ensembles were created within the CLS effort. Note that for H102 there are two replicas. These have the same parameters but were generated with slightly different algorithmic setups and, therefore, have to be analyzed separately. N401 and N451 differ in terms of the boundary conditions (bc) imposed in the time direction (open (o) and antiperiodic (p), respectively). The lattice spacings a are determined in Ref. [17]. In the second to last column t denotes the source-sink separation of the connected three-point functions. The subscript (superscript) given for each separation indicates the number of measurements performed using the sequential source (stochastic) method on each configuration (see Secs. III B and III C). The last column gives N_{cnfg}, the number of configurations analyzed.

Ensemble	β	a [fm]	Trajectory	bc	$N_t \times N_s^3$	M_π [MeV]	M_K [MeV]	LM_π	t/a	N_{cnfg}
A650	3.34	0.098	sym	p	$48 \cdot 24^3$	371	371	4.43	$7_3, 9_3, 11_3, 13_4$	5062
A653			tr M/sym	p	$48 \cdot 24^3$	429	429	5.12	$7_3, 9_3, 11_3, 13_4$	2525
A654			tr M	p	$48 \cdot 24^3$	338	459	4.04	$7_3^2, 9_3^2, 11_3^2, 13_4^2$	2533
rqcd021	3.4	0.086	sym	p	$32 \cdot 32^3$	340	340	4.73	$8_2, 10_2, 12_4, 14_4$	1541
H101			tr M/sym	o	$96 \cdot 32^3$	423	423	5.88	$8_2, 10_2, 12_2, 14_2$	2000
U103			tr M/sym	o	$128 \cdot 24^3$	420	420	4.38	$8_1, 10_2, 12_3, 14_4$	2470
H102r001			tr M	o	$96 \cdot 32^3$	354	442	4.92	$8_1^4, 10_2^4, 12_3^4, 14_4^4$	997
H102r002			tr M	o	$96 \cdot 32^3$	359	444	4.99	$8_1^4, 10_2^4, 12_3^4, 14_4^4$	1000
U102			tr M	o	$128 \cdot 24^3$	357	445	3.72	$8_1, 10_2, 12_3, 14_4$	2210
N101			tr M	o	$128 \cdot 48^3$	281	467	5.86	$8_1, 10_2, 12_3, 14_4$	1457
H105			tr M	o	$96 \cdot 32^3$	281	468	3.91	$8_1^2, 10_2^2, 12_3^2, 14_4^2$	2038
D101			tr M	o	$128 \cdot 64^3$	222	476	6.18	$8_1, 10_2, 12_3, 14_4$	608
C101			tr M	o	$96 \cdot 48^3$	222	476	4.63	$8_1^2, 10_2^2, 12_3^2, 14_4^2$	2000
S100			tr M	o	$128 \cdot 32^3$	214	476	2.98	$8_1, 10_2, 12_3, 14_4$	983
D150			tr M/ms	p	$128 \cdot 64^3$	127	482	3.53	$8_1, 10_2, 12_3, 14_4$	603
H107			ms	o	$96 \cdot 32^3$	368	550	5.12	$8_2^2, 10_2^2, 12_3^2, 14_4^2$	1564
H106			ms	o	$96 \cdot 32^3$	273	520	3.80	$8_2^4, 10_2^4, 12_3^4, 14_4^4$	1553
C102			ms	o	$96 \cdot 48^3$	223	504	4.65	$8_2^4, 10_2^4, 12_3^4, 14_4^4$	1500

(Table continued)

TABLE I. *(Continued)*

Ensemble	β	a [fm]	Trajectory	bc	$N_t \times N_s^3$	M_π [MeV]	M_K [MeV]	LM_π	t/a	N_{cnfg}
rqcd030	3.46	0.076	sym	p	$64 \cdot 32^3$	319	319	3.93	$9_4, 11_4, 13_8, 16_8$	1224
X450			sym	p	$64 \cdot 48^3$	265	265	4.90	$9_2, 11_2, 13_4, 16_4$	400
B450			tr M/sym	p	$64 \cdot 32^3$	421	421	5.19	$9_3, 11_3, 14_3, 16_4$	1612
S400			tr M	o	$128 \cdot 32^3$	354	445	4.36	$9_1^2, 11_2^2, 13_3, 14^2, 16_4^2$	2872
N451			tr M	p	$128 \cdot 48^3$	289	466	5.34	$9_4^4, 11_4^4, 13_4, 14^4, 16_4^4$	1011
N401			tr M	o	$128 \cdot 48^3$	287	464	5.30	$9_1^2, 11_2^2, 13_3, 14^2, 16_4^2$	1086
D450			tr M	p	$128 \cdot 64^3$	216	480	5.32	$9_4^2, 11_4^2, 13_4, 14^2, 16_4^2$	621
D452			tr M	p	$128 \cdot 64^3$	156	488	3.84	$9^4, 11^4, 14^4, 16^4$	1000
B452			ms	p	$64 \cdot 32^3$	352	548	4.34	$9_3^2, 11_3^2, 13_3, 14^2, 16_4^2$	1944
N450			ms	p	$128 \cdot 48^3$	287	528	5.30	$9_4^2, 11_4^2, 13_4, 14^2, 16_4^2$	1132
D451			ms	p	$128 \cdot 64^3$	219	507	5.39	$9_4^2, 11_4^2, 13_4, 14^2, 16_4^2$	458
X250	3.55	0.064	sym	p	$64 \cdot 48^3$	350	350	5.47	$11_2, 14_2, 16_4, 19_4$	1493
X251			sym	p	$64 \cdot 48^3$	268	268	4.19	$11_4, 14_4, 16_8, 19_8$	1474
N202			tr M/sym	o	$128 \cdot 48^3$	414	414	6.47	$11_1, 14_2, 16_2, 19_4$	883
N203			tr M	o	$128 \cdot 48^3$	348	445	5.44	$11_1^4, 14_2^4, 16_3^4, 19_4^4$	1543
N200			tr M	o	$128 \cdot 48^3$	286	466	4.47	$11_1^4, 14_2^4, 16_3^4, 19_4^4$	1712
S201			tr M	o	$128 \cdot 32^3$	290	471	3.02	$11_1, 14_2, 16_3, 19_4$	2092
D200			tr M	o	$128 \cdot 64^3$	202	484	4.21	$11_1^2, 14_2^2, 16_3^2, 19_4^2$	2001
E250			tr M/ms	p	$192 \cdot 96^3$	131	493	4.10	$11_4, 14_4, 16_4, 19_4$	490
N204			ms	o	$128 \cdot 48^3$	353	549	5.52	$11_2^2, 14_2^2, 16_3^2, 19_4^2$	1500
N201			ms	o	$128 \cdot 48^3$	287	527	4.49	$11_2^2, 14_2^2, 16_3^2, 19_4^2$	1522
D201			ms	o	$128 \cdot 64^3$	200	504	4.17	$11_1^4, 14_2^4, 16_3^4, 19_4^4$	1078
N300	3.7	0.049	tr M/sym	o	$128 \cdot 48^3$	425	425	5.15	$14_1, 17_2, 21_2, 24_4$	1539
N302			tr M	o	$128 \cdot 48^3$	348	455	4.21	$14_1^2, 17_2^2, 21_3^2, 24_4^2$	1383
J303			tr M	o	$192 \cdot 64^3$	259	479	4.18	$14_2^2, 17_4^2, 21_6^2, 24_8^2$	998
E300			tr M	o	$192 \cdot 96^3$	176	496	4.26	$14_3^2, 17_3^2, 21_6^2, 24_6^2$	1038
N304			ms	o	$128 \cdot 48^3$	353	558	4.27	$14_2^2, 17_2^2, 21_3^2, 24_4^2$	1652
J304			ms	o	$192 \cdot 64^3$	261	527	4.21	$14_3^2, 17_3^2, 21_3^2, 24_4^2$	1630
J500	3.85	0.039	tr M/sym	o	$192 \cdot 64^3$	413	413	5.24	$17_1, 22_2, 27_3, 32_4$	1837
J501			tr M	o	$192 \cdot 64^3$	336	448	4.26	$17_1^2, 22_2^2, 27_3^2, 32_4^2$	1018

volume can be investigated. Our strategy for performing a simultaneous continuum, quark mass and infinite volume extrapolation is given in Sec. III F.

B. Correlation functions

The baryon octet charges are extracted from two- and three-point correlation functions of the form

$$C_{\text{2pt}}^{B}(t) = \mathcal{P}_{+}^{\alpha\beta} \sum_{\mathbf{x}'} \langle \mathcal{B}_\alpha(\mathbf{x}', t) \bar{\mathcal{B}}_\beta(\mathbf{0}, 0) \rangle, \tag{11}$$

$$C_{\text{3pt}}^{B}(t, \tau) = \mathcal{P}^{\alpha\beta} \sum_{\mathbf{x}', \mathbf{y}} \langle \mathcal{B}_\alpha(\mathbf{x}', t) \mathcal{O}_J(\mathbf{y}, \tau) \bar{\mathcal{B}}_\beta(\mathbf{0}, 0) \rangle. \tag{12}$$

Spin-1/2 baryon states are created (annihilated) using suitable interpolators $\bar{\mathcal{B}}$ ($\mathcal{B}$): for the nucleon, Σ and Ξ, we employ interpolators corresponding to the proton, Σ^+ and Ξ^0, respectively,

$$N_\alpha = \epsilon^{ijk} u_\alpha^i (u^{jT} C \gamma_5 d^k), \tag{13}$$

$$\Sigma_\alpha = \epsilon^{ijk} u_\alpha^i (s^{jT} C \gamma_5 u^k), \tag{14}$$

$$\Xi_\alpha = \epsilon^{ijk} s_\alpha^i (s^{jT} C \gamma_5 u^k), \tag{15}$$

with spin index α, color indices i, j, k and C being the charge conjugation matrix. The Λ baryon is not considered here since three-point functions with the currents $\mathcal{O}_J = \bar{u}\Gamma_J u - \bar{d}\Gamma_J d$ vanish in this case. Without loss of generality, we place the source space-time position at the origin (0, 0) and the sink at $(\mathbf{x}', t)$ such that the source-sink separation in time equals t. The current is inserted at $(\mathbf{y}, \tau)$ with $0 \le \tau \le t$.[1] The annihilation interpolators are projected onto zero-momentum via the sums over the spatial sink

---

[1] Note that in practice we only analyze data with $2a \le \tau \le t - 2a$.

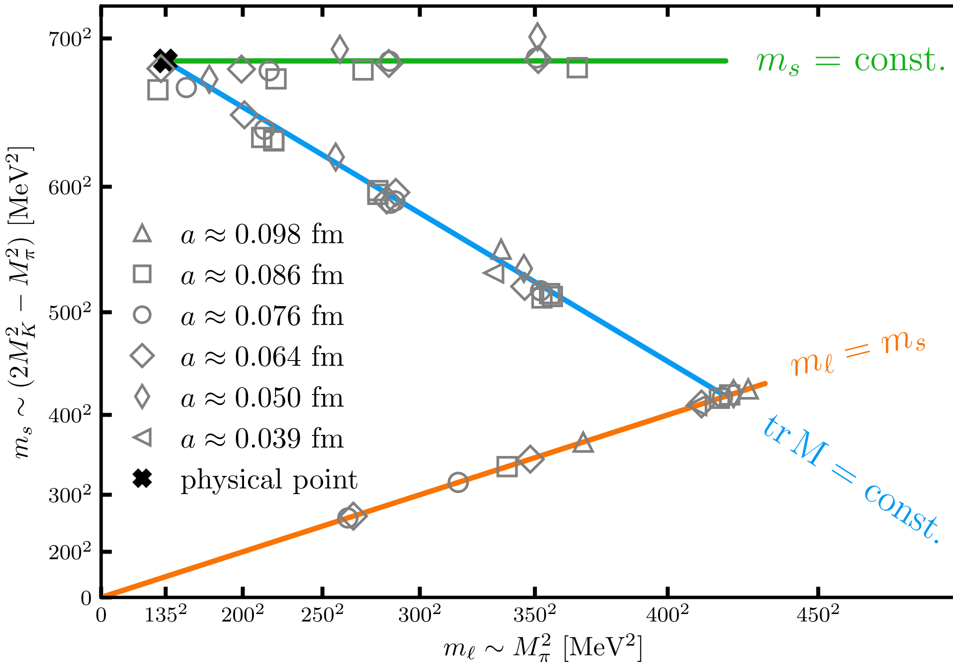

FIG. 3. Position of the ensembles in the quark mass plane. The tr M = const line (indicated as a blue line) and m_s = const line (green line) intersect close to the physical point (black cross). The symmetric line (orange line), which approaches the SU(3) chiral limit, crosses the tr M = const line around $M_\pi = 411$ MeV.

position, while momentum conservation (and the sum over $\mathbf{y}$ for the current) means the source is also at rest.

We ensure positive parity via the projection operator $\mathcal{P}_+ = \frac{1}{2}(\mathbb{1} + \gamma_4)$. For the three-point functions, $\mathcal{P} = \mathcal{P}_+$ for $J = V$, S and $\mathcal{P} = i\gamma_i\gamma_5\mathcal{P}_+$ for $J = A$, T. The latter corresponds to taking the difference of the polarizations (in the i direction). The interpolators are constructed from spatially extended quark fields in order to increase the overlap with the ground state of interest and minimize contributions to the correlation functions from excited states. Wuppertal smearing is employed [20], together with APE-smeared [40] gauge transporters. The number of smearing iterations is varied with the aim of ensuring that ground state dominance sets in for moderate time separations. The root mean squared light quark smearing radii range from about 0.6 fm (for $M_\pi \approx 430$ MeV) up to about 0.8 fm (for $M_\pi \approx 130$ MeV), whereas the strange quark radii range from about 0.5 fm (for the physical strange quark mass) up to about 0.7 fm (for $M_K = M_\pi \approx 270$ MeV). See Sec. E.1 (and in particular Table 15) of Ref. [17] for further details. Figure 4 demonstrates that, when keeping for similar pion and kaon masses the smearing radii fixed in physical units, the ground state dominates the two-point functions at similar physical times across different lattice spacings.

Performing the Wick contractions for the two- and three-point correlation functions leads to the connected quark-line diagrams displayed in Fig. 5. Note that there are no disconnected quark-line diagrams for the three-point functions as these cancel when forming the isovector flavor combination of the current. The two-point functions are constructed in the standard way using point-to-all propagators. For the three-point functions either a stochastic approach (described in the next subsection) or the sequential source method [41] (on some ensembles in combination with the coherent sink technique [42]) is employed. The stochastic approach provides a computationally cost efficient way of evaluating the three-point functions for the whole of the baryon octet, however, additional noise is introduced. The relevant measurements for the nucleon (which has the worst signal-to-noise ratio of the octet) have already been performed with the sequential source method as part of other projects by our group, see, e.g., Ref. [43]. We use these data in our analysis and the stochastic approach for the correlation functions of the Σ and the Ξ baryons. Note that along the symmetric line ($m_\ell = m_s$) the hyperon three-point functions can be obtained as linear combinations of the contractions carried out for the currents $\bar{u}\Gamma_J u$ and $\bar{d}\Gamma_J d$ within the proton. Therefore, no stochastic three-point functions are generated in these cases.

We typically realize four source-sink separations with $t/\text{fm} \approx \{0.7, 0.8, 1.0, 1.2\}$ in order to investigate excited state contamination and reliably extract the ground state baryon octet charges. Details of our fitting analysis are presented in Sec. III D. Multiple measurements are performed per configuration, in particular for the larger source-sink separations to improve the signal, see Table I. The source positions are chosen randomly on each configuration in order to reduce autocorrelations. On ensembles with open boundary conditions in time only

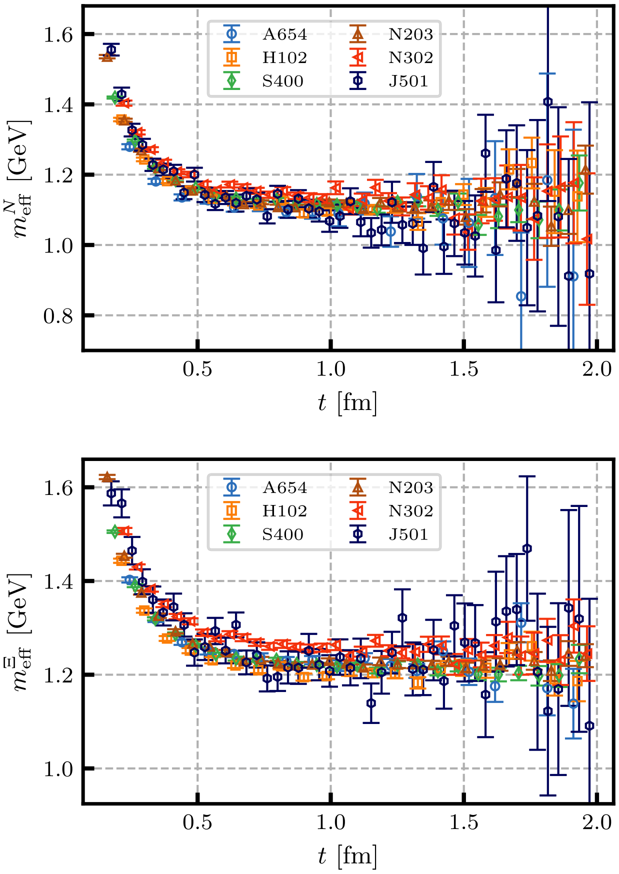

FIG. 4. Effective masses $m^B_{\rm eff}(t) = \ln[C^B_{\rm 2pt}(t-\frac{a}{2})/C^B_{\rm 2pt}(t+\frac{a}{2})]/a$ of the nucleon (top) and Ξ (bottom) determined on ensembles with $M_\pi \approx 340$ MeV and $M_K \approx 450$ MeV and lattice spacings ranging from $a = 0.098$ fm (ensemble A654) down to $a = 0.039$ fm (ensemble J501). The errors of $m^B_{\rm eff}(t)$ are expected to increase in proportion to a^{-1} but they also vary, e.g., with the number of effectively independent ensembles analyzed.

the spatial positions are varied and the source and sink time slices are restricted to the bulk of the lattice (sufficiently away from the boundaries), where translational symmetry is effectively restored.

C. Stochastic three-point correlation functions

In the following, we describe the construction of the connected three-point correlation functions using a computationally efficient stochastic approach. This method was introduced for computing meson three-point functions in Ref. [44] and utilized for baryons in Refs. [45,46] and also for mesons in Refs. [47,48]. Similar stochastic approaches have been implemented by other groups, see, e.g., Refs. [49,50].

In Fig. 5 the quark-line diagram for the three-point function contains an all-to-all quark propagator which connects the current insertion at time τ with the baryon sink at time t. The all-to-all propagator is too computationally expensive to evaluate exactly. One commonly used approach avoids directly calculating the propagator by constructing a sequential source [41] which depends on the baryon sink interpolator (including its temporal position and momentum). This method has the disadvantage that one needs to compute a new quark propagator for each source-sink separation, sink momentum and baryon sink interpolator. Alternatively, one can estimate the all-to-all propagator stochastically. This introduces additional noise on top of the gauge noise, however, the quark-line diagram can be computed in a very efficient way. The stochastic approach allows one to factorize the three-point correlation function into a "spectator" and an "insertion" part which can be computed and stored independently with all spin indices and one color index open. This is illustrated in Fig. 6 and explained in more detail below. The two parts can be contracted at a later (postprocessing) stage with the appropriate spin and polarization matrices, such that arbitrary baryonic interpolators can be realized, making this method ideal for SU(3) flavor symmetry studies.

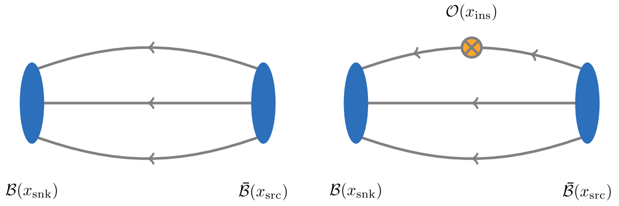

FIG. 5. Quark-line diagrams of the two-point (left) and connected three-point (right) correlation functions where $x_{\rm src} = (\mathbf{0}, 0)$, $x_{\rm ins} = (\mathbf{y}, \tau)$ and $x_{\rm snk} = (\mathbf{x}', t)$.

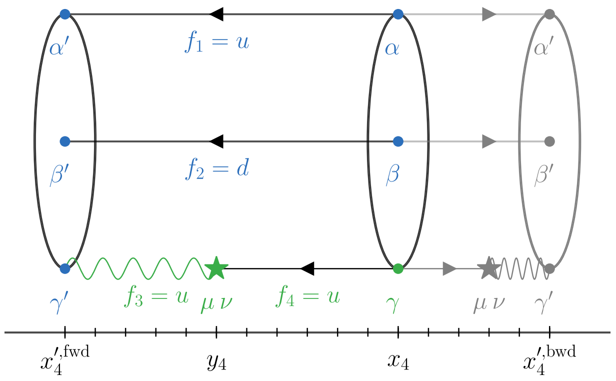

FIG. 6. Schematic representation of the forward (left) and backward (right, shown in gray) propagating three-point correlation functions with open spin indices that are computed simultaneously with the stochastic approach. The indices corresponding to the spectator and insertion part from the factorization in Eq. (21) are color-coded in blue and green, respectively. The black solid lines correspond to the standard point-to-all propagators, whereas the green wiggly lines represent stochastic time slice-to-all propagators. The temporal positions of the forward/backward sink, insertion and source are labeled as $x_4^{\prime,\rm fwd|bwd}$, y_4 and x_4, respectively. The flavor indices are chosen corresponding to a nucleon three-point function with a $\bar{u}\Gamma_J u$-current insertion.

Furthermore, no additional inversions are needed for different sink momenta.

As depicted in Fig. 7, we simultaneously compute the three-point functions for a baryon propagating (forwards) from source time slice x_4 to sink time slice $x_4^{\prime,\mathrm{fwd}}$ and propagating (backwards) from x_4 to $x_4^{\prime,\mathrm{bwd}}$. We start with the definition of the stochastic source and solution vectors which can be used to construct the time slice-to-all propagator (shown as a green wiggly line in Fig. 6). In the following $i \in \{1, \ldots, N_{\mathrm{sto}}\}$ is the "stochastic index," we denote spin indices with Greek letters, color indices with Latin letters (other than f or i) and we use flavor indices $f_n \in \{u, d, s\}$. We introduce (time partitioned) complex $\mathbb{Z}_2$ noise vectors [51,52]

$$\eta_i(x)^\alpha_a = \begin{cases} (\mathbb{Z}_2 \otimes \mathrm{i}\mathbb{Z}_2)/\sqrt{2} & \text{if } x_4 = x_4^{\prime,\mathrm{fwd}|\mathrm{bwd}}, \\ 0 & \text{otherwise,} \end{cases} \tag{16}$$

where the noise vector has support on time slices $x_4^{\prime,\mathrm{fwd}}$ and $x_4^{\prime,\mathrm{bwd}}$. The noise vectors have the properties

$$\frac{1}{N_{\mathrm{sto}}} \sum_{i=1}^{N_{\mathrm{sto}}} \eta_i(x)^\alpha_a = \mathcal{O}\left(\frac{1}{\sqrt{N_{\mathrm{sto}}}}\right), \tag{17}$$

$$\frac{1}{N_{\mathrm{sto}}} \sum_{i=1}^{N_{\mathrm{sto}}} \eta_i(x)^\alpha_a \eta_i^*(y)^\beta_b = \delta_{xy}\delta_{\alpha\beta}\delta_{ab} + \mathcal{O}\left(\frac{1}{\sqrt{N_{\mathrm{sto}}}}\right). \tag{18}$$

The solution vectors $s_{f,i}(y)$ are defined through the linear system

$$D_f(x, y)^{\alpha\beta}_{ab} s_{f,i}(y)^\beta_b = \eta_i(x)^\alpha_a, \tag{19}$$

where we sum over repeated indices (other than f) and $D_f(x, y)^{\alpha\beta}_{ab}$ is the Wilson-Dirac operator for the quark flavor f. Note that $s_{u,i} = s_{d,i}$ since our light quarks are mass-degenerate.

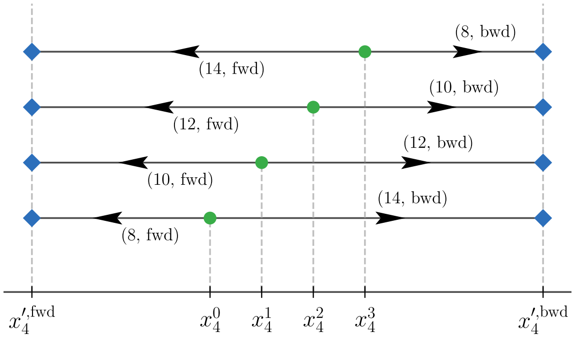

FIG. 7. Sketch of the source and sink positions of the three-point functions realized using the stochastic approach. Blue diamonds depict the position of the forward ($x_x^{\prime,\mathrm{fwd}}$) and backward ($x_x^{\prime,\mathrm{bwd}}$) sink time slices. Green points correspond to the source time slices x_4^k for $k = 0, 1, 2, 3$. Each three-point function measurement is labeled by the source-sink separation, where the values given correspond to the setup for the ensembles at $\beta = 3.40$.

Using γ_5-Hermiticity ($\gamma_5 D_f \gamma_5 = D_f^\dagger$) and the properties given in Eqs. (17) and (18), the time slice-to-all propagator connecting all points of the (forward and backward) sink time slices x_4' to all points of any insertion time slice y_4 can be estimated as

$$G_{f_3}(x', y)^{\gamma'\mu}_{c'd} \approx \frac{1}{N_{\mathrm{sto}}} \sum_{i=1}^{N_{\mathrm{sto}}} [\gamma_5 \eta_i(x')]^{\gamma'}_{c'} [\gamma_5 s^*_{f_3}(y)]^\mu_d. \tag{20}$$

Combining this time slice-to-all propagator with point-to-all propagators for the source position x_4, the baryonic three-point correlation functions Eq. (12) can be factorized as visualized in Fig. 6 into a spectator part (S) and an insertion part (I), leaving all flavor and spin indices open:

$$\begin{aligned} &C_{\mathrm{3pt}}(\mathbf{p}', \mathbf{q}|x_4', y_4, x_4)^{\alpha'\alpha\beta'\beta\gamma'\mu\nu\gamma}_{f_1 f_2 f_3 f_4} \\ &\quad\approx \frac{1}{N_{\mathrm{sto}}} \sum_{i=1}^{N_{\mathrm{sto}}} \sum_{c=1}^{3} (S_{f_1 f_2}(\mathbf{p}', x_4', x_4)^{\alpha'\alpha\beta'\beta\gamma'}_{ic} \\ &\qquad \times I_{f_3 f_4}(\mathbf{q}, y_4, x_4)^{\mu\nu\gamma}_{ic}). \end{aligned} \tag{21}$$

The spectator and insertion parts are defined as

$$\begin{aligned} &S_{f_1 f_2}(\mathbf{p}', x_4', x_4)^{\alpha'\alpha\beta'\beta\gamma'}_{ic} \\ &\quad\coloneqq \sum_{\mathbf{x}'} (\epsilon_{a'b'c'}\epsilon_{abc} G_{f_1}(x', x)^{\alpha'\alpha}_{a'a} G_{f_2}(x', x)^{\beta'\beta}_{b'b} \\ &\qquad \times [\gamma_5 \eta_i(x')]^{\gamma'}_{c'} e^{-\mathrm{i}\mathbf{p}'\cdot(\mathbf{x}'-\mathbf{x})}), \end{aligned} \tag{22}$$

$$\begin{aligned} &I_{f_3 f_4}(\mathbf{q}, y_4, x_4)^{\mu\nu\gamma}_{ic} \\ &\quad\coloneqq \sum_{\mathbf{y}} [\gamma_5 s^*_{f_3,i}(y)]^\mu_d G_{f_4}(y, x)^{\nu\gamma}_{dc} e^{+\mathrm{i}\mathbf{q}\cdot(\mathbf{y}-\mathbf{x})}. \end{aligned} \tag{23}$$

Using these building blocks, three-point functions for given baryon interpolators and currents for any momentum combination can be constructed. Note that in this article we restrict ourselves to the case $\mathbf{q} = \mathbf{p}' = \mathbf{0}$. The point-to-all propagators within the spectator part are smeared at the source and at the sink, whereas G_{f_4} is only smeared at the source. The stochastic source is smeared too, however, this is carried out after solving Eq. (19). In principle, the spectator part also depends on f_3 because for $f_3 = s$ and $f_3 \in \{u, d\}$ different smearing parameters are used. We ignore the dependence of the spectator part on f_3 since here we restrict ourselves to $f_3, f_4 \in \{u, d\}$. For details on the smearing see the previous subsection. Using the same set of time slice-to-all propagators, we compute point-to-all propagators for a number of different source positions at time slices x_4 in-between $x_4^{\prime,\mathrm{bwd}}$ and $x_4^{\prime,\mathrm{fwd}}$ which allows us to vary the source-sink distances, see Figs. 6 and 7.

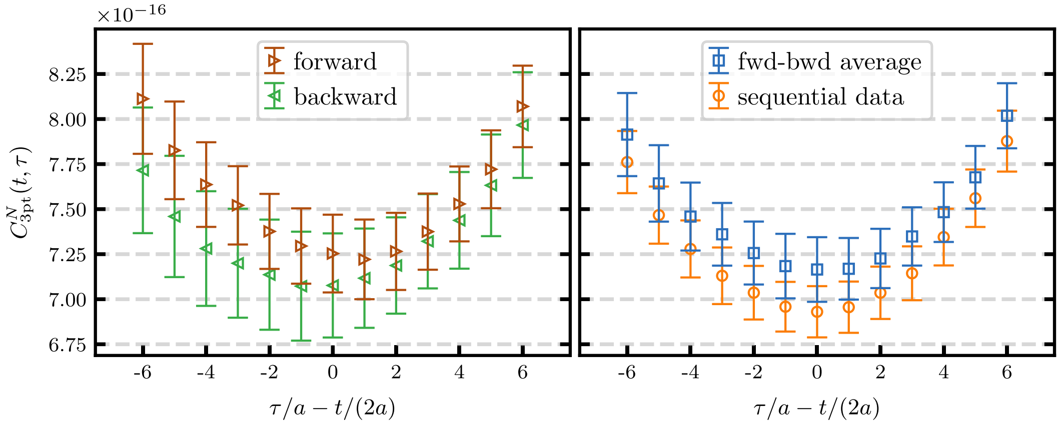

FIG. 8. Left: polarized nucleon three-point correlation function propagating in the forward and backward directions for a $\bar{u}\gamma_y\gamma_z u$ current insertion obtained from one stochastic measurement on ensemble N200 ($a = 0.064$ fm). Note that two different source positions were needed to obtain the same source-sink separation $t = 14a$ in the two directions, see Fig. 7. Right: forward-backward average of the stochastic three-point function shown on the left compared to that obtained using the sequential source method (with one source position, propagating in the forward direction).

The number of stochastic estimates N_{sto} is chosen by balancing the computational cost against the size of the stochastic noise introduced. We find that for $N_{\text{sto}} \gtrsim 100$ the stochastic noise becomes relatively small compared to the gauge noise and we employ 100 estimates across all the ensembles. In some channels the signal obtained for the three-point function, after averaging over the forward and backward directions, is comparable to that obtained from the traditional sequential source method (for a single source, computed in the forward direction), as shown in Fig. 8. Nonetheless, when taking the ratio of the three-point function with the two-point function for the fitting analysis, discussed in the next subsection, a significant part of the gauge noise cancels, while the stochastic noise remains. This results in larger statistical errors in the ratio for the stochastic approach. This is a particular problem in the vector channel. A more detailed comparison of the two methods is given in Appendix A.

As mentioned above, only flavor conserving currents and zero momentum transfer are considered, however, the data to construct three-point functions with flavor changing currents containing up to one derivative for various different momenta is also available, enabling an extensive investigation of (generalized) form factors in the future. Similarly, meson three-point functions can be constructed by computing the relatively inexpensive meson spectator part and (re-)using the insertion part, see Ref. [48] for first results.

D. Fitting and excited state analysis

The spectral decompositions of the two- and three-point correlation functions read

$$C_{2\text{pt}}^B(t) = \sum_n |Z_n^B|^2 e^{-E_n^B t}, \tag{24}$$

$$C_{3\text{pt}}^B(t,\tau;\mathcal{O}_J) = \sum_{n,m} Z_n^B Z_m^{B*} \langle n|\mathcal{O}_J|m\rangle e^{-E_n^B(t-\tau)} e^{E_m^B \tau}, \tag{25}$$

where E_n^B is the energy of state $|n\rangle$ $(n = 0, 1, \ldots)$, created when applying the baryon interpolator $\bar{\mathcal{B}}$ to the vacuum state $|\Omega\rangle$ and Z_n^B is the associated overlap factor $Z_n^B \propto \langle n|\bar{\mathcal{B}}|\Omega\rangle$. The ground state matrix elements of interest $\langle 0|\mathcal{O}_J|0\rangle = g_J^{B,\text{latt}}$ can be obtained in the limit of large time separations from the ratio of the three-point and two-point functions

$$R_J^B(t,\tau) = \frac{C_{3\text{pt}}^B(t,\tau;\mathcal{O}_J)}{C_{2\text{pt}}^B(t)} \xrightarrow{t,\tau\to\infty} g_J^{B,\text{latt}}. \tag{26}$$

However, the signal-to-noise ratio of the correlation functions deteriorates exponentially with the time separation and with current techniques it is not possible to achieve a reasonable signal for separations that are large enough to ensure ground state dominance. At moderate t and τ, one observes significant excited state contributions to the ratio. All states with the same quantum numbers as the baryon interpolator contribute to the sums in Eqs. (24) and (25), including multi-particle excitations such as $B\pi$ P-wave and $B\pi\pi$ S-wave scattering states. The spectrum of states becomes increasingly dense as one decreases the pion mass while keeping the spatial extent of the lattice sufficiently large, where the lowest lying excitations are multiparticle states.

One possible strategy is to first determine the energies of the ground state and lowest lying excitations by fitting to the two-point function (which is statistically more precise than the three-point function) with a suitable functional form. The energies can then be used in a fit to the three-point function (or the ratio R^B_J) to extract the charge g^B_J.[2] However, the three-quark baryon interpolators we use by design have only a small overlap with the multi-particle states containing five or more quarks and antiquarks and it is difficult to extract the lower lying excited state spectrum from the two-point function. Nonetheless, multiparticle states can significantly contribute to the three-point function if the transition matrix elements $\langle n|\mathcal{O}_J|0\rangle$ are large. Furthermore, depending on the current, different matrix elements, and hence excited state contributions, will dominate. In particular, one would expect the axial and scalar currents to couple to the $B\pi$ P-wave and $B\pi\pi$ S-wave states, respectively, while the tensor and vector currents may enhance transitions between B and $B\pi\pi$ states when $\pi\pi$ is in a P-wave.

The summation method [41] is an alternative approach, which involves summing the ratio over the operator insertion time $S^B_J(t) = \sum_{\tau=\tau_0}^{t-\tau_0} R^B_J(t,\tau)$, where one can show that the leading excited state contributions to $S^B_J(t)$ only depend on t [rather than also on $t-\tau$ and τ as for $R^B_J(t,\tau)$]. However, one needs a large number of source-sink separations (more than the four values of t that are realized in this study) in order to extract reliable results from this approach.

These considerations motivate us to extract the charges by fitting to the ratio of correlation functions using a fit form which takes into account contributions from up to two excited states,

$$R^B_J(t,\tau) = b^J_0 + b^J_1(e^{-\Delta E_1(t-\tau)} + e^{-\Delta E_1\tau}) + b^J_2 e^{-\Delta E_1 t} + b^J_3(e^{-\Delta E_2(t-\tau)} + e^{-\Delta E_2\tau}) + b^J_4 e^{-\Delta E_2 t}, \tag{27}$$

where $\Delta E_n = E^B_n - E^B_0$ denotes the energy gap between the ground state and the n^{th} excited state of baryon B and we have not included transitions between the first and the second excited state. The amplitude $b^J_0 = g^{B,\mathrm{latt}}_J$ gives the charge, while $b^J_{1,3}$ and $b^J_{2,4}$ are related to the ground state to excited state and excited state to excited state transition matrix elements, respectively. In practice, even when simultaneously fitting to all available source-sink separations, it is difficult to determine the energy gaps (and amplitudes) for a particular channel J. Similar to the strategy pursued in Ref. [53], we simultaneously fit to all four channels $J\in\{V,A,S,T\}$ for a given baryon. As the same energy gaps are present, the overall number of fit parameters is reduced and the fits are further constrained.

To ensure that the excited state contributions are sufficiently under control, we carry out a variety of different fits, summarized in Table II. We vary

(i) The datasets included in the fit: simultaneous fits are performed to the data for $J\in\{A,S,T,V\}$ and $J\in\{A,S,T\}$. As the axial, scalar and tensor channels are the main focus of this study, we only consider excluding the vector channel data.

(ii) The parametrization: either one (“ES = 1”) or two (“ES = 2”) excited states are included in the fits. In the latter case, in order to stabilize the fit, we use a prior for ΔE_1 corresponding to the energy gap for the lowest lying multi-particle state. As a cross-check we repeat these fits using the average result obtained for ΔE_2 in fits 5–8 as a prior and leaving ΔE_1 as a free parameter (fits 13–20). The widths of the priors are set to $E_1/100$ and to $E_2/100$, respectively. In general, the contributions from excited state to excited state transitions could not be resolved and the parameters $b^J_{2,4}$ are set to zero. We also found that the tensor and vector currents couple more strongly to the second excited state, consistent with the expectations mentioned above, and the first excited state contributions are omitted for these channels in the ES = 2 fits. Furthermore, due to the large statistical error of the stochastic three-point functions for the Σ and Ξ baryons in the vector channel (see Fig. 9 and the discussion in Appendix A), we are not able to resolve b^V_1 (and analogously b^V_3). For these baryons we also set $b^V_{1,3} = 0$ in all the fits.

(iii) The fit range: two fit intervals $\tau\in[\delta t_j, t-\delta t_j]$ are used with $\delta t_1 = n_1 a \approx 0.15$ fm and $\delta t_2 = n_2 a \approx 0.25$ fm.[3]

A typical fit to the ratios for the cascade baryon is shown in Fig. 9 for ensemble N302 ($M_\pi = 348$ MeV and $a = 0.049$ fm). The variation in the ground state matrix elements extracted from the 20 different fits is shown in Fig. 10, also for the nucleon on the same ensemble. See Appendix C for the analogous plot for the Σ baryon. Overall, the results are consistent within errors, however, some trends in the results can be seen across the different ensembles. In the axial channel, in particular the results for the fits involving a single excited state (fits 1–4), tend to be lower than those involving two excited states (fits 5–20). The former are, in general, statistically more precise than the latter due to the smaller number of parameters in the fit.

In order to study the systematics arising from any residual excited state contamination in the final results at the physical point (in the continuum limit at infinite volume), the extrapolations, detailed in Sec. III F, are performed for the results obtained from fits 1–4 (ES = 1) and fits 5–8 (ES = 2), separately. For each set of fits, 500 samples are drawn from the combined bootstrap distributions of the four

---

[2] Given the precision of the two-point function relative to that of the three-point function, this strategy is very similar to fitting C^B_{2pt} and C^B_{3pt} simultaneously.

[3] Due to $n_j \geq 2$ and its quantization, δt_1 and δt_2 depend slightly on the lattice spacing: $\delta t_j \approx 0.20$ fm, 0.29 fm ($\beta = 3.34$), $\delta t_j \approx 0.17$ fm, 0.26 fm ($\beta = 3.40$), $\delta t_j \approx 0.15$ fm, 0.23 fm ($\beta = 3.46$), $\delta t_j \approx 0.13$ fm, 0.26 fm ($\beta = 3.55$), $\delta t_j \approx 0.15$ fm, 0.25 fm ($\beta = 3.70$), $\delta t_j \approx 0.16$ fm, 0.27 fm ($\beta = 3.85$).

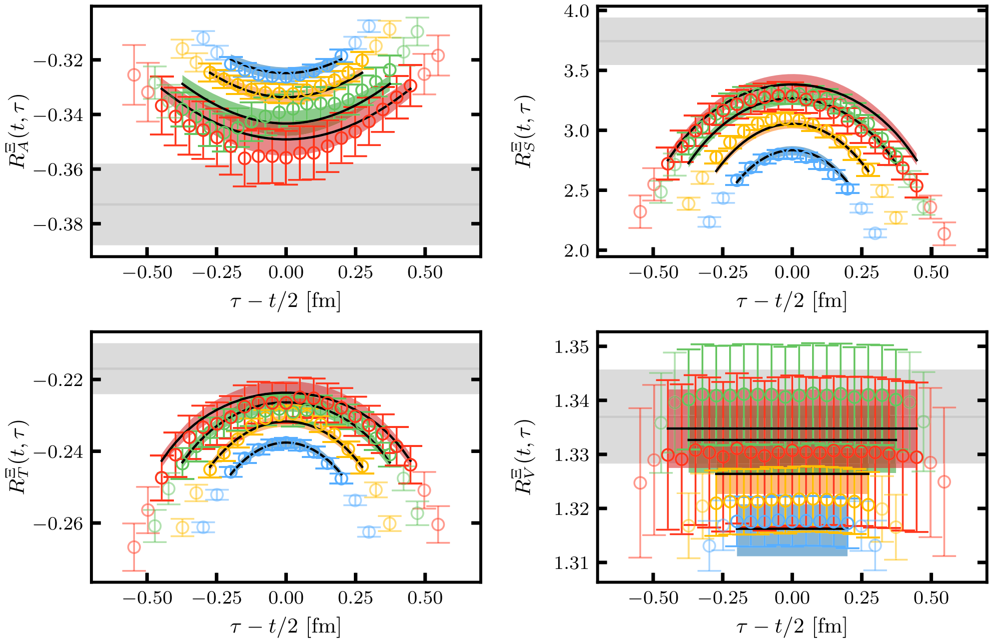

FIG. 9. Unrenormalized ratios $R_J^{\Xi}(t,\tau)$, $J \in \{A, S, T, V\}$ [defined in Eq. (26)] for the cascade baryon on ensemble N302 ($M_\pi = 348$ MeV and $a = 0.049$ fm), where $t \approx \{0.7, 0.8, 1.0, 1.2\}$ fm. The gray horizontal lines and bands show the results for the ground state matrix elements $\langle 0|\bar{u}\Gamma_J u - \bar{d}\Gamma_J d|0\rangle = g_J^{\Xi,\mathrm{latt}}$, obtained from a simultaneous fit to the ratios for all channels and source-sink separations using parametrization 7 [see Eq. (27) and Table II]. The data points with $\tau \in [\delta t, t - \delta t]$, where $\delta t = 2a$, are included in the fit (the faded data points are omitted), which is the maximum fit range possible for our action. The colored curves show the expectation from the fit for each source-sink separation.

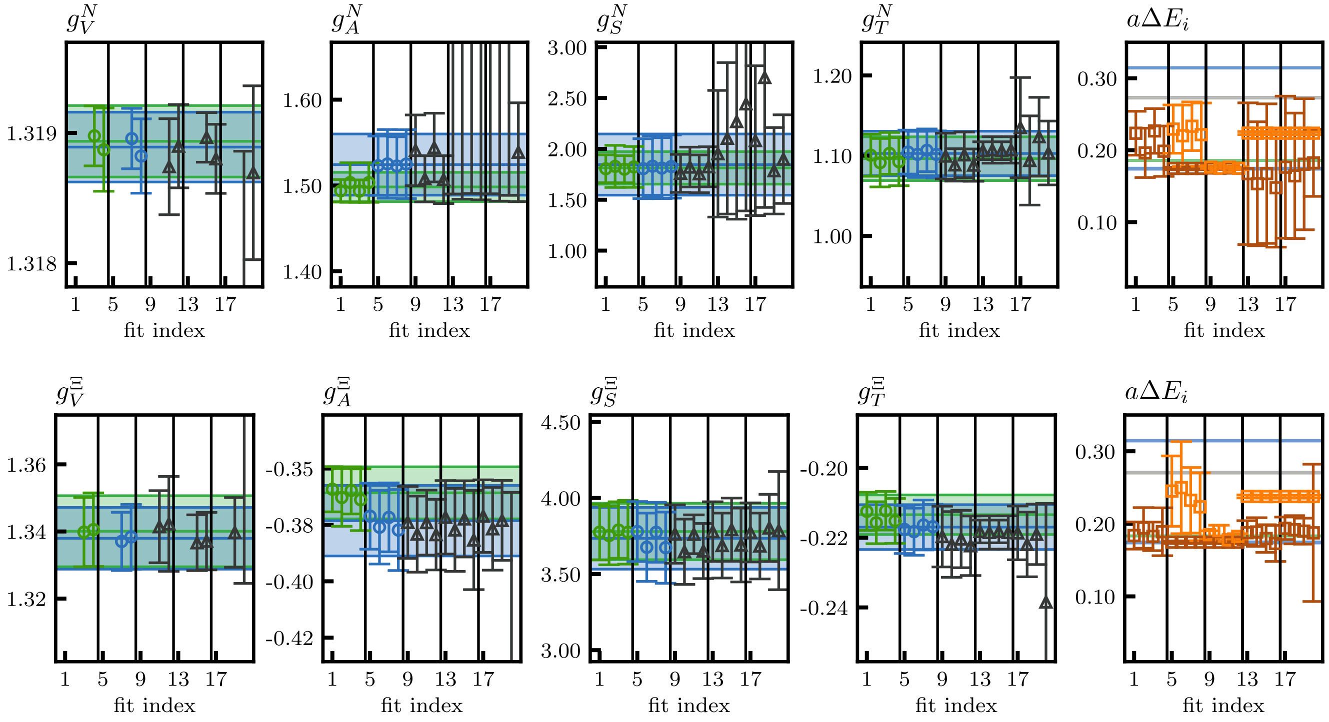

FIG. 10. Results for the four unrenormalized charges of the nucleon (top) and cascade baryon (bottom) obtained from the fits listed in Table II for ensemble N302 ($M_\pi = 348$ MeV and $a = 0.049$ fm). The green (blue) horizontal lines and bands indicate the final results and errors obtained from the median and 68% confidence level interval of the combined bootstrap distributions determined from the fits indicated by the green (blue) data points which include one (two) excited state(s). On the right the energy gaps determined in the fits and those corresponding to the lowest lying multiparticle states are displayed using the same color coding as in Fig. 11.

TABLE II. Summary of the fits performed. We vary the combinations of channels J that are fitted simultaneously as well as the number of excited states (ES) included in the fit and the fit interval $\tau \in [\delta t, t - \delta t]$ with $\delta t \in \{\delta t_1, \delta t_2\}$, where $\delta t_1 \approx 0.15$ fm, $\delta t_2 \approx 0.25$ fm. The last two columns indicate which parameters in Eq. (27) are constrained by a prior or set to zero. All other parameters are determined in the fit.

Fit	J	δt	ES	Prior	Set to zero
1	A, S, T	δt_1	1		$b_2^J, b_3^J, b_4^J, \Delta E_2$
2	A, S, T	δt_2	1		$b_2^J, b_3^J, b_4^J, \Delta E_2$
3	A, S, T, V	δt_1	1		$b_2^J, b_3^J, b_4^J, \Delta E_2$
4	A, S, T, V	δt_2	1		$b_2^J, b_3^J, b_4^J, \Delta E_2$
5	A, S, T	δt_1	2	ΔE_1	b_1^T, b_2^J, b_4^J
6	A, S, T	δt_2	2	ΔE_1	b_1^T, b_2^J, b_4^J
7	A, S, T, V	δt_1	2	ΔE_1	$b_1^{T,V}, b_2^J, b_4^J$
8	A, S, T, V	δt_2	2	ΔE_1	$b_1^{T,V}, b_2^J, b_4^J$
9	A, S, T	δt_1	2	ΔE_1	b_2^J, b_4^J
10	A, S, T	δt_2	2	ΔE_1	b_2^J, b_4^J
11	A, S, T, V	δt_1	2	ΔE_1	b_2^J, b_4^J
12	A, S, T, V	δt_2	2	ΔE_1	b_2^J, b_4^J
13	A, S, T	δt_1	2	ΔE_2	b_1^T, b_2^J, b_4^J
14	A, S, T	δt_2	2	ΔE_2	b_1^T, b_2^J, b_4^J
15	A, S, T, V	δt_1	2	ΔE_2	$b_1^{T,V}, b_2^J, b_4^J$
16	A, S, T, V	δt_2	2	ΔE_2	$b_1^{T,V}, b_2^J, b_4^J$
17	A, S, T	δt_1	2	ΔE_2	b_2^J, b_4^J
18	A, S, T	δt_2	2	ΔE_2	b_2^J, b_4^J
19	A, S, T, V	δt_1	2	ΔE_2	b_2^J, b_4^J
20	A, S, T, V	δt_2	2	ΔE_2	b_2^J, b_4^J

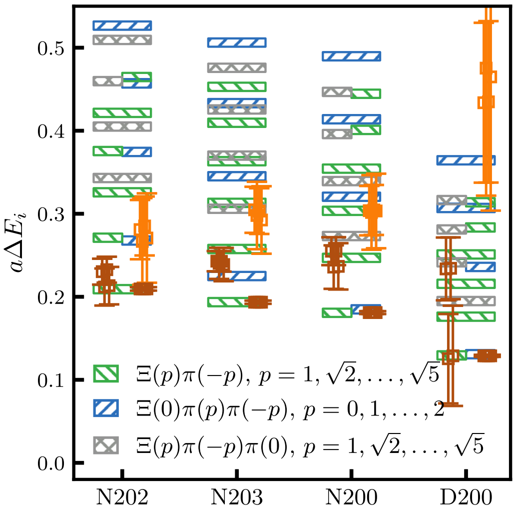

FIG. 11. Results for the first and second excited state energy gaps of the cascade baryon, ΔE_1 (brown data points) and ΔE_2 (orange data points), respectively, determined on ensembles lying on the $\mathrm{tr}\, M = \mathrm{const}$ trajectory with $a = 0.064$ fm. The pion mass decreases from left to right with $M_\pi = 414$ MeV for ensemble N202 and $M_\pi = 202$ MeV for ensemble D200, see Table I. For each ensemble, the ΔE_1 obtained using fits 1–4 of Table II are shown on the left and the ΔE_1 (fixed with a prior to the lowest multi-particle energy gap) and ΔE_2 resulting from fits 5–8 are displayed on the right. For comparison, the energy gaps of the lower lying noninteracting multiparticle states with the quantum numbers of the cascade baryon are shown as horizontal lines, where the momenta utilized for each hadron are indicated in lattice units.

fit variations. The final result and error, shown as the green and blue bands in Fig. 10, correspond to the median and the 68% confidence interval, respectively. Note that we take the same 500 bootstrap samples for all the baryons to preserve correlations. The final results for all the ensembles are listed in Tables XVI–XVIII of Appendix B for the nucleon, sigma and cascade baryons, respectively.

In terms of the energy gaps extracted, Fig. 10 shows that we find consistency across variations in the fit range and whether the vector channel data is included or not. However, the first excited energy gap ΔE_1 obtained from the single excited state fits tends to be higher than the lowest multiparticle level, in particular, as the pion mass is decreased, suggesting that contributions from higher excited states are significant. This can be seen in Fig. 11, where we compare the results for the energy gaps for the cascade baryon with the lower lying noninteracting $\Xi\pi$ and $\Xi\pi\pi$ states for four ensembles with $a = 0.064$ fm and pion masses ranging from 414 MeV down to 202 MeV. Note that the multi-particle levels are modified in a finite volume, although the corresponding energy shifts may be small for the large volumes realized here. There are a number of levels within roughly 500 MeV of the first excited state. Some levels lie close to each other and one would not expect that the difference can be resolved by fits with one or two excited states. The ΔE_2 energy gaps from the two excited state fits (with the first excited state fixed with a prior to the lowest multi-particle level) are consistent with the next level that is significantly above the first excited state, although for ensemble D200 the errors are too large to draw a conclusion. Given that more than one excited state is contributing significantly, we expect that the latter fits isolate the ground state contribution more reliably. We remark that within present statistics, two-exponential fits to the two-point functions alone give energy gaps $a\Delta E = 0.390(37), 0.371(34), 0.430(37)$ and $0.312(46)$ for N202, N203, N200 and D200, respectively, that are all larger than

TABLE III. Improvement coefficients b_J for $J \in \{A, S, T, V\}$ from Refs. [54,55].

β	b_A	b_S	b_T	b_V
3.34	1.249(16)	1.622(47)	1.471(11)	1.456(11)
3.4	1.244(16)	1.583(62)	1.4155(48)	1.428(11)
3.46	1.239(15)	1.567(74)	1.367(12)	1.410(13)
3.55	1.232(15)	1.606(98)	1.283(14)	1.388(17)
3.7	1.221(13)	1.49(11)	1.125(15)	1.309(22)
3.85	1.211(12)	1.33(16)	0.977(38)	1.247(26)

$a\Delta E_2$, with the exception of D200, where the two gaps agree within errors.

E. Nonperturbative renormalization and improvement

The isovector lattice charges, $g_J^{B,\mathrm{latt}}$, extracted in the previous subsection need to be matched to the continuum $\overline{\mathrm{MS}}$ scheme. The renormalized matrix elements suffer from discretization effects, however, the leading order effects are reduced to $O(a^2)$ when implementing full $O(a)$ improvement. In the forward limit, in addition to using a nonperturbatively $O(a)$ improved fermion action, this involves taking mass dependent terms into account. The following multiplicative factors are applied,

$$g_J^B = Z_J^k(1 + am_\ell b_J + 3a\bar{m}\tilde{b}_J)g_J^{B,\mathrm{latt}} + O(a^2), \qquad (28)$$

for $J \in \{V, A, S, T\}$, where Z_J are the renormalization factors and b_J and $\tilde{b}_J$ are the $O(a)$ improvement coefficients. Note that the renormalization factors for the scalar and tensor currents depend on the scale, $Z_{S,T} = Z_{S,T}(\mu)$, where we take $\mu = 2$ GeV. The vector Ward identity lattice quark mass am_q is obtained from the hopping parameter κ_q ($q = \ell, s$) and the critical hopping parameter κ_{crit} via $am_q = (1/\kappa_q - 1/\kappa_{\mathrm{crit}})/2$. $\bar{m} = (2m_\ell + m_s)/3$ denotes the flavor averaged quark mass. The hopping parameters for all ensembles used within this work are tabulated in Table XV of Appendix B. For κ_{crit} we utilize the interpolation formula [17]

$$\frac{1}{\kappa_{\mathrm{crit}}} = 8 - 0.402454g^2\,\frac{1 + 0.28955g^2 - 0.1660g^6}{1 + 0.22770g^2 - 0.2540g^4}. \qquad (29)$$

The improvement coefficients b_J and $\tilde{b}_J$ are determined nonperturbatively in Ref. [54]. We make use of updated preliminary values, which will appear in a future publication [55]. These are listed in Tables III and IV, respectively. Note that no estimates of $\tilde{b}_J$ are available for $\beta = 3.85$. Considering the size of the statistical errors, the general reduction of the $|\tilde{b}_J|$ values with increasing β (and the decreasing a), at this lattice spacing we set $\tilde{b}_J = 0$ for all J.

TABLE IV. Improvement coefficients $\tilde{b}_J$ for $J \in \{A, S, T, V\}$ from Refs. [54,55]. Note that no results are available for $\beta = 3.85$.

β	$\tilde{b}_A$	$\tilde{b}_S$	$\tilde{b}_T$	$\tilde{b}_V$
3.34	−0.06(28)	−0.24(55)	1.02(16)	1.05(13)
3.4	−0.11(13)	−0.36(23)	0.49(17)	0.41(11)
3.46	0.08(11)	−0.421(83)	0.115(19)	0.158(28)
3.55	−0.03(13)	−0.25(12)	0.000(37)	0.069(42)
3.7	−0.047(75)	−0.274(65)	−0.0382(60)	−0.031(18)

For the renormalization factors, we employ the values obtained in Ref. [56]. The factors are determined nonperturbatively in the RI′-SMOM scheme [57,58] and then (for Z_S and Z_T) converted to the $\overline{\mathrm{MS}}$ scheme using three-loop matching [59–61]. We remark that the techniques for implementing the Rome-Southampton method were extended in Ref. [56] to ensembles with open boundary conditions in time. This development enables us to utilize ensembles with $a < 0.06$ fm, where only open boundary conditions in time are available due to the need to maintain ergodicity. A number of different methods are employed in Ref. [56] to determine the renormalization factors. In order to assess the systematic uncertainty arising from the matching in the final results for the charges at the physical point in the continuum limit, we make use of two sets of results, collected in Tables V and VI and referred to as Z_J^1 and Z_J^2, respectively, in the following. The first set of results are extracted using the fixed-scale method, where the RI′-SMOM factors are determined at a fixed scale (ignoring discretization effects), while the second set are obtained by fitting the factors as a function of the scale and the lattice spacing, the “fit method.” See Ref. [56] for further details. In both cases, lattice artefacts are reduced by subtracting the perturbative one-loop expectation. For the axial and

TABLE V. Set of renormalization factors taken from Ref. [56], denoted as Z_J^1 in the text. The factors are determined using the RI′-SMOM scheme and the “fixed-scale method” with the perturbative subtraction of lattice artefacts. For Z_A and Z_V, the values correspond to those listed under Z_A' and Z_V', respectively, which are obtained using renormalization conditions consistent with the respective Ward identities. The statistical and systematic errors have been added in quadrature.

β	Z_A	$Z_S^{\overline{\mathrm{MS}}}(2\ \mathrm{GeV})$	$Z_T^{\overline{\mathrm{MS}}}(2\ \mathrm{GeV})$	Z_V
3.34	0.77610(58)	0.6072(26)	0.8443(35)	0.72690(71)
3.4	0.77940(36)	0.6027(25)	0.8560(35)	0.73290(67)
3.46	0.78240(32)	0.5985(25)	0.8665(36)	0.73870(71)
3.55	0.78740(22)	0.5930(25)	0.8820(37)	0.74740(82)
3.7	0.79560(98)	0.5846(24)	0.9055(42)	0.76150(94)
3.85	0.8040(13)	0.5764(25)	0.9276(42)	0.77430(76)

TABLE VI. Set of renormalization factors denoted as Z_J^2 in the text. These are determined as in Table V but now using the “fit method.”

β	Z_A	$Z_S^{\overline{\mathrm{MS}}}(2\ \mathrm{GeV})$	$Z_T^{\overline{\mathrm{MS}}}(2\ \mathrm{GeV})$	Z_V
3.34	0.7579(42)	0.6115(93)	0.8321(95)	0.7072(60)
3.4	0.7641(35)	0.6068(86)	0.8462(88)	0.7168(49)
3.46	0.7695(36)	0.6025(79)	0.8585(84)	0.7250(43)
3.55	0.7774(36)	0.5968(66)	0.8756(76)	0.7367(37)
3.7	0.7895(32)	0.5880(45)	0.9010(63)	0.7544(30)
3.85	0.8006(25)	0.5793(35)	0.9243(55)	0.7699(38)

TABLE VII. Renormalization factors Z_A and Z_V obtained from the interpolation formulas in Eqs. (C.7) and (C.8) in Ref. [63], denoted as Z_J^3 in the text.

β	Z_A	Z_V
3.34	0.7510(11)	0.7154(11)
3.4	0.75629(65)	0.72221(65)
3.46	0.76172(39)	0.72898(39)
3.55	0.76994(34)	0.73905(35)
3.7	0.78356(32)	0.75538(33)
3.85	0.79675(45)	0.77089(47)

vector currents, we also consider a third set of renormalization factors, Z_J^3, listed in Table VII, that are obtained with the chirally rotated Schrödinger functional approach [62], see Ref. [63]. We emphasize that employing the different sets of renormalization factors should lead to consistent results for the charges in the continuum limit.

F. Extrapolation strategy

In the final step of the analysis the renormalized charges g_J^B determined at unphysical quark masses and finite lattice spacing and spatial volume are extrapolated to the physical point in the continuum and infinite volume limits. We employ a similar strategy to the one outlined in Ref. [64] and choose continuum fit functions of the form

$$g_J^B(M_\pi, M_K, L, a=0) = c_0 + c_\pi M_\pi^2 + c_K M_K^2 + c_V M_\pi^2 \frac{e^{-LM_\pi}}{\sqrt{LM_\pi}}, \qquad (30)$$

to parameterize the quark mass and finite volume dependence, where L is the spatial lattice extent and the coefficients c_X, $X \in \{0, \pi, K, V\}$ are understood to depend on the baryon B and the current J. The leading order coefficients c_0 give the charges in the SU(3) chiral limit, which can be expressed in terms of two LECs, e.g., F and D, for the axial charges, see Eq. (7).

Equation (30) is a phenomenological fit form based on the SU(3) ChPT expressions for the axial charge. It contains the expected $O(p^2)$ terms for the quark mass dependence and the dominant finite volume corrections. The $O(p^3)$ expressions for g_A^B [65–67] contain log terms with coefficients completely determined by the LECs F and D. In an earlier study of the axial charges on the $m_s = m_\ell$ subset of the ensembles used here [64], we found that including these terms did not provide a satisfactory description of the data. When terms arising from loop corrections that contain decuplet baryons are taken into account, additional LECs enter that are difficult to resolve. If the coefficient of the log term is left as a free parameter, one finds that the coefficient has the opposite sign to the ChPT expectation without decuplet loops. We made similar observations in this study and this is also consistent with the findings of previous works, see, e.g., Refs. [68–70]. Finite volume effects appear at $O(p^3)$ with no additional LECs appearing in the coefficients. Again the signs of the corrections are the opposite to the trend seen in the data and, when included, it is difficult to resolve the effects of the decuplet baryons. As is shown in Sec. IV, the data for all the charges are well described when the fit form is restricted to the dominant terms, with free coefficients c_0, c_π, c_K and c_V.

We remark that the same set of LECs appear in the $O(p^2)$ SU(3) ChPT expressions for the three different octet baryons (for a particular charge). Ideally, one would carry out a simultaneous fit to the whole baryon octet (taking the correlations between the g_J^B determined on the same ensemble into account). However, we obtain very similar results when fitting the g_J^B individually compared to fitting the results for all the octet baryons simultaneously. For simplicity, we choose to do the former, such that the coefficients c_X for the different baryons are independent of one another.

Lattice spacing effects also need to be taken into account and we add both mass independent and mass dependent terms to the continuum fit ansatz to give

$$\begin{aligned} g_J^B(M_\pi, M_K, L, a) = g_J^B(&\mathcal{M}_\pi, \mathcal{M}_K, L, 0) \\ &+ c_a \mathbb{a}^2 + \bar{c}_a \bar{\mathcal{M}}^2 \mathbb{a}^2 + \delta c_a \delta\mathcal{M}^2 \mathbb{a}^2 \\ &+ c_{a,3} \mathbb{a}^3, \end{aligned} \qquad (31)$$

where $\bar{\mathcal{M}}^2 = (2\mathcal{M}_K^2 + \mathcal{M}_\pi^2)/3$ and $\delta\mathcal{M}^2 = \mathcal{M}_K^2 - \mathcal{M}_\pi^2$. The meson masses are rescaled with the Wilson flow scale t_0 [71], $\mathcal{M}_{\pi,K} = \sqrt{8t_0} M_{\pi,K}$ to form dimensionless combinations. This rescaling is required to implement full $O(a)$ improvement (along with employing a fermion action and isovector currents that are nonperturbatively $O(a)$ improved) when simulating at fixed bare lattice coupling instead of at fixed lattice spacing, see Sec. 4.1 of Ref. [17] for a detailed discussion of this issue. The values of t_0/a^2 and the pion and kaon masses in lattice units for our set of ensembles are given in Table XV of Appendix B. We translate between different lattice spacings using $t_0^\star$, the value of t_0 along the symmetric line where $12 t_0^\star M_\pi^2 = 1.110$ [72], i.e., $\mathbb{a} = a/\sqrt{8t_0^\star}$. The values, determined in Ref. [17], are listed in Table VIII. Note that we include a term that is cubic in the lattice spacing in the fit form, however, this term is only utilized in the analysis of the vector charge, for which we have the most precise data.

TABLE VIII. Values for $t_0^\star/a^2$ at each β-value as determined in Ref. [17].

β	3.34	3.4	3.46	3.55	3.7	3.85
$\frac{t_0^\star}{a^2}$	2.204(6)	2.888(8)	3.686(11)	5.157(15)	8.617(22)	13.988(34)

To obtain results at the physical quark mass point, we make use of the scale setting parameter

$$\sqrt{8t_{0,\mathrm{phys}}} = 0.4098^{(20)}_{(25)}\ \mathrm{fm}, \tag{32}$$

determined in Ref. [17] and take the isospin corrected pion and kaon masses quoted in the FLAG 16 review [73] to define the physical point in the quark mass plane,

$$M_\pi^{\mathrm{phys}} = 134.8(3)\ \mathrm{MeV}, \tag{33}$$

$$M_K^{\mathrm{phys}} = 494.2(3)\ \mathrm{MeV}. \tag{34}$$

In practice, we choose to fit to the bare lattice charges $g_J^{B,\mathrm{latt}}$ rather than the renormalized ones as this enables us to include the uncertainties of the renormalization and improvement factors (which are the same for all ensembles at fixed β) consistently. Therefore, our final fit form reads

$$g_J^{B,\mathrm{latt}} = \frac{g_J^B(M_\pi, M_K, L, a)}{Z_J^k(\beta)(1 + am_\ell b_J(\beta) + 3a\bar{m}\tilde{b}_J(\beta))}, \tag{35}$$

where the dependence of the factors on the β-value is made explicit and the superscript k of Z_J^k refers to the different determinations of the renormalization factors that we consider, $k = 1, 2, 3$ for $J \in \{A, V\}$ and $k = 1, 2$ for $J \in \{S, T\}$ (see Tables V–VII in the previous subsection). We introduce a separate parameter for Z_J^k, b_J and $\tilde{b}_J$ for each β-value and add corresponding "prior" terms to the χ^2 function. The statistical uncertainties of these quantities are incorporated by generating pseudobootstrap distributions.

The systematic uncertainty in the determination of the charges at the physical point is investigated by varying the fit model and by employing different cuts on the ensembles that enter the fits. For the latter we consider

(1) no cut: including all the available data points, denoted as dataset 0, DS (0),
(2) pion mass cut: excluding all ensembles with $M_\pi > 400$ MeV, DS($M_\pi^{<400\ \mathrm{MeV}}$),
(3) pion mass cut: excluding all ensembles with $M_\pi > 300$ MeV, DS($M_\pi^{<300\ \mathrm{MeV}}$),
(4) a lattice spacing cut: excluding the coarsest lattice spacing, i.e., the ensembles with $a \approx 0.098$ fm, DS($a^{<0.1\ \mathrm{fm}}$), and
(5) a volume cut: excluding all ensembles with $LM_\pi < 4$, DS($LM_\pi^{>4}$).

In some cases, more than one cut is applied, e.g., cut 2 and 4, with the dataset denoted DS($M_\pi^{<400\ \mathrm{MeV}}, a^{<0.1\ \mathrm{fm}}$), etc. Our final results are obtained by carrying out the averaging procedure described in Appendix B of Ref. [64] which gives an average and error that incorporates both the statistical and systematic uncertainties.

IV. EXTRAPOLATIONS TO THE CONTINUUM, INFINITE VOLUME, PHYSICAL QUARK MASS LIMIT

We present the extrapolations to the physical point in the continuum and infinite volume limits of the isovector vector (V), axial (A), scalar (S) and tensor (T) charges for the nucleon (N), sigma (Σ) and cascade (Ξ) octet baryons.

A. Vector charges

The isovector vector charges for the nucleon, cascade and sigma baryons are $g_V^N = g_V^\Xi = 1$ and $g_V^\Sigma = 2$, up to second order isospin breaking corrections [74]. These values also apply to our isospin symmetric lattice results in the continuum limit for any quark mass combination and volume. A determination of the vector charges provides an important cross-check of our analysis methods and allows us to demonstrate that all systematics are under control.

To start with, we display the ratios of the hyperon charges over the nucleon charge in Fig. 12. The renormalization factors drop out in the ratio and lattice spacing effects are expected to cancel to some extent. As one can see, the results align very well with the expected values.

For the individual charges, we perform a continuum extrapolation of the data using the fit form

$$g_V = c_0 + c_a \mathbb{a}^2 + \bar{c}_a \bar{\mathcal{M}}^2 \mathbb{a}^2 + \delta c_a \delta\mathcal{M}^2 \mathbb{a}^2 + c_{a,3} \mathbb{a}^3. \tag{36}$$

Note that there is no dependence on the pion or kaon mass nor on the spatial volume in the continuum limit. $\mathcal{M}^2$ and $\delta\mathcal{M}^2$ represent the flavor average and difference of the kaon and pion masses squared, rescaled with the scale

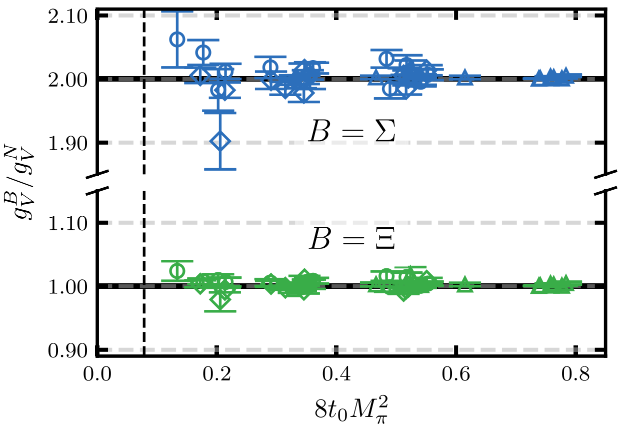

FIG. 12. Ratio of the hyperon ($B = \Sigma, \Xi$) vector charges over the nucleon charge, g_V^B/g_V^N, as a function of the rescaled pion mass squared ($8t_0M_\pi^2 = \mathcal{M}_\pi^2$). The data were extracted using two excited states in the fitting analysis, see Sec. III D, and not corrected for lattice spacing or volume effects. Circles (diamonds) correspond to the tr M = const (m_s = const) trajectories, the triangles to the $m_s = m_\ell$ line.

parameter t_0, while the lattice spacing $\mathbb{a} = a/\sqrt{8t_0^*}$. See the previous section for further details of the extrapolation procedure. We implement full $O(a)$ improvement and leading discretization effects are quadratic in the lattice spacing. However, the data for the nucleon vector charge are statistically very precise and higher order effects can be resolved. This motivates the addition of the cubic term in Eq. (36). The data for g_V^Σ and g_V^Ξ are less precise as they are determined employing the stochastic approach outlined in Sec. III C which introduces additional noise, see Appendix A for further discussion.

The data are well described by Eq. (36), as demonstrated by the fit, shown in Fig. 13, for g_V^N which has a goodness of fit of $\chi^2/N_{\mathrm{dof}} = 0.92$. The data are extracted using two excited states in the fitting analysis (see Sec. III D) and we employ the most precise determination of the renormalization factors (Z_V^3, see Table VII). A cut of $M_\pi < 400$ MeV is imposed on the ensembles entering the fit, however, fits including all data points are also performed, as detailed below. When the data are corrected for the discretization effects according to the fit, we see consistency with $g_V^N = 1$, for all pion and kaon masses. Using the fit to shift the data points to the physical point, we observe that the lattice spacing dependence is moderate but statistically significant, with a 3–4% deviation from the continuum value at the coarsest lattice spacing (lower panel of Fig. 13).

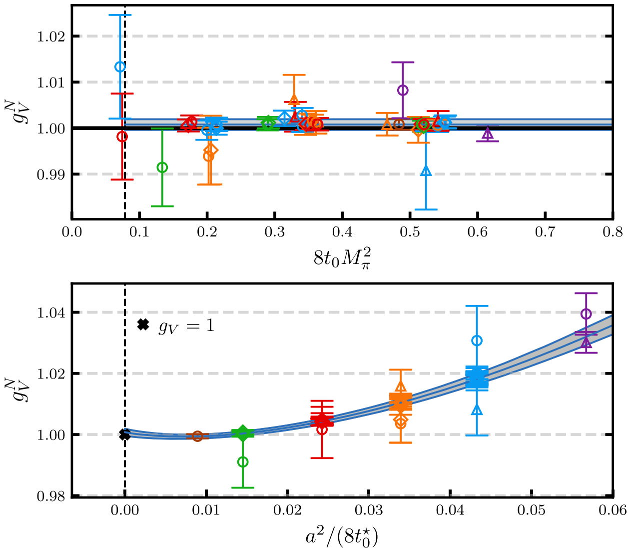

FIG. 13. Continuum limit extrapolation of the nucleon isovector vector charge g_V^N for a five parameter fit [Eq. (36)] using the renormalization factors Z_V^3 (see Table VII) and imposing the cut $M_\pi < 400$ MeV. The data were extracted including two excited states in the fitting analysis, see Sec. III D. The upper panel shows the data points corrected for discretization effects according to the fit. They are consistent with $g_V^N = 1$. The bottom panel shows the lattice spacing dependence at the physical point. The blue lines and gray bands indicate the expectations from the fit. For better visibility, the data point for ensemble D452, which has a relatively large error (see Table XVI), is not displayed. Circles (diamonds) correspond to the $\mathrm{tr}\, M = \mathrm{const}$ ($m_s = \mathrm{const}$) trajectories, the triangles to the $m_s = m_\ell$ line.

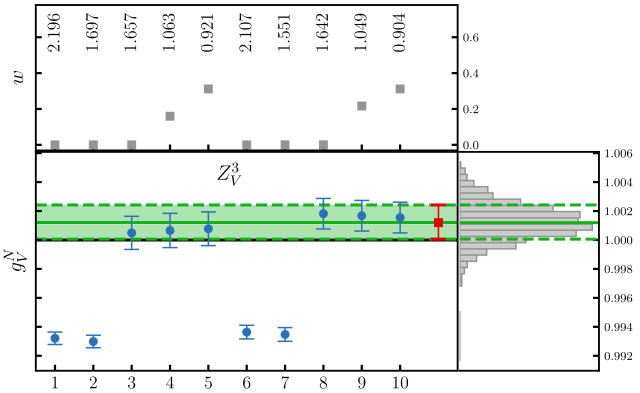

FIG. 14. Results for the nucleon vector charge g_V^N in the continuum limit at the physical point obtained using Z_V^3 (see Table VII) and five different parametrizations applied to dataset $\mathrm{DS}(M_\pi^{<400\ \mathrm{MeV}})$ (fits to Eq. (31) with different coefficients set to zero labeled 1, …, 5, see the text) and $\mathrm{DS}(M_\pi^{<400\ \mathrm{MeV}}, a^{<0.1\ \mathrm{fm}})$ (6, …, 10). See Sec. III F for the definitions of the data sets. The data were extracted including two excited states in the fitting analysis, see Sec. III D. The model average is shown as the red data point and the green horizontal line and band. On the right the model averaged distribution is displayed as a histogram where also the median and the 68% confidence level interval, which form the final result, are indicated (green lines). The top panel shows the weights (gray points) assigned to the individual fits, with the corresponding χ^2/N_{dof} values given above.

In order to investigate the uncertainty arising from the choice of parametrization and the importance of the different terms, we repeat the extrapolations employing five different parametrizations (listed in terms of the coefficients of the terms entering the fit): $(1, \{c_0, c_a\})$, $(2, \{c_0, c_a, \delta c_a\})$, $(3, \{c_0, c_a, c_{a,3}\})$, $(4, \{c_0, c_a, c_{a,3}, \delta c_a\})$ and $(5, \{c_0, c_a, c_{a,3}, \bar{c}_a, \delta c_a\})$.[4] Regarding the lattice spacing dependence, the mass independent term c_a is always included as the other terms are formally at a higher order. These five fits are performed on two datasets. The first set contains ensembles with $M_\pi < 400$ MeV [dataset $\mathrm{DS}(M_\pi^{<400\ \mathrm{MeV}})$], while in the second set the ensembles with the coarsest lattice spacing are also excluded ($\mathrm{DS}(M_\pi^{<400\ \mathrm{MeV}}, a^{<0.1\ \mathrm{fm}})$, +5 is added to the fit number). See the end of Sec. III F for the definitions of the datasets.

The results for g_V^N, displayed in Fig. 14, show that the cubic term and at least one mass dependent term are needed to obtain a reasonable description of the data in terms of the χ^2/N_{dof}. Two of the fit forms with large χ^2/N_{dof} values (corresponding to 1, 2, 6, 7, with negligible weight in the

---

[4] We also investigated the possibility of residual $\mathcal{O}(a)$ effects, in spite of the nonperturbative improvement of the current and the action. Indeed, the coefficients of additional terms $\propto a$ were found to be consistent with zero.

TABLE IX. Results for g_V^B, $B \in \{N, \Sigma, \Xi\}$, obtained with three different sets of renormalization factors. The errors include the statistical and all the systematic uncertainties.

Renormalization	g_V^N	g_V^Σ	g_V^Ξ
Z_V^1 (Table V)	$0.9975^{(22)}_{(20)}$	$2.012^{(26)}_{(16)}$	$1.012^{(13)}_{(11)}$
Z_V^2 (Table VI)	$0.9945^{(66)}_{(41)}$	$2.014^{(36)}_{(16)}$	$1.008^{(19)}_{(8)}$
Z_V^3 (Table VII)	$1.0012^{(12)}_{(11)}$	$2.021^{(21)}_{(27)}$	$1.015^{(10)}_{(11)}$

model averaging procedure) give values that are inconsistent with the continuum expectation. The results are stable under the removal of the coarsest ensembles. Performing the model averaging procedure, the final result for the nucleon, given in the last row of the first column of Table IX, agrees with the expectation $g_V^N = 1$ within a combined statistical and systematic uncertainty of about 1‰.

The above analysis is also performed utilizing the sets of renormalization factors Z_V^1 and Z_V^2, determined via the RI′-SMOM scheme [56]. The results for the nucleon vector charge are compared in Fig. 15. The uncertainties on these factors are larger, in particular for Z_V^2, than those of set Z_V^3, which is derived using the chirally rotated Schrödinger functional approach [63]. This translates into larger errors for g_V^N for those fits. The lattice spacing dependence is somewhat different: the first quadratic mass dependent term in Eq. (36) and the cubic term can no longer be fully resolved and also parametrization $(2, \{c_0, c_a, \delta c_a\})$ gives a $\chi^2/N_{\mathrm{dof}} = 1.00$ (0.95) when employing Z_V^1 (Z_V^2).

The systematic uncertainty of the results due to residual excited state contamination and the range of pion masses

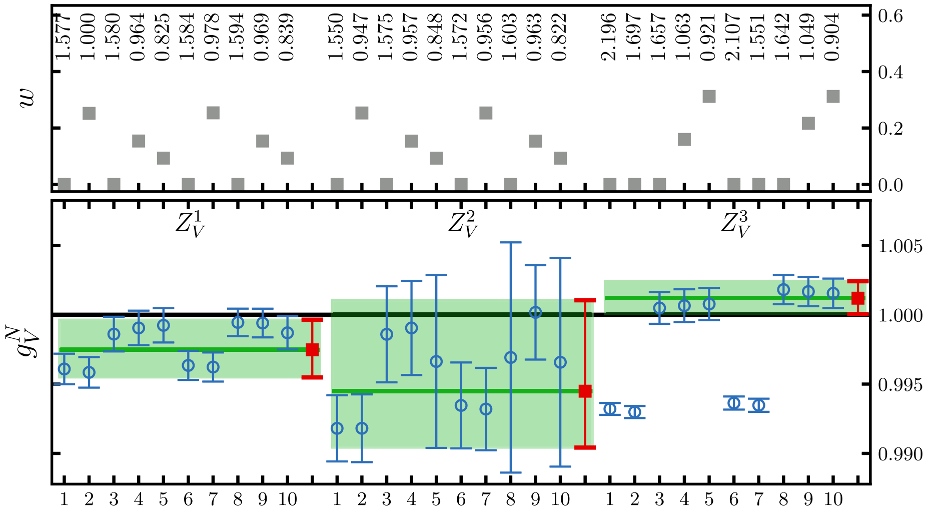

FIG. 15. Results for the nucleon vector charge g_V^N as in Fig. 14 but now also including those obtained employing Z_V^1 and Z_V^2.

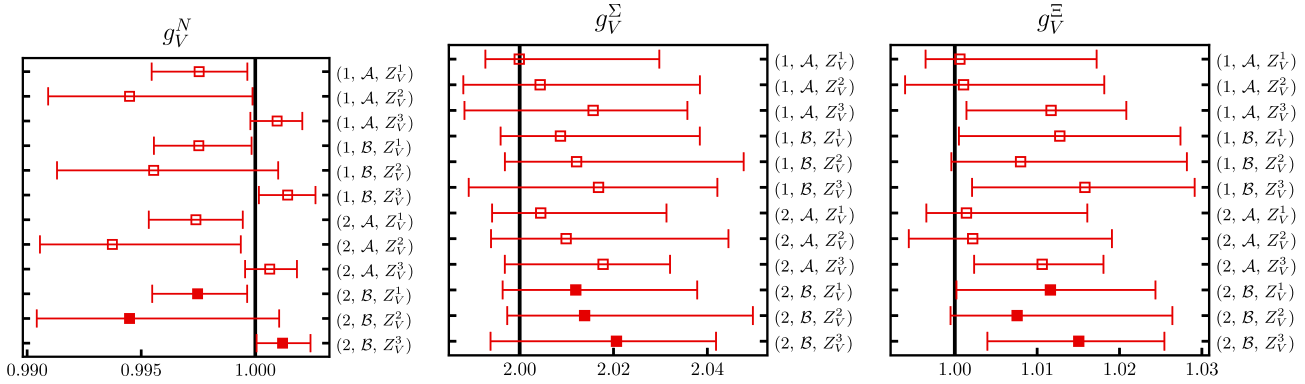

FIG. 16. Overview of the results for the vector charges g_V^B, $B \in \{N, \Sigma, \Xi\}$, obtained from different datasets. These are labeled by the number of excited states used in the fitting analysis (ES = 1, 2), the pion mass cut imposed (denoted $\mathcal{A}$ or $\mathcal{B}$) and the set of renormalization factors employed (Z_V^k, $k = 1, 2, 3$). Each data point represents a model averaged result. The label $\mathcal{A}$ indicates that 15 fits [5 fit variations applied to three datasets, DS(0), DS($M_\pi^{<400\ \mathrm{MeV}}$) and DS($a^{<0.1\ \mathrm{fm}}$)] are averaged, while the results labeled with $\mathcal{B}$ are based on the set of 10 fits utilized in Fig. 14 (5 fit variations applied to two datasets, DS($M_\pi^{<400\ \mathrm{MeV}}$) and DS[$M_\pi^{<400\ \mathrm{MeV}}$, $a^{<0.1\ \mathrm{fm}}$)]. See Sec. III F for the definitions of the datasets. The final results for each Z_V^k (filled squares) are listed in Table IX.

employed in the extrapolations is also considered. Figure 16 shows the model averaged results discussed so far, displayed as filled squares, and also those obtained using several other sets of fits. These are labeled in terms of the number of excited states (one or two) included in the fitting analysis, the cuts imposed on the pion mass ($\mathcal{A}$ or $\mathcal{B}$) and the renormalization factors utilized. For the results from pion mass cut $\mathcal{A}$, 15 fits enter the model average, the five different parametrizations are applied to three datasets DS(0), DS($M_\pi^{<400\text{ MeV}}$) and DS($a^{<0.1\text{ fm}}$). Note that the first and third dataset include ensembles with pion masses up to 430 MeV. For mass cut $\mathcal{B}$, datasets DS($M_\pi^{<400\text{ MeV}}$) and DS[$M_\pi^{<400\text{ MeV}}$, $a^{<0.1\text{ fm}}$)] are used, giving 10 fits in total. The results only depend on the choice of renormalization factors, suggesting that the systematic uncertainties due to excited state contamination and the cut made on the pion mass are very small.

Repeating the whole procedure for the sigma and the cascade baryons gives vector charges which are also consistent with the expected values to within 1.5σ, as shown in Fig. 16 (see Figs. 41 and 42 in Appendix C for the individual fits for mass cut $\mathcal{B}$). The statistical noise introduced by the stochastic approach dominates, leading to much less precise values and very little variation between the results for the different hyperon data sets. We take the values obtained from the datasets ($2, \mathcal{B}, Z_V^k$), listed in Table IX, as our estimates of the vector charges as these datasets give the most reliable determinations of the charges across the different channels (as discussed in the following subsections).

Overall, the results demonstrate that the systematics arising from excited state contamination, renormalization and finite lattice spacing are under control in our analysis in this channel (to within an error of 1‰ for the nucleon).

B. Axial charges

In the following we present our results for the nucleon, sigma and cascade isovector axial charges g_A^B, $B \in \{N, \Sigma, \Xi\}$. The nucleon axial charge is very precisely measured in experiment, $\lambda = g_A^N/g_V^N = 1.2754(13)$ [75], and serves as another benchmark quantity when assessing the size of the systematics of the final results. Note, however, that possible differences of up to 2%, due to radiative corrections, between λ computed in QCD and an effective λ measured in experiment have been discussed recently [76,77]. Lattice determinations of g_A^N are known to be sensitive to excited state contributions, finite volume effects and other systematics. Whereas there is a long history of lattice QCD calculations of g_A^N, see, e.g., the FLAG 21 review [78], there are very few lattice computations of hyperon axial charges [22–26] and only few phenomenological estimates exist from measurements of semileptonic hyperon decay rates.

We carry out simultaneous continuum, quark mass and finite volume fits to the individual baryon charges employing the parametrization in Eq. (31) [with the continuum form in Eq. (30)]. The discretization effects are found to be fairly mild and we are not able to resolve the quadratic mass dependent terms or a cubic term. These terms are omitted throughout. As already mentioned in Sec. III F we are also not able to resolve any higher order ChPT terms in the continuum parametrization.

A five parameter fit, with free coefficients $\{c_0, c_\pi, c_K, c_V, c_a\}$, describes the data well, as demonstrated in Fig. 17 for the nucleon (with $\chi^2/N_{\text{dof}} = 0.86$) and

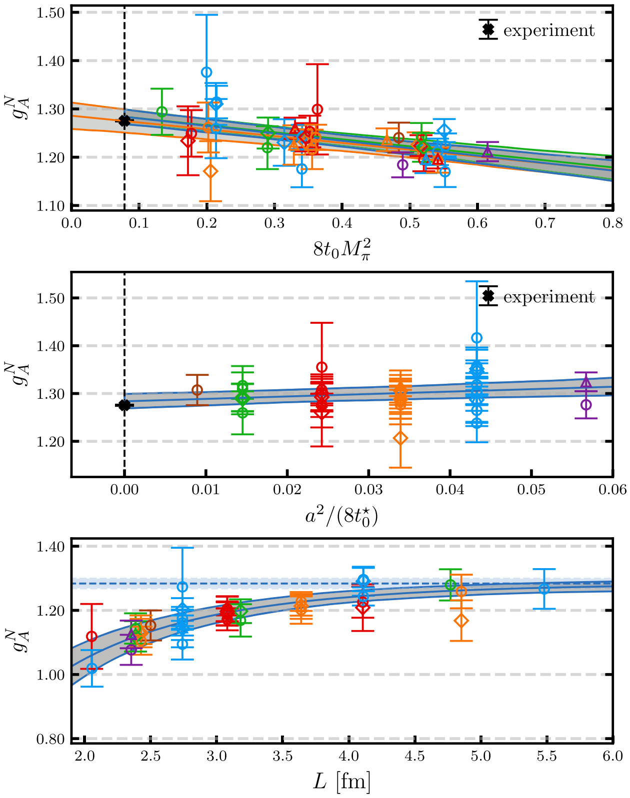

FIG. 17. Simultaneous quark mass, continuum and finite volume extrapolation of the nucleon isovector axial charge g_A^N extracted on ensembles with $M_\pi < 400$ MeV using two excited states in the fitting analysis (see Sec. III D) and renormalization factors Z_A^3 (see Table VII). A five parameter fit form is employed, see the text. (Top) Pion mass dependence of g_A^N, where the data points are corrected, using the fit, for finite volume and discretization effects and shifted (depending on the ensemble) to kaon masses corresponding to the $\text{tr}\, M = \text{const}$ and $m_s = \text{const}$ trajectories. The fit is shown as a gray band with the three trajectories distinguished by blue ($\text{tr}\, M = \text{const}$, circles), green ($m_s = \text{const}$, diamonds) and orange ($m_s = m_\ell$, triangles) lines, respectively. The vertical dashed line indicates the physical point. (Middle) Lattice spacing dependence at the physical point in the infinite volume limit. (Bottom) Finite volume dependence at the physical point in the continuum limit. The dashed blue line (band) indicates the infinite volume result. For better visibility, the data points for ensembles D150, E250, and D452, which have relatively large errors (see Table XVI), are not displayed. The black cross at the physical point indicates the experimental value [75].

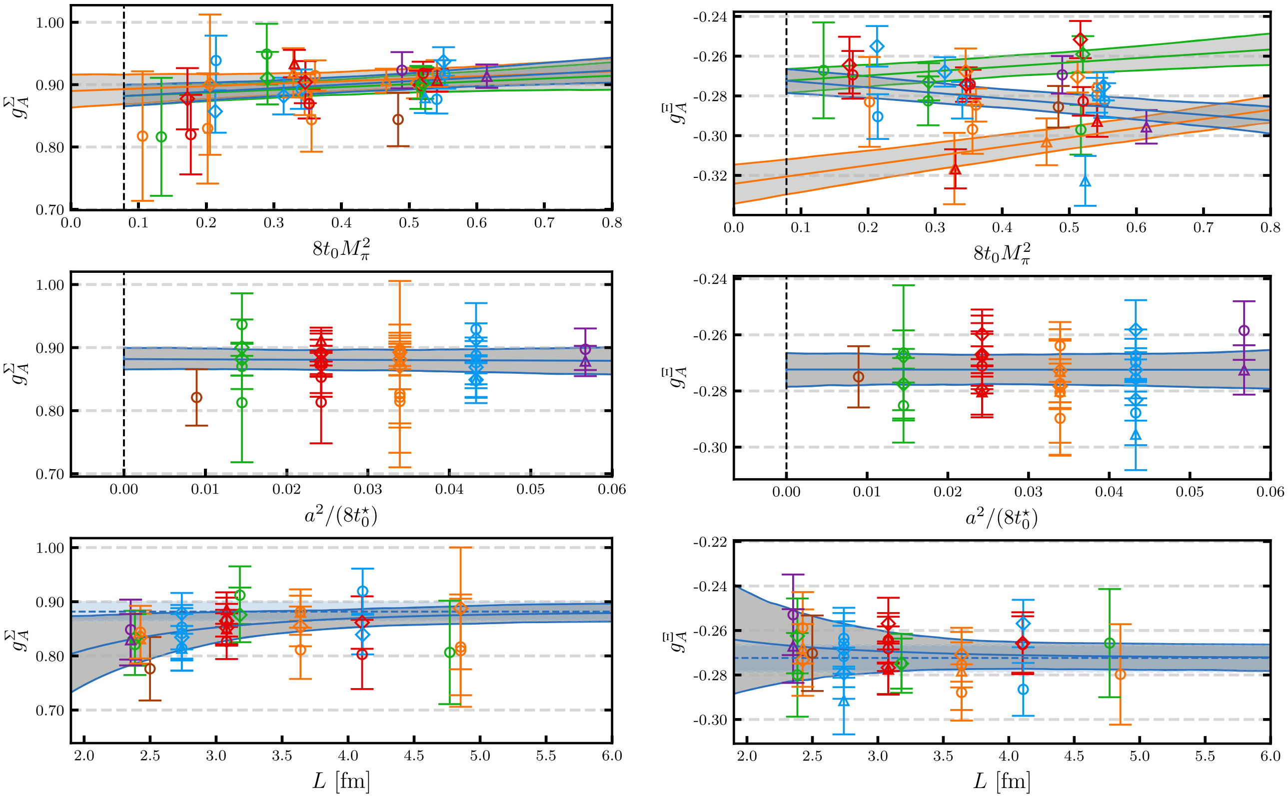

FIG. 18. The same as Fig. 17 for the isovector axial charges g_A^B of the sigma baryon (left) and the cascade baryon (right). For better visibility, the data points for ensembles D452 and D451, which have relatively large errors (see Table XVIII), are not displayed for the cascade baryon. Compared to the nucleon, for the analysis of the hyperon charges a reduced set of ensembles is employed, see Tables XVII and XVIII for a complete list of ensembles.

Fig. 18 for the sigma and cascade baryons (with $\chi^2/N_{\rm dof} = 0.85$ and 1.25, respectively). The data are extracted using two excited states (ES = 2) in the fitting analysis (see Sec. III D) and renormalized with factors Z_A^3 (that are the most precise of the three determinations considered, see Table VII). For the cascade baryon, with two strange quarks, the data on the three quark mass trajectories (tr M = const, m_s = const and $m_\ell = m_s$) are clearly delineated, however, note the different scale on the right of Fig. 18. The availability of ensembles on two trajectories which intersect at the physical point helps to constrain the physical value of the axial charge. In terms of the finite volume effects, only the nucleon shows a significant dependence on the spatial extent. The quark mass dependence is also pronounced in this case.

As in the vector case, we quantify the systematics associated with the extraction of the charges at the physical point (in the continuum and infinite volume limits) by varying the parametrization and the set of ensembles that are included in the fit. We consider two fit forms $(1, \{c_0, c_\pi, c_K, c_V, c_a\})$ and $(2, \{c_0, c_\pi, c_K, c_V, c_a, \delta c_a\})$ and four datasets, DS($M_\pi^{<400\text{ MeV}}$), DS($M_\pi^{<300\text{ MeV}}$), DS($M_\pi^{<400\text{ MeV}}, a^{<0.1\text{ fm}}$) and DS($M_\pi^{<400\text{ MeV}}, LM_\pi^{>4}$), see Sec. III F for their definitions.

The results of the eight fits and their model averages for the three different determinations of the renormalization factors are shown in Fig. 19 for the nucleon and in Fig. 43 of Appendix C for the hyperon axial charges. In all cases, we find consistent results across the different fits and choice of renormalization factor suggesting that the statistical errors dominate. The additional lattice spacing term is not really resolved with the goodness of fit only changing slightly, while the errors on the coefficients increase. For the nucleon and sigma baryon, all fits have a $\chi^2/N_{\rm dof} < 1$ and are given a similar weight in the model average, while for the cascade baryon, the cut $M_\pi^{<300\text{ MeV}}$ is needed to achieve a goodness of fit around 1 and these fits have the highest weight factors.

In order to further explore the systematics, additional datasets are considered. We assess the sensitivity of the results to excited state contributions by performing extrapolations of the data extracted using only one excited state ("ES=1") in the fitting analysis. In addition, as only the $O(p^2)$ ChPT terms are included in the continuum parametrization, we test the description of the quark mass dependence by performing 10 fits, involving the two parametrization variations above, applied to five datasets, DS(0), DS($M_\pi^{<400\text{ MeV}}$), DS($M_\pi^{<300\text{ MeV}}$), DS($a^{<0.1\text{ fm}}$) and

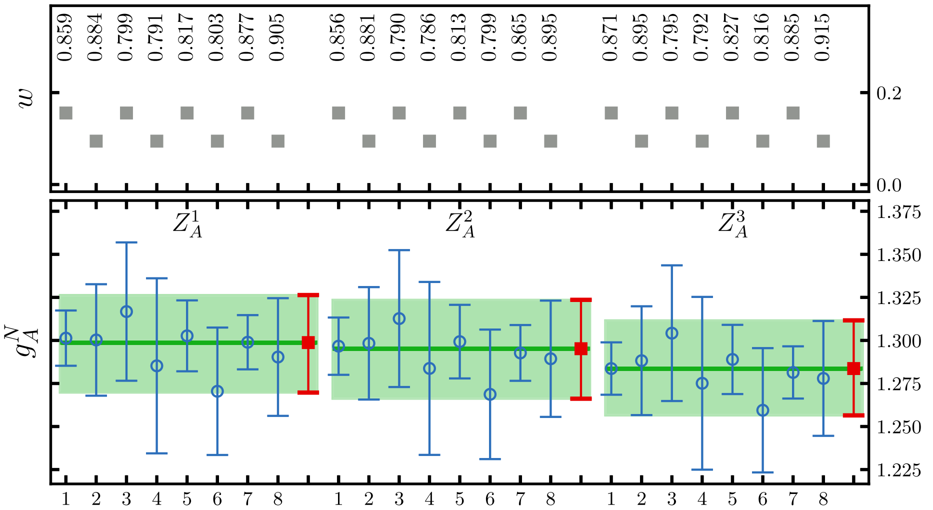

FIG. 19. The same as Fig. 15 for the nucleon axial charge g_A^N. The eight fits correspond to two fit variations, see the text, applied to four datasets, $\mathrm{DS}(M_\pi^{<400\text{ MeV}})$, $\mathrm{DS}(M_\pi^{<300\text{ MeV}})$, $\mathrm{DS}(M_\pi^{<400\text{ MeV}}, a^{<0.1\text{ fm}})$ and $\mathrm{DS}(M_\pi^{<400\text{ MeV}}, LM_\pi^{>4})$. The data are extracted using two excited states in the fitting analysis, see Sec. III D.

$\mathrm{DS}(LM_\pi^{>4})$. The first, fourth and fifth datasets include ensembles with pion masses up to 430 MeV.

The results for the axial charges from model averaging the 10 fits (denoted $\mathcal{A}$) employing the 5 datasets and also from the 8 fits (denoted $\mathcal{B}$) using the 4 datasets given above, for the ES = 1 and ES = 2 data and the different renormalization factors are displayed in Fig. 20. Very little variation is seen in the results in terms of the range of pion masses included and, as before, the renormalization factors employed, suggesting the associated systematics are accounted for within the combined statistical and systematic error (which includes the uncertainty due to lattice spacing and finite volume effects). However, the results are sensitive to the number of excited states included in the fitting analysis. This is only a significant effect for the nucleon, for which the ES = 1 results lie around 2.5σ below experiment. Similar underestimates of g_A^N have been observed in many earlier lattice studies [78].

As detailed in Sec. III D, more than one excited state is contributing significantly to the ratio of three-point over two-point correlation functions and including two excited states in the fitting analysis enables the ground state matrix element to be isolated more reliably. Considering the pion mass cuts, to be conservative we take the results of the model averages of the $\mathcal{B}$ datasets (where all the ensembles have $M_\pi < 400$ MeV) as only the dominant mass dependent terms are included in the continuum parametrization. Our estimates, corresponding to the (ES = 2, $\mathcal{B}$, Z_A^k) results in Fig. 20, are listed in Table X.

C. Scalar charges

As there is no isovector scalar current interaction at tree-level in the Standard Model, the scalar charges cannot be measured directly in experiment. However, the conserved vector current (CVC) relation can be used to estimate the

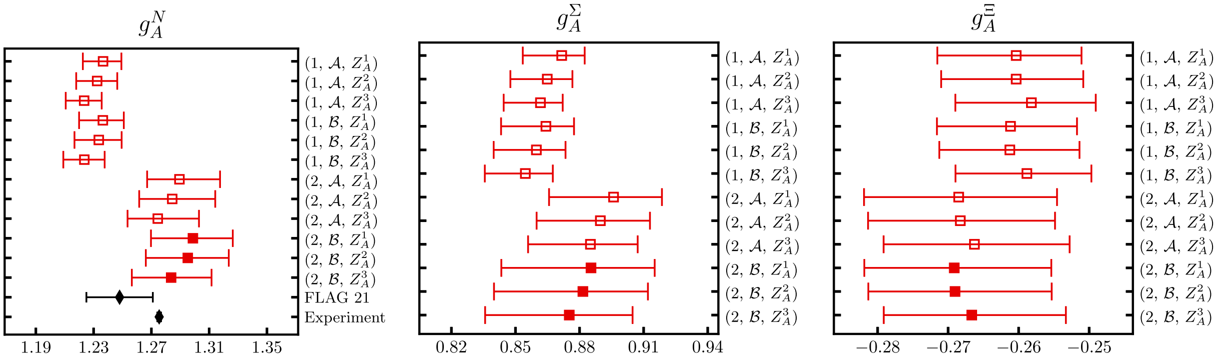

FIG. 20. The same as Fig. 16 for the nucleon, sigma and cascade axial charges. The label $\mathcal{A}$ indicates that 10 fits enter the model average corresponding to two fit variations, see the text, applied to 5 datasets, DS(0), $\mathrm{DS}(M_\pi^{<400\text{ MeV}})$, $\mathrm{DS}(M_\pi^{<300\text{ MeV}})$, $\mathrm{DS}(a^{<0.1\text{ fm}})$ and $\mathrm{DS}(LM_\pi^{>4})$. For the data points labeled with $\mathcal{B}$, the results of the 8 fits employed in Fig. 19 are averaged. For the nucleon, the FLAG 21 average for $N_f = 2 + 1$ [53,79] and the experimental value [75] are indicated (black diamonds).

TABLE X. Results for g_A^B, $B \in \{N, \Sigma, \Xi\}$, obtained with three different sets of renormalization factors. The errors include the statistical and all the systematic uncertainties.

Renormalization	g_A^N	g_A^Σ	g_A^Ξ
Z_A^1 (Table V)	$1.299^{(28)}_{(29)}$	$0.885^{(30)}_{(42)}$	$-0.269^{(14)}_{(13)}$
Z_A^2 (Table VI)	$1.295^{(28)}_{(29)}$	$0.882^{(30)}_{(42)}$	$-0.269^{(14)}_{(12)}$
Z_A^3 (Table VII)	$1.284^{(28)}_{(27)}$	$0.875^{(30)}_{(39)}$	$-0.267^{(13)}_{(12)}$

charges from determinations of the up and down quark mass difference, $\delta_m = m_u - m_d$, and the QCD contribution to baryon mass isospin splittings, e.g., between the mass of the proton and the neutron, $\Delta m_N^{\mathrm{QCD}}$, (for g_S^N see Eq. (55) below). Reference [80] finds $g_S^N = 1.02(11)$ employing lattice estimates for δ_m and an average of lattice and phenomenological values for $\Delta m_N^{\mathrm{QCD}}$, which is consistent with the FLAG 21 [78] $N_f = 2 + 1$ result of $g_S^N = 1.13(14)$ [53]. Estimates can also be made of the isovector scalar charges of the other octet baryons, see the discussion in Sec. V A. Conversely, direct determinations of the scalar charges can be used to predict δ_m, as presented in Sec. V C. So far, there has been only one previous study of the hyperon scalar charges [26].

For the extrapolation of the scalar charges and the extraction of the value at the physical point, we follow the same procedures as for the axial channel, presented in the previous subsection. The five parameter fit (with coefficients $\{c_0, c_\pi, c_K, c_V, c_a\}$) can again account for the observed quark mass, lattice spacing and volume dependence as illustrated in Fig. 21 for the nucleon (with $\chi^2/N_{\mathrm{dof}} = 0.56$) and Fig. 46 of Appendix C for the sigma and cascade baryons (with $\chi^2/N_{\mathrm{dof}} = 0.97$ and 1.14, respectively). The data are extracted using two excited states in the fitting analysis. For both hyperons, the quark mass and lattice spacing effects can be resolved, in contrast to the nucleon, while for all baryons the dependence on the spatial volume is marginal. When investigating the systematics in the estimates of the charges at the physical point, we perform model averages of the results of ($\mathcal{A}$): 8 fits from the two fit variations (as for the axial case) and the four datasets, DS(0), DS($M_\pi^{<400\ \mathrm{MeV}}$), DS($a^{<0.1\ \mathrm{fm}}$) and DS($LM_\pi^{>4}$), ($\mathcal{B}$): 6 fits from the two fit variations to the three datasets DS($M_\pi^{<400\ \mathrm{MeV}}$), DS($M_\pi^{<400\ \mathrm{MeV}}, a^{<0.1\ \mathrm{fm}}$) and DS($M_\pi^{<400\ \mathrm{MeV}}$, $LM_\pi^{>4}$). Note that a cut on the pion mass $M_\pi < 300$ MeV is not considered. The scalar matrix elements are generally less precise than the axial ones and utilizing such a reduced dataset leads to instabilities in the extrapolation and spurious values of the coefficients.

For illustration, the values from the individual fits and the model averages over the $\mathcal{B}$ datasets for the two different determinations of the renormalization factors are given in Fig. 44 in Appendix C. The results are consistent across the different fits, although the weights vary. The values of the scalar charges for all the model averages performed are compiled in Fig. 22. There are no significant variations in the results obtained using the different renormalization factors and datasets ($\mathcal{A}$ or $\mathcal{B}$). For the nucleon, there is also agreement between the values for the data extracted including one (ES = 1) or two (ES = 2) excited states in the fitting analysis and consistency with the current FLAG 21 result. For the sigma baryon, and to a lesser extent for the cascade baryon, there is a tension between the ES = 1 and ES = 2 determinations. As discussed previously, the ("ES = 2," $\mathcal{B}$, Z_S^k) values are considered the most reliable. These are listed in Table XI.

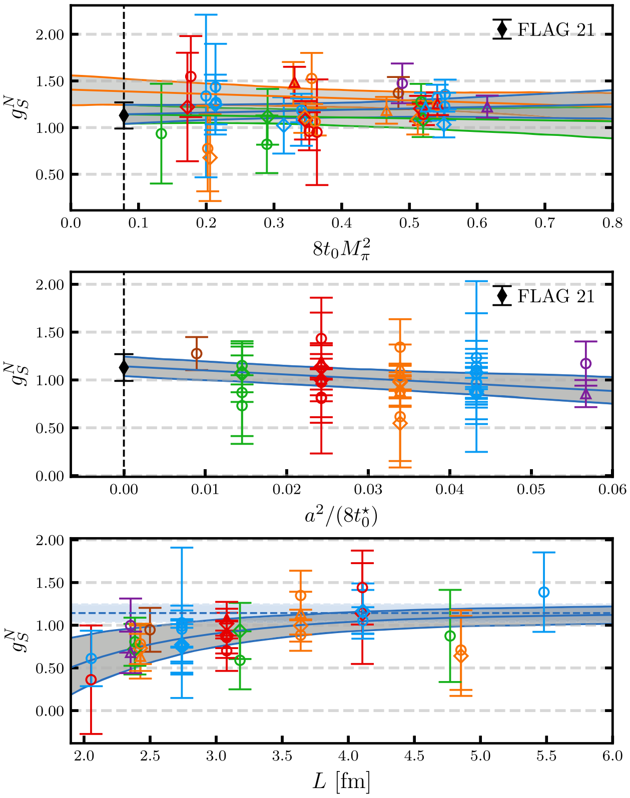

FIG. 21. The same as Fig. 17 for the nucleon scalar charge g_S^N. The factors Z_S^1 are used for the matching (see Table V). For orientation, the FLAG 21 result for $N_f = 2 + 1$ [53] is indicated (black diamond) at the physical point. For better visibility, the data points for ensembles D150, E250, and D452, which have relatively large errors (see Table XVI), are not displayed.

TABLE XI. Results for g_S^B, $B \in \{N, \Sigma, \Xi\}$, obtained with two different sets of renormalization factors. The errors include the statistical and all the systematic uncertainties.

Renormalization	g_S^N	g_S^Σ	g_S^Ξ
Z_S^1 (Table V)	$1.11^{(14)}_{(16)}$	$3.98^{(22)}_{(24)}$	$2.57^{(11)}_{(11)}$
Z_S^2 (Table VI)	$1.12^{(14)}_{(17)}$	$4.00^{(23)}_{(24)}$	$2.57^{(11)}_{(11)}$

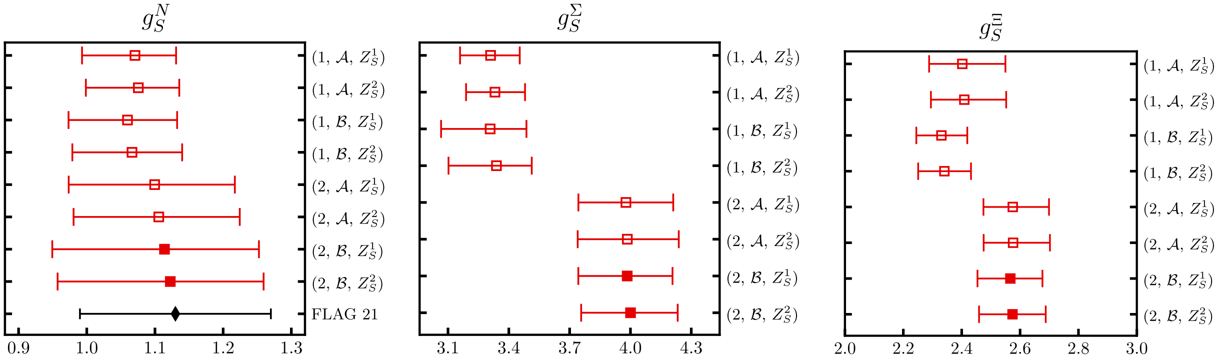

FIG. 22. The same as Fig. 16 for the nucleon, sigma and cascade scalar charges. The label $\mathcal{A}$ indicates that 8 fits enter the model average corresponding to two fit variations, see the text, applied to 4 datasets, DS(0), DS($M_\pi^{<400\ \mathrm{MeV}}$), DS($a^{<0.1\ \mathrm{fm}}$) and DS($LM_\pi^{>4}$). For the data points labeled with $\mathcal{B}$, the two fit variations are performed on 3 datasets, DS($M_\pi^{<400\ \mathrm{MeV}}$), DS($M_\pi^{<400\ \mathrm{MeV}}, a^{<0.1\ \mathrm{fm}}$) and DS($M_\pi^{<400\ \mathrm{MeV}}, LM_\pi^{>4}$), giving a total of 6 fits for the average. For the nucleon, the FLAG 21 result for $N_f = 2 + 1$ [53] is also shown (black diamond).

D. Tensor charges

In the isosymmetric limit, the nucleon tensor charge is equal to the first moment of the nucleon isovector transversity parton distribution function. Due to the lack of experimental data, estimates of g_T^N from phenomenological fits have very large uncertainties, unless some assumptions are made. In fact, in some analyses, the fit is constrained to reproduce the lattice results for the isovector charge, see Refs. [14,15]. The FLAG 21 review [78] gives as the $N_f = 2 + 1$ value for the nucleon tensor charge the result of Ref. [53], $g_T^N = 0.965(61)$, whereas, as far as we know, there is only one previous study of the hyperon tensor charges [26].

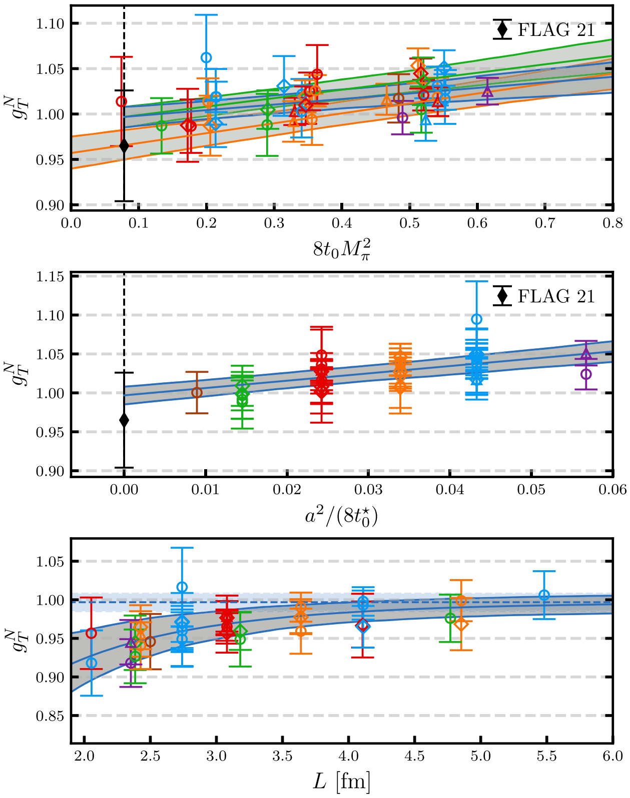

FIG. 23. The same as Fig. 17 for the nucleon tensor charge g_T^N. The factors Z_T^1 are used for the matching (see Table V). For orientation, the FLAG 21 result for $N_f = 2 + 1$ [53] is indicated (black diamond) at the physical point. For better visibility, the data points for ensembles D150 and D452, which have relatively large errors (see Table XVI), are not displayed.

The extraction of the octet baryon tensor charges at the physical point follows the analysis of the axial charges in Sec. IV B. In particular, the parametrizations employed and the datasets considered are the same. Figure 23 displays a typical example of an extrapolation for the nucleon tensor charge for a five parameter fit with a $\chi^2/N_{\mathrm{dof}} = 0.63$. See Fig. 47 in Appendix C for the analogous figures for the sigma and cascade baryons. The variation of the fits with the parametrization and the datasets utilized and the corresponding model averages, for the datasets with pion mass cut $\mathcal{B}$ (see Sec. IV B), are shown in Fig. 45.

An overview of the model averaged results for all variations of the input data is given in Fig. 24. The agreement between the different determinations suggests the systematics associated with the extrapolation are under control. Although the results utilizing data extracted with two excited states (ES = 2) in the fitting analysis are consistently above or below those extracted from the ES = 1 data, considering the size of the errors of the model averages (which combine the statistical and systematic uncertainties), the differences are not significant. Our estimates for the tensor charges, corresponding to the (ES = 2, $\mathcal{B}$, Z_T^k) values, are listed in Table XII.

V. DISCUSSION OF THE RESULTS

Our values for the vector, axial, scalar and tensor charges of the nucleon, sigma and cascade baryons are given in

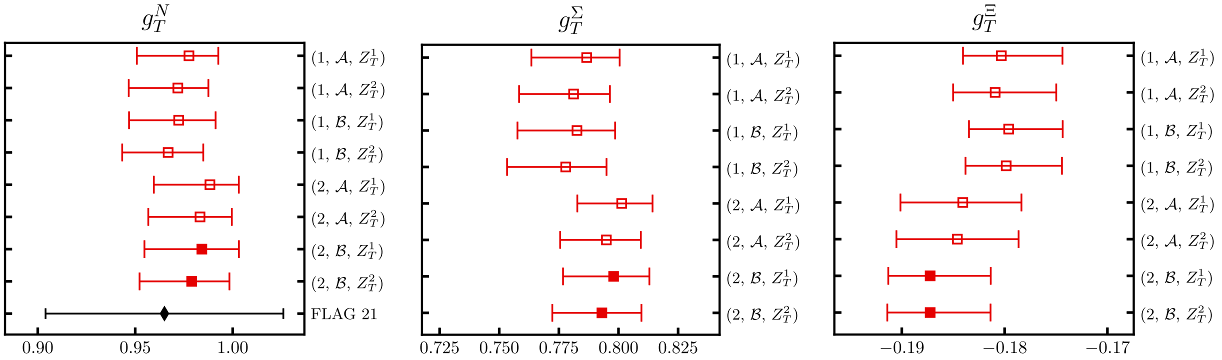

FIG. 24. The same as Fig. 16 for the nucleon, sigma and cascade tensor charges. For the nucleon, the FLAG 21 result for $N_f = 2 + 1$ [53] is also shown (black diamond).

Tables IX–XII, respectively. In each case, we take the most precise value as our final result, i.e., the one obtained using Z_V^3 and Z_A^3 for the vector and axial channels, respectively, and Z_S^1 and Z_T^1 for the scalar and the tensor. In the following we compare with previous determinations of the charges taken from the literature and discuss the SU(3) flavor symmetry breaking effects in the different channels. We use the conserved vector current relation and our result for the scalar charge of the sigma baryon to determine the up and down quark mass difference. We compute the QCD contributions to baryon isospin mass splittings and evaluate the isospin breaking effects on the pion baryon σ terms.

A. Individual charges

We first consider the axial charges. Our final values read

$$g_A^N = 1.284^{(28)}_{(27)}, \quad g_A^\Sigma = 0.875^{(30)}_{(39)}, \quad g_A^\Xi = -0.267^{(13)}_{(12)}. \qquad (37)$$

The result for the nucleon compares favorably with the experimental value $g_A^N/g_V^N = 1.2754(13)$ [75] and the FLAG 21 [78] average for $N_f = 2 + 1$, $g_A^N = 1.248(23)$. The latter is based on the determinations in Refs. [53,79]. All sources of systematic uncertainty must be reasonably under control to be included in the FLAG average and a number of more recent studies incorporate continuum, quark mass and finite volume extrapolations. A compilation of results for g_A^N is displayed in Fig. 25. Although the determinations are separated in terms of the number of dynamical fermions employed, including charm quarks in the sea is not expected to lead to a discernible effect.

Regarding the hyperon axial charges, far fewer works exist. Lin *et al.* [22,92] performed the first study, utilizing $N_f = 2 + 1$ ensembles with pion masses ranging between 350 MeV and 750 MeV and a single lattice spacing of 0.12 fm. After an extrapolation to the physical pion mass they obtain $g_A^\Sigma = 0.900(42)_{\text{stat}}(54)_{\text{sys}}$ and $g_A^\Xi = -0.277(15)_{\text{stat}}(19)_{\text{sys}}$, where estimates of finite volume and discretization effects are included in the systematic uncertainty. Note that we have multiplied their result for g_A^Σ by a factor of two to match our normalization convention. In Refs. [24,93] ETMC determined all octet and decuplet

TABLE XII. Results for g_T^B, $B \in \{N, \Sigma, \Xi\}$, obtained with two different sets of renormalization factors. The errors include the statistical and all the systematic uncertainties.

Renormalization	g_T^N	g_T^Σ	g_T^Ξ
Z_T^1 (Table V)	$0.984^{(19)}_{(29)}$	$0.798^{(15)}_{(21)}$	$-0.1872^{(59)}_{(41)}$
Z_T^2 (Table VI)	$0.979^{(19)}_{(27)}$	$0.793^{(17)}_{(21)}$	$-0.1872^{(59)}_{(42)}$

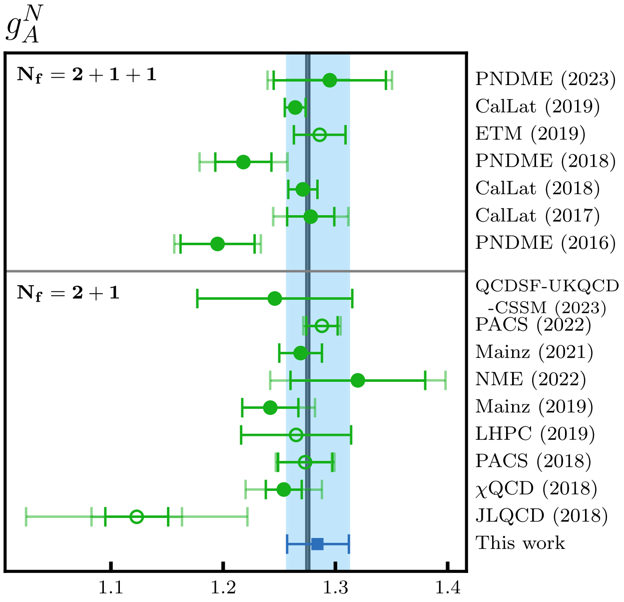

FIG. 25. Compilation of recent lattice determinations of the nucleon axial charge g_A^N with $N_f = 2 + 1$ [26,53,79,81–86] and $N_f = 2 + 1 + 1$ [68,69,87–91] dynamical fermions. Values with filled symbols were obtained via a chiral, continuum and finite volume extrapolation. The vertical black line gives the experimental result [75].

(i.e., nucleon, hyperon and Δ) axial couplings employing $N_f = 2+1+1$ ensembles with pion masses between 210 MeV and 430 MeV and two lattice spacings $a \in \{0.065\ \mathrm{fm}, 0.082\ \mathrm{fm}\}$. Using a simple linear ansatz for the quark mass extrapolation, they quote $g_A^\Sigma = 0.7629(218)_{\mathrm{stat}}$ and $g_A^\Xi = -0.2479(87)_{\mathrm{stat}}$, where the errors are purely statistical.

More recently, Savanur *et al.* [25] extracted the axial charges on $N_f = 2+1+1$ ensembles with three different lattice spacings $a \in \{0.06\ \mathrm{fm}, 0.09\ \mathrm{fm}, 0.12\ \mathrm{fm}\}$, pion masses between 135 MeV and 310 MeV and volumes in the range $3.3 \le LM_\pi \le 5.5$. The ratios g_A^Σ/g_A^N and g_A^Ξ/g_A^N are extrapolated taking the quark mass dependence and lattice spacing and finite volume effects into account. The experimental value of g_A^N is then used to obtain $g_A^\Sigma = 0.891(11)_{\mathrm{stat}}(13)_{\mathrm{sys}}$ (again multiplied by a factor of two to meet our conventions) and $g_A^\Xi = -0.2703(47)_{\mathrm{stat}}(13)_{\mathrm{sys}}$. Finally, QCDSF-UKQCD-CSSM presented results for the isovector axial, scalar and tensor charges in Ref. [26]. They employ $N_f = 2+1$ ensembles lying on a $\mathrm{tr}\, M = \mathrm{const}$ trajectory with pion masses ranging between 220 MeV and 470 MeV and five different values of the lattice spacing in the range (0.052–0.082) fm. The Feynman-Hellmann theorem is used to calculate the baryon matrix elements. Performing an extrapolation to the physical mass point including lattice spacing and finite volume effects, they find $g_A^\Sigma = 0.876(26)_{\mathrm{stat}}(09)_{\mathrm{sys}}$ and $g_A^\Xi = -0.206(22)_{\mathrm{stat}}(19)_{\mathrm{sys}}$.

We also mention the earlier studies of Erkol *et al.* [23] ($N_f = 2$), utilizing pion masses above 500 MeV, and QCDSF-UKQCD ($N_f = 2+1$) carried out at a single lattice spacing [94].

In Fig. 26 we compare the ratios of the hyperon axial charges to the nucleon axial charge, g_A^B/g_A^N, from Refs. [22,24,25], obtained on individual ensembles to our results. A comparison of the charges themselves cannot be made since, as mentioned above, Savanur *et al.* only present results for the ratio. As the strange quark mass is held approximately constant in these works, only our results from the $m_s = \mathrm{const}$ trajectory are displayed. Similarly, the QCDSF-UKQCD-CSSM values are omitted as the ensembles utilized lie on a $\mathrm{tr}\, M = \mathrm{const}$ trajectory. We observe reasonable agreement between the data. Note that our continuum, infinite volume limit result (the gray band in the figure) for g_A^Σ/g_A^N lies slightly below the central values of most of our $m_s = \mathrm{const}$ data points.

The individual hyperon axial charges at the physical point are shown in Fig. 27, along with a number of phenomenological determinations employing a variety of quark models [95–97], the chiral soliton model [98] and SU(3) covariant baryon ChPT [67]. Within errors, the lattice results are consistent apart from the rather low value for g_A^Σ from ETMC [24] and the rather high value for g_A^Ξ from QCDSF-UKQCD-CSSM [26]. The phenomenological estimates for g_A^Σ are in

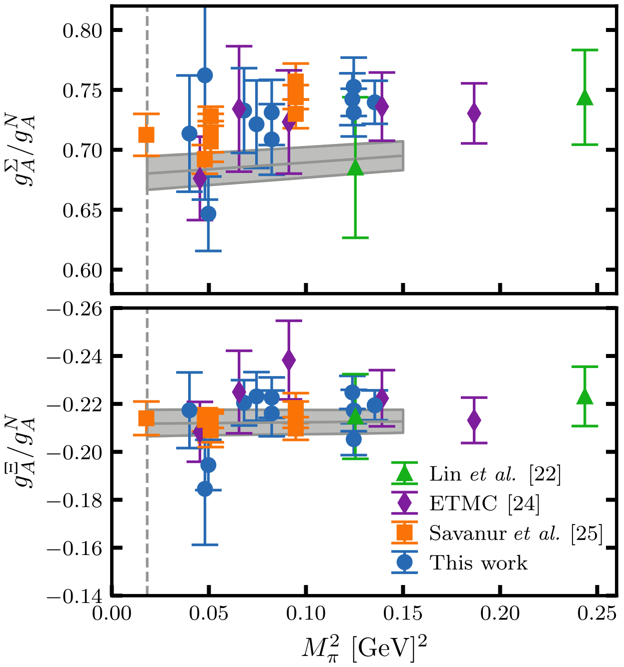

FIG. 26. Comparison of lattice determinations [22,24,25] of the hyperon axial charges for the Σ and Ξ baryons normalized to the nucleon axial charge. Some of the results from Lin *et al.* at heavier pion masses are not shown. The gray vertical dashed line indicates the physical pion mass point. Only our results from the $m_s = \mathrm{const}$ trajectory are shown. The gray bands indicate the (continuum limit, infinite volume) quark mass behavior according to the fits displayed in Figs. 17 and 18. Note that the data points are not corrected for finite volume or discretization effects. All data are converted to our phase and normalization conventions, Eqs. (1)–(6). The Lin *et al.* and ETMC results are obtained by taking the ratio of the individual charges and employing error propagation.

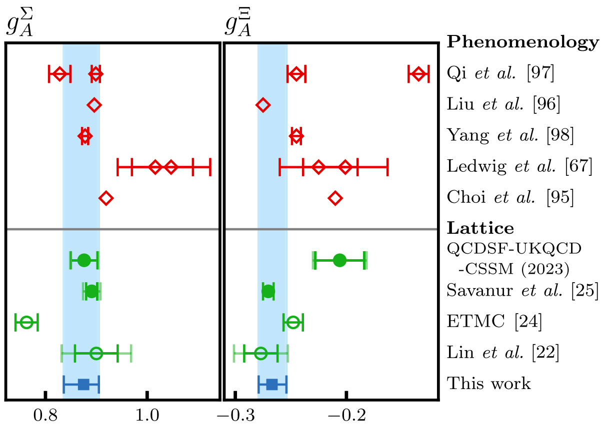

FIG. 27. Comparison of our results for the axial charges g_A^Σ and g_A^Ξ (blue symbols and error bands) with other lattice determinations [22,24–26] and phenomenological estimates [67,95–98]. Values with filled symbols were obtained via a chiral, continuum and finite volume extrapolation. All results are converted to our phase and normalization conventions, Eqs. (1)–(6).

reasonable agreement with our value, while there is a large spread in the expectations for g_A^Ξ.

We remark that, in analogy to the CVC relation (discussed in Sec. V C below), the axial Ward identity, $\partial_\mu(\bar{u}\gamma_\mu\gamma_5 d) = i(m_d + m_u)\bar{u}\gamma_5 d$, connects the axial and pseudoscalar charges,

$$g_P^B = \frac{m_B}{m_\ell} g_A^B, \tag{38}$$

where m_B and m_ℓ correspond to the baryon and the light quark mass, respectively. This relation was employed in Ref. [80] to determine the pseudoscalar charge of the nucleon, which is defined as the pseudoscalar form factor in the forward limit. Taking the baryon masses of isosymmetric QCD from Table 14 of Ref. [17] and the isospin averaged light quark mass $m_\ell = 3.381(40)$ MeV in the $N_f = 4$ flavor $\overline{\mathrm{MS}}$ scheme at $\mu = 2$ GeV from the FLAG 21 review [78], we find

$$g^N_{P,N_f=4} = 356^{(9)}_{(9)}, \qquad g^\Sigma_{P,N_f=4} = 308^{(11)}_{(14)},$$
$$g^\Xi_{P,N_f=4} = -104^{(5)}_{(5)}. \tag{39}$$

Turning to the scalar charges, our final results in the three flavor $\overline{\mathrm{MS}}$ scheme at $\mu = 2$ GeV read[5]

$$g_S^N = 1.11^{(14)}_{(16)}, \quad g_S^\Sigma = 3.98^{(22)}_{(24)}, \quad g_S^\Xi = 2.57^{(11)}_{(11)}. \tag{40}$$

For the nucleon, our result for g_S^N agrees with the FLAG 21 value $g_S^N = 1.13(14)$ for $N_f = 2 + 1$ [78] (taken from Ref. [53]) and more recent lattice determinations, see Fig. 28. There is only one previous lattice determination of the hyperon scalar couplings by QCDSF-UKQCD-CSSM [26], who obtain $g_S^\Sigma = 2.80(24)_{\mathrm{stat}}(05)_{\mathrm{sys}}$ and $g_S^\Xi = 1.59(11)_{\mathrm{stat}}(04)_{\mathrm{sys}}$. These values are much smaller than ours.

One can also employ the CVC relation and estimates of the QCD contribution to the isospin mass splittings and the light quark mass difference to determine the scalar charges. For a detailed discussion see Sec. V C below. Reference [80] obtains $g_S^N = 1.02(11)$ assuming $\Delta m_N^{\mathrm{QCD}} = m_p^{\mathrm{QCD}} - m_n^{\mathrm{QCD}} = -2.58(18)$ MeV and the quark mass difference $\delta_m = m_u - m_d = -2.52(19)$ MeV. Similarly, using the results by BMWc on the light quark mass splitting [108] and their QCD contributions to the baryon mass splittings [109], we obtain

$$g_S^N = 1.05(13), \quad g_S^\Sigma = 3.35(19), \quad g_S^\Xi = 2.29(15), \tag{41}$$

which agree with our results to within two standard deviations. Note that a smaller value for $|\delta_m|$ (see Sec. V C) would uniformly increase these charges.

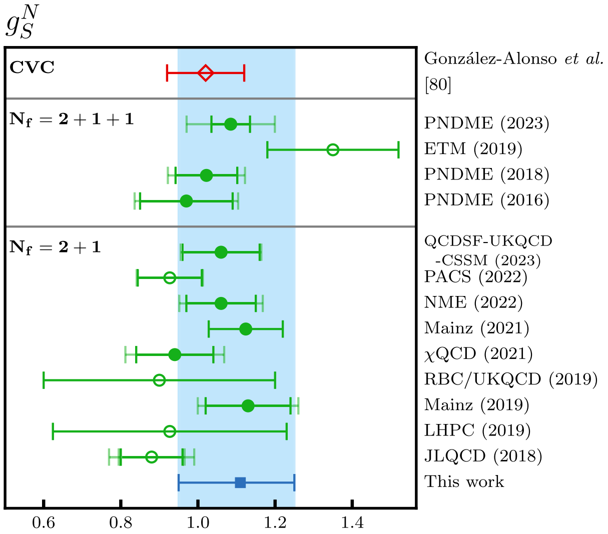

FIG. 28. As in Fig. 25 for the nucleon scalar charge g_S^N with $N_f = 2 + 1$ [26,53,81,83–86,106,107] and $N_f = 2 + 1 + 1$ [69,87,89,91] dynamical fermions. González-Alonso *et al.* estimate the scalar charge via the conserved vector current (CVC) relation [80].

Regarding the tensor charges we find in the $N_f = 3$ $\overline{\mathrm{MS}}$ scheme at $\mu = 2$ GeV

$$g_T^N = 0.984^{(19)}_{(29)}, \quad g_T^\Sigma = 0.798^{(15)}_{(21)}, \quad g_T^\Xi = -0.1872^{(59)}_{(41)}. \tag{42}$$

Since the anomalous dimension of the tensor bilinear is smaller than for the scalar case, we would expect no statistically relevant difference between the $N_f = 3$ and $N_f = 4$ schemes at $\mu = 2$ GeV. The nucleon charge agrees with the FLAG 21 [78] value of $g_T^N = 0.965(61)$ [53] for $N_f = 2 + 1$ and other recent lattice studies. These are shown in Fig. 29 along with determinations from phenomenology. The large uncertainties of the latter reflect the lack of experimental data. In particular, in Refs. [14,15] the JAM collaboration constrain the first Mellin moment of the isovector combination of the transverse parton distribution functions to reproduce a lattice result for g_T^N. QCDSF-UKQCD-CSSM also determined the hyperon tensor charges 26]]. Their results $g_T^\Sigma = 0.805(15)_{\mathrm{stat}}(02)_{\mathrm{sys}}$ and $g_T^\Xi = -0.1952(74)_{\mathrm{stat}}(10)_{\mathrm{sys}}$ are in good agreement with ours.

---

[5] Using Version 3 of RunDec [99], we compute the conversion factor from $N_f = 3$ to $N_f = 4$: $1.00082(2)_\Lambda(1)_{\mathrm{pert}}(56)_{m_c} = 1.0008(6)$. The errors reflect the uncertainty of the Λ-parameter [100], the difference between 5-loop running [101,102]/4-loop decoupling [103–105] and 4-loop running/3-loop decoupling and a 200 MeV uncertainty in the charm quark on-shell mass, respectively: at $\mu = 2$ GeV there is no noteworthy difference between $N_f = 3$ and $N_f = 4$ $\overline{\mathrm{MS}}$ pseudo(scalar) charges.

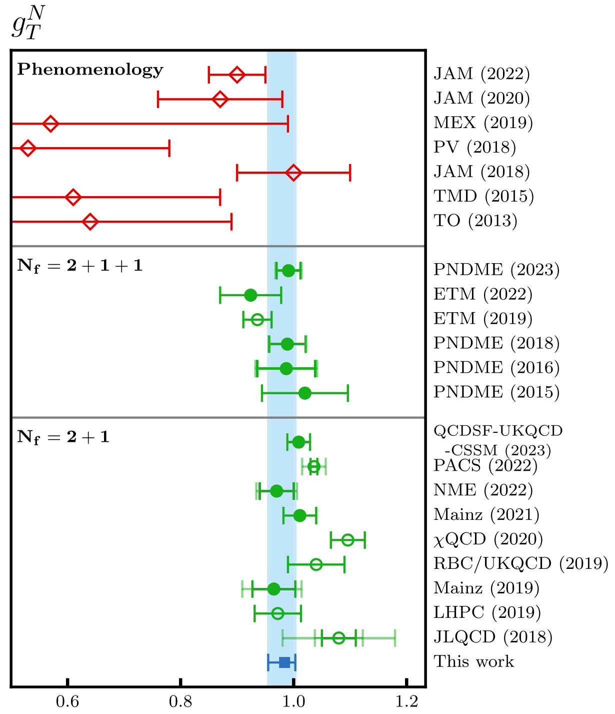

FIG. 29. As in Fig. 25 for the nucleon tensor charge g_T^N with $N_f = 2+1$ [26,53,81,83–86,106,110] and $N_f = 2+1+1$ [69,87,89,91,111,112] dynamical fermions. Recent phenomenological estimates are also displayed for comparison [14,15,113–117]. Values with filled symbols were obtained via a quark mass, continuum and finite volume extrapolation. In addition, the filled ETM (2022) [112] point is obtained from a continuum limit extrapolation of results determined on three physical point ensembles with large spatial volumes.

B. SU(3) flavor symmetry breaking

On the SU(3) flavor symmetric line, i.e., for $m = m_\ell = m_s$, the baryon charges $g_J^B(m)$ can be decomposed into two functions, $F_J(m)$ and $D_J(m)$, see Sec. II and Eqs. (8)–(10). For the axial charges g_A^B, the values of these functions in the SU(3) chiral limit correspond to the LECs $F = F_A(0)$ and $D = D_A(0)$. We will not consider the vector channel $(J = V)$ here since $F_V(m) = 1$ and $D_V(m) = 0$, which holds even at $m_s \neq m_\ell$, due to charge conservation.

Estimates of baryon structure observables often rely on SU(3) flavor symmetry arguments, however, it is not known *a priori* to what extent this symmetry is broken for $m_s \neq m_\ell$ and, in particular, at the physical point. Since within this analysis, we only determined three isovector charges $(B \in \{N, \Sigma, \Xi\})$ for each channel $(J \in \{A, S, T\})$, we cannot follow the systematic approach to investigate SU(3) flavor symmetry breaking of matrix elements proposed in Ref. [29]. Nevertheless, constructing appropriate ratios from the individual charges will provide us with estimates of the flavor symmetry breaking effects for each channel.

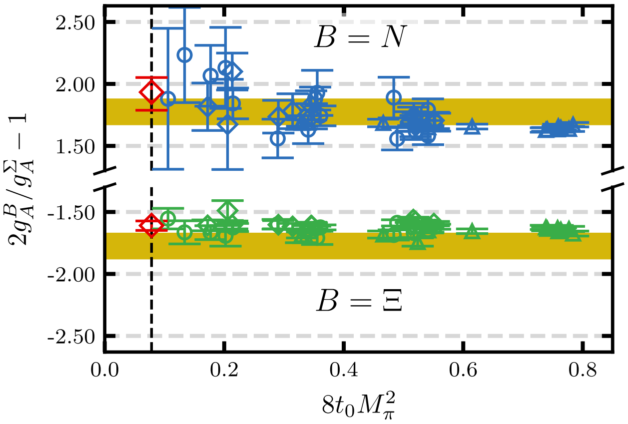

FIG. 30. The ratios $2g_A^B/g_A^\Sigma - 1$ for $B \in \{N, \Xi\}$ as a function of the pion mass squared. The latter are rescaled with the Wilson flow scale t_0. The red diamonds are the continuum and infinite volume limit results at the physical point (indicated by the dashed vertical line) obtained from our extrapolations of the individual charges. The yellow bands depict the corresponding $m_s = m_\ell = 0$ predictions $\pm D/F$. Circles (diamonds) correspond to the $\mathrm{tr}\, M = \text{const.}$ $(m_s = \text{const.})$ trajectories, the triangles to the $m_s = m_\ell$ line. The data are not corrected for lattice spacing or volume effects.

Using Eqs. (8)–(10), we obtain for $m = m_s = m_\ell$

$$\frac{2g_J^B(m)}{g_J^\Sigma(m)} - 1 = \pm \frac{D_J(m)}{F_J(m)}, \tag{43}$$

where "+" and "−" corresponds to $B = N$ and $B = \Xi$, respectively. Figure 30 shows these combinations for the axial charges, as functions of the squared pion mass, compared to the chiral, continuum limit expectations $\pm D/F$ (yellow bands) determined from our global fit (see Fig. 18 and Table XIII). The chiral limit value agrees with our earlier result $D/F = 1.641^{(27)}_{(44)}$ [64] (model averaging recomputed for D/F instead of F/D) within 1.5 standard errors. The data shown in the figure are not corrected for volume or lattice spacing effects. Note that the

TABLE XIII. The combinations $2g_J^B/g_J^\Sigma - 1$ of Eq. (43) with $B \in \{N, \Xi\}$ at the physical point, in the continuum and infinite volume limit. These are computed from the individual charges in Tables X (for Z_A^3), XI and XII (for Z_J^1). The last row gives the combination $D_J(0)/F_J(0)$ in the chiral, continuum and infinite volume limit (yellow bands in Figs. 30–32), computed from the individual charges: $D_J/F_J = (g_J^N - g_J^\Xi)/g_J^\Sigma$.

B	$2g_A^B/g_A^\Sigma - 1$	$2g_S^B/g_S^\Sigma - 1$	$2g_T^B/g_T^\Sigma - 1$
N	$1.93^{(12)}_{(15)}$	$-0.441^{(76)}_{(89)}$	$1.467^{(67)}_{(99)}$
Ξ	$-1.609^{(37)}_{(40)}$	$0.288^{(91)}_{(96)}$	$-1.469^{(17)}_{(16)}$
$D_J(0)/F_J(0)$	$1.79^{(11)}_{(8)}$	$-0.416^{(46)}_{(49)}$	$1.530^{(54)}_{(56)}$

renormalization factors and improvement coefficients and, possibly, other systematics cancel from Eq. (43). For the ratio of the Ξ over the Σ axial charge we see no significant difference between the physical point value and that obtained for the same average quark mass at the flavor symmetric point. The symmetry breaking effect of the combination involving g_A^N/g_A^Σ can be attributed to the pion mass dependence of g_A^N, see Fig. 17. The red symbols at the physical point (dashed vertical line) correspond to our continuum, infinite volume limit extrapolated results, listed in Table XIII for the combinations Eq. (43).

In Fig. 31 the combinations Eq. (43) are shown for the isovector scalar charges. These are compared to our SU(3) chiral limit extrapolated results (yellow bands) and the continuum, infinite volume limit results at the physical point (red diamonds). We find no statistically significant symmetry breaking in this case. However, the statistical errors are larger than for the axial case and also $F_S > F_A$. Therefore, we cannot exclude symmetry breaking of a similar size as for the axial charges, in particular, in the ratio of the Ξ over the Σ baryon charge. Finally, in Fig. 32 we carry out the same comparison for the tensor charges. In this case, within errors of a few percent, no flavor symmetry violation is seen. Moreover, $D_T(m)/F_T(m) = D_T(0)/F_T(0)$ within errors.

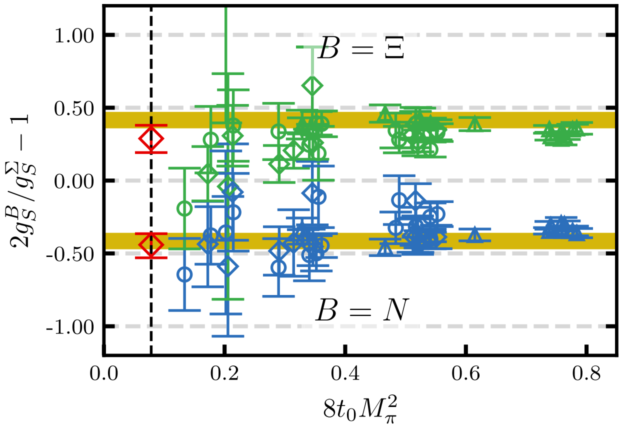

FIG. 31. The same as Fig. 30 for the scalar channel. The yellow bands depict the $m_s = m_\ell = 0$ predictions $\pm D_S(0)/F_S(0)$ obtained from the extrapolations of the individual charges.

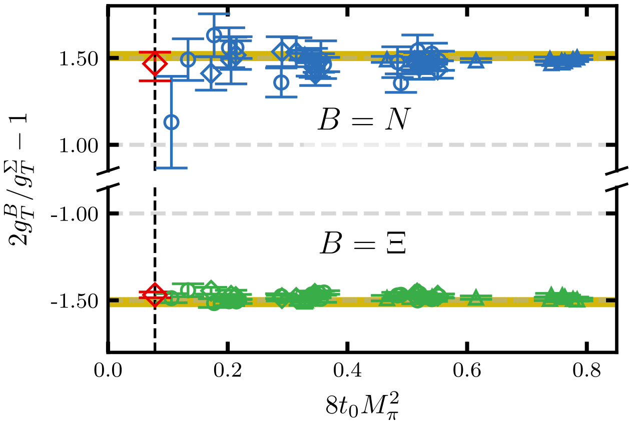

FIG. 32. The same as Fig. 30 for the tensor channel.

In order to quantify the symmetry breaking effect between matrix elements involving the current J as a function of the quark mass splitting $m_s - m_\ell$, we define

$$\delta^J_{\rm SU(3)} = \frac{g_J^\Xi + g_J^N - g_J^\Sigma}{g_J^\Xi + g_J^N + g_J^\Sigma}, \tag{44}$$

where for $m_s = m_\ell$, $\delta^J_{\rm SU(3)} = (2F_J - 2F_J)/(2F_J + 2F_J) = 0$, see Eqs. (8)–(10). Also from these ratios some of the systematics as well as the renormalization factors and improvement terms will cancel. We define a dimensionless SU(3) breaking parameter $x = (M_K^2 - M_\pi^2)/(2M_K^2 + M_\pi^2) \sim m_s - m_\ell$ and assume a polynomial dependence:

$$\delta^J_{\rm SU(3)} = \sum_{n>0} a_n^J x^n. \tag{45}$$

The data for $\delta^A_{\rm SU(3)}(x)$ depicted in Fig. 33 become more and more positive as the physical point (vertical dashed line) is approached. This observation agrees with findings from earlier studies [22–26]. We fit to data for which the average quark mass is kept constant (blue circles). However, there is no significant difference between these and the $m_s \approx$ const points (black squares). Both linear and quadratic fits in x ($a_n^A = 0$ for $n \neq 1$ and $a_n^A = 0$ for $n \neq 2$, respectively) give

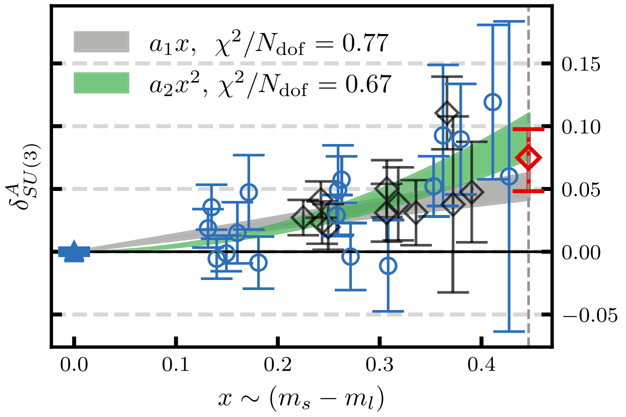

FIG. 33. The SU(3) symmetry breaking ratio $\delta^A_{\rm SU(3)}(x)$ [Eq. (45)] for the axial charges as a function of $x = (M_K^2 - M_\pi^2)/(2M_K^2 + M_\pi^2)$. Circles (diamonds) correspond to the tr M = const (m_s = const) trajectories, the triangle to $m_s = m_\ell$. The gray (green) band shows the result from a linear (quadratic) one parameter fit including only the blue data points that correspond to the ensembles on the tr M = const line. Black data points correspond to ensembles on the m_s = const trajectory. The vertical gray dashed line indicates the physical point. The red diamond corresponds to the result derived from the values for the individual charges, see Sec. V A.

adequate descriptions of the data and agree with our continuum, infinite volume limit extrapolated physical point result (red diamond)

$$\delta^A_{\mathrm{SU}(3)} = 0.075^{(23)}_{(27)}, \tag{46}$$

derived from the values for the individual charges. Effects of this sign and magnitude were also reported previously. ETMC [24] find $g_A^N + g_A^\Xi - g_A^\Sigma = 0.147(24)$, whereas Savanur and Lin [25] quote $(g_A^N + g_A^\Xi - g_A^\Sigma)/g_A^N = 0.087(15)$.

For $J \neq A$ no statistically significant effects were observed. Nevertheless, for completeness we carry out the same analysis for $J = S$ and $J = T$, see Fig. 34. Our continuum, infinite volume limit extrapolated physical point results

$$\delta^S_{\mathrm{SU}(3)} = -0.040^{(37)}_{(41)}, \qquad \delta^T_{\mathrm{SU}(3)} = -0.001^{(16)}_{(23)} \tag{47}$$

provide upper limits on the relative size of SU(3) flavor violation at the physical point.

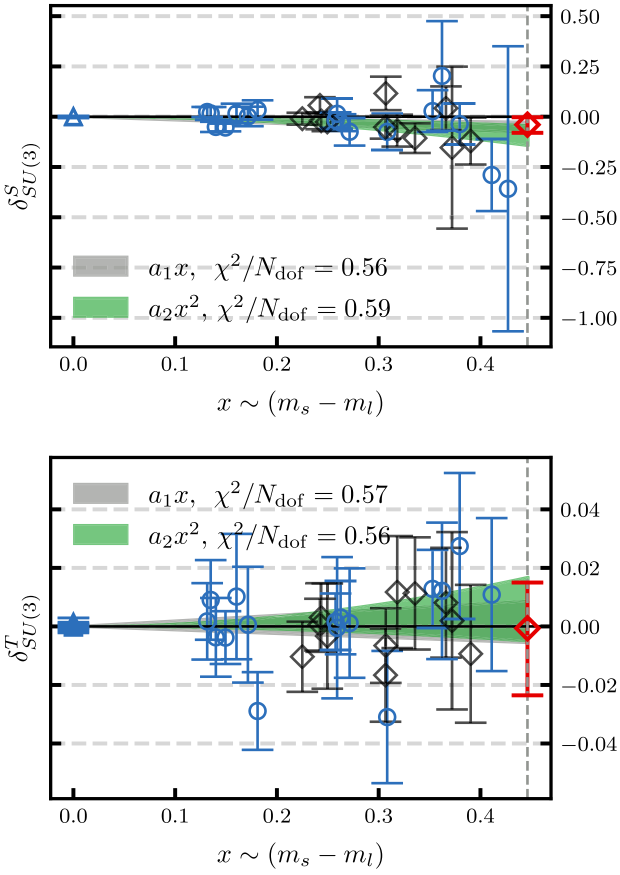

FIG. 34. The same as Fig. 33 for the scalar (top) and tensor (bottom) charges.

C. The up and down quark mass difference

Our results on the scalar charges, in particular, g_S^Σ, enable us to determine the quark mass splitting $\delta_m = m_u - m_d$. While we simulate the isosymmetric theory, in Nature this symmetry is broken. The extent of isospin symmetry breaking is determined by two small parameters, $\delta_m/\Lambda_{\mathrm{QCD}}$ and the fine structure constant α_{QED}, which are similar in size. The vector Ward identity relates δ_m to the QCD contributions to baryon mass splittings within an isomultiplet. In particular, to leading order in $\delta_m/\Lambda_{\mathrm{QCD}}$ and α_{QED}, the difference between the Σ^+ and Σ^- baryon masses is a pure QCD effect from which, with our knowledge of g_S^Σ, we can extract δ_m without additional assumptions.

We consider isospin multiplets of baryons $B^Q \in \{N^Q, \Sigma^Q, \Xi^Q\}$ with electric charges $Q = I_3 + \frac{1}{2}(1+S) \in \{0, \pm 1\}$ ($N^+ = p, N^0 = n$) and define the mass differences $\Delta m_{B^{Q+1}} = m_{B^{Q+1}} - m_{B^Q}$. Note that for the Σ there are two differences [75],

$$\Delta m_{\Sigma^+} = m_{\Sigma^+} - m_{\Sigma^0} = -3.27(7)\ \mathrm{MeV}, \tag{48}$$

$$\Delta m_{\Sigma^0} = m_{\Sigma^0} - m_{\Sigma^-} = -4.81(4)\ \mathrm{MeV}. \tag{49}$$

The other splittings read [75]

$$\Delta m_\Xi = -6.85(21)\ \mathrm{MeV}, \qquad \Delta m_N \approx -1.293\ \mathrm{MeV}. \tag{50}$$

The mass differences can be split into QCD ($\sim\delta_m$) and QED ($\sim\alpha_{\mathrm{QED}}\Lambda_{\mathrm{QCD}}$) contributions:

$$\Delta m_B = \Delta m_B^{\mathrm{QCD}} + \Delta m_B^{\mathrm{QED}}. \tag{51}$$

The splitting depends on the scale, the renormalization scheme and the matching conventions between QCD and QCD + QED. The Cottingham formula [118] relates the leading QED contribution to hadron masses to the total electric charge squared times a function of the unpolarized Compton forward-amplitude, i.e., to leading order in α_{QED} the electric contribution to charge-neutral hadron masses should vanish (as was suggested in the massless limit by Dashen [119]). Moreover, for $\delta_m = 0$ this implies that the leading QED contributions to the masses of the Σ^+ and Σ^- baryons are the same. Therefore, up to $\mathcal{O}(\alpha_{\mathrm{QED}}, \delta_m/\Lambda_{\mathrm{QCD}}) \cdot \delta_m$ terms,

$$\begin{aligned}\Delta m_\Sigma^{\mathrm{QCD}} &= \frac{1}{2}(m_{\Sigma^+} - m_{\Sigma^-}) \\ &= -4.04(4)\ \mathrm{MeV},\end{aligned} \tag{52}$$

$$\begin{aligned}\Delta m_{\Sigma^+}^{\mathrm{QED}} &= \frac{1}{2}(m_{\Sigma^+} + m_{\Sigma^-}) - m_{\Sigma^0} \\ &= 0.77(5)\ \mathrm{MeV} = -\Delta m_{\Sigma^0}^{\mathrm{QED}}.\end{aligned} \tag{53}$$

From the Ademollo-Gatto theorem [74] we know that the leading isospin breaking effects on the vector charges $g_V^N = g_V^\Xi = 1$ and $g_V^\Sigma = 2$ are quadratic functions of $\delta_m/\Lambda_{\mathrm{QCD}}$ and α_{QED}, whereas the scalar charges g_S^B are subject to linear corrections in α_{QED} and $\delta_m/\Lambda_{\mathrm{QCD}}$.

The Lorentz decomposition of the on-shell QCD matrix element for the isovector vector current between baryons $B' = B^{Q+1}$ and $B = B^Q$ (that differ by $\Delta I_3 = 1$ in their isospin) gives [see Eq. (1)]

$$\begin{aligned} i\partial^\mu \langle B'(p')|\bar{d}\gamma_\mu u|B(p)\rangle &= g_V^{B'B} i\partial^\mu \bar{u}_{B'}(p')\gamma_\mu u_B(p) \\ &= g_V^{B'B}\Delta m_B^{\mathrm{QCD}}[1+\mathcal{O}(\delta_m/\Lambda_{\mathrm{QCD}})], \end{aligned} \tag{54}$$

where the leading correction is due to $q_0 = p_0' - p_0 = \Delta m_B^{\mathrm{QCD}} = |\mathbf{q}|$. In the last step we used the equations of motion. Combining this with the vector Ward identity $i\partial^\mu \bar{d}\gamma_\mu u = (m_u - m_d)\bar{d}u$ gives

$$g_V^{B'B}\Delta m_B^{\mathrm{QCD}} = g_S^{B'B}(m_u - m_d) \tag{55}$$

as the QCD contribution to the mass difference, with corrections that are suppressed by powers of the symmetry breaking parameters. Note that the normalization convention of the charges g_J^B defined in Eq. (3),

$$g_J^{pn} = g_J^N, \qquad g_J^{\Sigma^+\Sigma^0} = -g_J^\Sigma/\sqrt{2}, \qquad g_J^{\Xi^0\Xi^-} = -g_J^\Xi,$$

cancels in the above equation so that we can replace $g_J^{B'B} \mapsto g_J^B$ to obtain

$$\delta_m = m_u - m_d = \frac{g_V^B}{g_S^B}\Delta m_B^{\mathrm{QCD}}, \tag{56}$$

which we refer to as the CVC relation.[6]

Using our physical point, continuum and infinite volume limit result $g_S^\Sigma = 3.98^{(22)}_{(24)}$, assuming $g_V^\Sigma = 2$ and applying Eq. (56) for the Σ baryon, we obtain in the $N_f = 3$ $\overline{\mathrm{MS}}$ scheme at $\mu = 2$ GeV

$$m_u - m_d = -2.03^{(12)}_{(12)}\ \mathrm{MeV}. \tag{57}$$

TABLE XIV. Comparison of the light quark mass difference.

	N_f	δ_m/MeV
RM123 [121]	$2+1+1$	$-2.38(18)$
FNAL-MILC[a] [122]	$2+1+1$	$-2.55^{(9)}_{(7)}$
MILC[a] [123]	$2+1+1$	$-2.57^{(11)}_{(6)}$
BMWc [108]	$2+1$	$-2.41(12)$
This work	$2+1$	$-2.03(12)$

[a] FNAL-MILC [122] and MILC [123] only quote the ratios $m_u/m_d = 0.4556^{(131)}_{(93)}$ and $m_u/m_d = 0.4529^{(157)}_{(82)}$, respectively (all errors added in quadrature). Using the FLAG 21 [78] average $m_\ell = 3.410(43)$, we combine these results to form $\delta_m = 2m_\ell(m_u/m_d - 1)/(m_u/m_d + 1)$ and compute the error by error propagation.

We expect $|\mathcal{O}(\delta_m/\Lambda_{\mathrm{QCD}}, \alpha_{\mathrm{QED}})| \lesssim 1\%$ corrections from higher order effects to this result, which we can neglect at the present level of accuracy.

We can compare our value of δ_m with results from the literature in Table XIV. This includes the $N_f = 2+1$ result of BMWc [108] and the $N_f = 2+1+1$ continuum limit results of RM123 [121], FNAL-MILC [122] and MILC [123]. In the latter two cases we convert results for m_u/m_d into δ_m as described in the table caption. We see a tension between the previous determinations and our result on the two to three σ level.

We remark that all the previous results utilize the dependence of the pion and kaon masses on the quark masses and the electromagnetic coupling. We consider our method of determining the quark mass splitting from the scalar coupling g_S^Σ and the mass difference between the Σ^+ and the Σ^- baryons as more direct. In Ref. [124] $\Delta m_N^{\mathrm{QCD}} = -1.87(16)$ MeV (which agrees within errors with lattice determinations, including ours, see below) is determined from experimental input. A larger (negative) QCD difference would require a larger QED contribution to the proton mass. As discussed above, the QED contribution to the mass of the Σ^+ baryon is 0.77(5) MeV (similar in size to $\Delta m_N^{\mathrm{QED}} = 0.58(16)$ MeV [124]) and it would be surprising if this increased when replacing a strange quark by a down quark. Assuming $\Delta m_N^{\mathrm{QCD}} = -1.87(16)$ MeV and a value $\delta_m \approx -2.50(10)$ MeV as suggested by Refs. [108,121–123] would require a coupling $g_S^N = 0.75(7)$ to satisfy the CVC relation Eq. (56). This in turn is hard to reconcile with the majority of lattice results compiled in Fig. 28. With a lower value for $|\delta_m|$ (and/or a larger $|\Delta m_N^{\mathrm{QCD}}|$) this inconsistency disappears.

D. QCD and QED isospin breaking effects on the baryon masses

We proceed to compute the QED contributions to the proton and Ξ^- masses, $\Delta m_N^{\mathrm{QED}}$ and $-\Delta m_\Xi^{\mathrm{QED}}$:

---

[6] Note that also the relations between $g_S^{B'B}$ and g_S^B receive $\mathcal{O}(\alpha_{\mathrm{QED}})$ corrections. Therefore terms $\propto m_\ell\alpha_{\mathrm{QED}}$, $\propto \delta_m\alpha_{\mathrm{QED}}$ and $\propto \delta_m^2/\Lambda_{\mathrm{QCD}}$ can be added to Eq. (56). Since m_ℓ is similar in size to δ_m, we can neglect the first of these terms too, whose appearance is related to the mixing in QCD + QED of m_ℓ and δ_m under renormalization. Using the $\overline{\mathrm{MS}}$ scheme at $\mu = 2$ GeV corresponds to the suggestion of Ref. [120], however, for quark masses $m_\ell \sim \delta_m$ this additional scale-dependence can be neglected with good accuracy, as pointed out above. In addition, there are small $\mathcal{O}(\alpha_{\mathrm{QED}}^2\Lambda_{\mathrm{QCD}})$ terms due to the QED contributions to the β- and γ-functions, which are also of higher order.

$$\Delta m_N^{\mathrm{QED}} = \Delta m_N - g_S^N(m_u - m_d) = \Delta m_N - \frac{2g_S^N}{g_S^\Sigma}\Delta m_\Sigma^{\mathrm{QCD}}, \tag{58}$$

$$\Delta m_\Xi^{\mathrm{QED}} = \Delta m_\Xi - \frac{2g_S^\Xi}{g_S^\Sigma}\Delta m_\Sigma^{\mathrm{QCD}}. \tag{59}$$

This gives

$$\Delta m_N^{\mathrm{QED}} = 0.97^{(31)}_{(36)}\ \mathrm{MeV}, \quad \Delta m_N^{\mathrm{QCD}} = -2.26^{(31)}_{(36)}\ \mathrm{MeV}, \tag{60}$$

$$\Delta m_\Sigma^{\mathrm{QED}} = 0.77(05)\ \mathrm{MeV}, \quad \Delta m_\Sigma^{\mathrm{QCD}} = -4.04(04)\ \mathrm{MeV}, \tag{61}$$

$$\Delta m_\Xi^{\mathrm{QED}} = -1.65^{(37)}_{(39)}\ \mathrm{MeV}, \quad \Delta m_\Xi^{\mathrm{QCD}} = -5.20^{(42)}_{(44)}\ \mathrm{MeV}. \tag{62}$$

For completeness we included the values for the Σ baryons that we determined from the experimental masses alone, without lattice input. The above mass splittings agree with the BMWc [109] continuum limit results from simulations of QCD plus QED, see Fig. 35 (errors added in quadrature). Nevertheless, as mentioned above, the value of δ_m, reported by BMWc [108] from simulations of QCD with quenched QED, differs by 2.2 standard deviations from our result in Eq. (57). Also other lattice results on the QCD contribution to the mass-splittings (summarized in Fig. 35), obtained at a single lattice spacing from Endres *et al.* [125] using $\mathrm{QED_{TL}}$ and $\mathrm{QED_M}$, Brantley *et al.* [126] and CSSM-QCDSF-UKQCD [127] agree within errors.

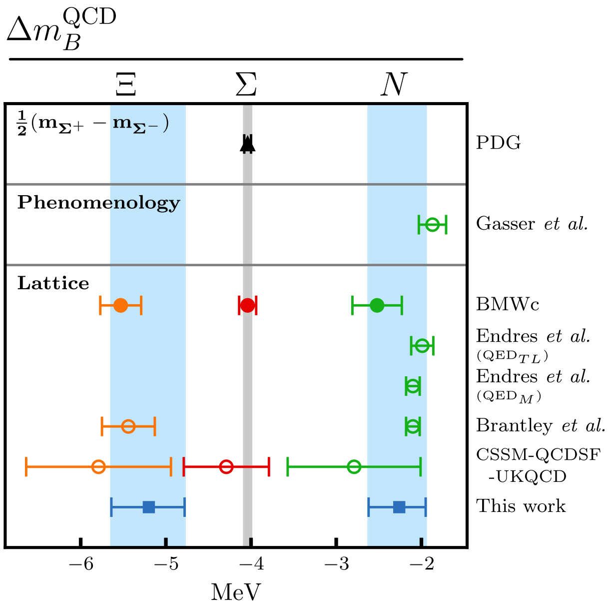

FIG. 35. Comparison of the QCD contributions to isospin mass splittings [75,109,124–127]. Note that in our normalization $m_{\Sigma^+} - m_{\Sigma^-} \approx 2\Delta m_\Sigma^{\mathrm{QCD}}$. Values with filled symbols were obtained via a quark mass, continuum and finite volume extrapolation. Endres *et al.* [125] only quote values for $\Delta m_N^{\mathrm{QED}}$ from which we compute $\Delta m_N^{\mathrm{QCD}}$ employing the experimental proton-neutron mass splitting.

We mention the possibility of an enhancement of the (higher order) $\delta_m^2/\Lambda_{\mathrm{QCD}}$ correction to the Σ^0 mass due to the possibility of mixing with the Λ^0, which, however, appears to be a very small effect [128]. A positive contribution to the Σ^0 mass would increase $\Delta m_\Sigma^{\mathrm{QED}}$ but leave $\Delta m_\Sigma^{\mathrm{QCD}}$ [and therefore the quark mass difference Eq. (57)] invariant.

The electromagnetic contributions to the p, $\Sigma^\pm$ and Ξ^- masses are all similar to 1 MeV, with an enhancement for the heavier, more compact cascade baryon. Recently, combining the Cottingham formula [118] with experimental input from elastic scattering and parton distribution functions, the value $\Delta m_N^{\mathrm{QED}} = 0.58(16)$ MeV was determined in Ref. [124]. While within errors our result Eq. (60) agrees with this value, the number obtained in Ref. [124] is more inline with the suggested ordering $\Delta m_N^{\mathrm{QED}} < \Delta m_\Sigma^{\mathrm{QED}} < -\Delta m_\Xi^{\mathrm{QED}}$. Combining their value with our determination of g_S^N gives $\delta_m = -1.69^{(28)}_{(26)}$MeV, somewhat smaller in modulus than our result Eq. (57) and certainly in tension with, e.g., $\delta_m = -2.41(12)$ MeV [108].

We find that the effect of $m_d > m_u$ on the Ξ and Σ mass splittings is much bigger than for the nucleon since this is proportional to g_S^B/g_V^B and $g_S^N < g_S^\Sigma/2 < g_S^\Xi$. This hierarchy is due to $g_S^N \approx F_S + D_S$, $g_S^\Sigma/2 \approx F_S$ and $g_S^\Xi \approx F_S - D_S$ with $F_S > 0$ and $D_S < 0$. Interestingly, the pion baryon σ terms $\sigma_{\pi B} = \sigma_{uB} + \sigma_{dB}$ that encode the up plus down quark mass contribution to the baryon masses exhibit the opposite ordering [17], $\sigma_{\pi N} > \sigma_{\pi\Sigma} > \sigma_{\pi\Xi}$.

E. Isospin breaking effects on the pion baryon σ terms

Having determined the quark mass differences, we can also compute the leading isospin violating corrections to the pion baryon σ terms $\sigma_{\pi B} = \sigma_{uB} + \sigma_{dB}$. One can either work with matrix elements [129], using the identity

$$m_u\bar{u}u + m_d\bar{d}d = m_\ell(\bar{u}u + \bar{d}d) + \frac{\delta_m}{2}(\bar{u}u - \bar{d}d), \tag{63}$$

or one can start from the Feynman-Hellmann theorem

$$\sigma_{qB} = m_q\frac{\langle B|\bar{q}q|B\rangle}{\langle B|B\rangle} = m_q\frac{\partial m_B}{\partial m_q}. \tag{64}$$

Writing $m_p = m_N + \Delta m_N^{\mathrm{QCD}}/2 + \Delta m_N^{\mathrm{QED}}$ and $m_n = m_N - \Delta m_N^{\mathrm{QCD}}/2$, where $\Delta m_N^{\mathrm{QCD}} = \delta_m g_S^N/g_V^N$, and realizing that the dependence of the QED contributions on the quark masses is of higher order in the isospin breaking, we obtain at linear order

$$\sigma_{\pi p} = m_u \frac{\partial m_p}{\partial m_u} + m_d \frac{\partial m_p}{\partial m_d} = \sigma_{\pi N} + \frac{1}{2}\Delta m_N^{\mathrm{QCD}}, \qquad (65)$$

$$\sigma_{\pi n} = m_u \frac{\partial m_n}{\partial m_u} + m_d \frac{\partial m_n}{\partial m_d} = \sigma_{\pi N} - \frac{1}{2}\Delta m_N^{\mathrm{QCD}}. \qquad (66)$$

The same can be carried out for the $\Sigma^{\pm}$, Ξ^0 and Ξ^- baryons. Using the results for the σ terms of the isosymmetric theory of Ref. [17], we obtain

$$\sigma_{\pi p} = 42.8^{(4.7)}_{(4.7)}\mathrm{MeV}, \qquad \sigma_{\pi n} = 45.0^{(4.7)}_{(4.7)}\mathrm{MeV}, \qquad (67)$$

$$\sigma_{\pi\Sigma^+} = 21.9^{(3.8)}_{(6.1)}\mathrm{MeV}, \qquad \sigma_{\pi\Sigma^-} = 29.9^{(3.8)}_{(6.1)}\mathrm{MeV}, \qquad (68)$$

$$\sigma_{\pi\Xi^0} = 8.6^{(4.5)}_{(6.4)}\mathrm{MeV}, \qquad \sigma_{\pi\Xi^-} = 13.8^{(4.5)}_{(6.4)}\mathrm{MeV}, \qquad (69)$$

whereas the pion σ term for the Σ^0 is not affected at linear order: $\sigma_{\pi\Sigma^0} \approx \sigma_{\pi\Sigma} = 25.9^{(3.8)}_{(6.1)}\mathrm{MeV}$. We refrain from further decomposing the pion baryon σ terms into the individual up and down quark contributions. However, this can easily be accomplished [129]. It is worth noting that $(\sigma_{\pi\Xi^-} - \sigma_{\pi\Xi^0})/\sigma_{\pi\Xi} \gg (\sigma_{\pi n} - \sigma_{\pi p})/\sigma_{\pi N}$, in spite of the same isospin difference.

VI. SUMMARY AND OUTLOOK

We determined the axial, scalar and tensor isovector charges of the nucleon, sigma and cascade baryons using $N_f = 2+1$ lattice QCD simulations. The analysis is based on 47 gauge ensembles, spanning a range of pion masses from 430 MeV down to a near physical value of 130 MeV across six different lattice spacings between $a \approx 0.039$ fm and $a \approx 0.098$ fm and linear spatial lattice extents $3.0 M_\pi^{-1} \leq L \leq 6.5 M_\pi^{-1}$. The availability of ensembles lying on three trajectories in the quark mass plane enables SU(3) flavor symmetry breaking to be explored systematically and the quark mass dependence of the charges to be tightly constrained. Simultaneous extrapolations to the physical point in the continuum and infinite volume limit are performed. Systematic errors are assessed by imposing cuts on the pion mass, the lattice spacing and the volume as well as using different sets of renormalization factors. Our results (in the $\overline{\mathrm{MS}}$ scheme at $\mu = 2$ GeV) for the nucleon charges are

$$g_A^N = 1.284^{(28)}_{(27)}, \qquad g_S^N = 1.11^{(14)}_{(16)}, \qquad g_T^N = 0.984^{(19)}_{(29)}.$$

For the hyperon charges we find

$$g_A^\Sigma = 0.875^{(30)}_{(39)}, \qquad g_S^\Sigma = 3.98^{(22)}_{(24)}, \qquad g_T^\Sigma = 0.798^{(15)}_{(21)},$$

$$g_A^\Xi = -0.267^{(13)}_{(12)}, \qquad g_S^\Xi = 2.57^{(11)}_{(11)}, \qquad g_T^\Xi = -0.1872^{(59)}_{(41)}.$$

A comparison with previous works is presented in Sec. V A. We quantify SU(3) symmetry breaking effects for the axial charge at the physical point in terms of the combination

$$\delta^A_{\mathrm{SU(3)}} = \frac{g_A^\Xi + g_A^N - g_A^\Sigma}{g_A^\Xi + g_A^N + g_A^\Sigma} = 0.075^{(23)}_{(27)},$$

see Fig. 33. In particular the axial charge of the nucleon deviates from its value in the SU(3) chiral limit, as can be seen in Fig. 30 and Table XIII. No significant symmetry breaking is observed for the other charges within current precision, see Figs. 31, 32, and 34.

To cross-check the analysis methods, the vector charges are determined and the expected values, $g_V^N = g_V^\Xi = 1$ and $g_V^\Sigma = 2$, are reproduced reasonably well:

$$g_V^N = 1.0012^{(12)}_{(11)}, \qquad g_V^\Sigma = 2.021^{(21)}_{(27)}, \qquad g_V^\Xi = 1.015^{(10)}_{(11)}.$$

Furthermore, we exploit the conserved vector current relation to predict the quark mass difference

$$m_u - m_d = -2.03(12)\ \mathrm{MeV}$$

from the scalar charge of the Σ baryon. We utilize this to decompose isospin mass splittings between the baryons into QCD and QED contributions [see Eqs. (60)–(62)] and to predict the leading isospin corrections to the pion baryon σ terms [see Eqs. (67)–(69)].

A computationally efficient stochastic approach was employed in the analysis, which allows for the simultaneous evaluation of the three-point correlation functions of all baryons with a variety of current insertions and momentum combinations. This work is a first step toward determining hyperon decay form factors which are relevant for the study of *CP* violation [130]. A complementary study of the baryon octet σ terms on the same dataset as used here is already ongoing [131].

ACKNOWLEDGMENTS

We thank all our coordinated lattice simulations (CLS) colleagues for discussions and the joint production of the gauge ensembles used. Moreover, we thank Benjamin Gläßle and Piotr Korcyl for their contributions regarding the (stochastic) three-point function code. S. C. and S. W. received support through the German Research Foundation (DFG) Grant CO 758/1-1. The work of G. B. was funded in part by the German Federal Ministry of Education and Research (BMBF) Grant No. 05P18WRFP1. Additional support from the European Union's Horizon 2020 research and innovation programme under the Marie Skłodowska-Curie Grant Agreement No. 813942 (ITN EuroPLEx) and Grant Agreement No. 824093 (STRONG 2020) is gratefully acknowledged, as well as initial stage funding through the German Research Foundation (DFG) collaborative research centre SFB/TRR-55. The authors gratefully acknowledge the Gauss Centre for Supercomputing (GCS) for providing computing time through the John von Neumann Institute for Computing (NIC) on the supercomputer JUWELS [132] and in particular on the Booster partition of the supercomputer JURECA [133] at Jülich Supercomputing Centre (JSC). GCS is the alliance of the three national supercomputing centres HLRS (Universität Stuttgart), JSC (Forschungszentrum Jülich), and LRZ (Bayerische Akademie der Wissenschaften), funded by the BMBF and the German State Ministries for Research of Baden-Württemberg (MWK), Bayern (StMWFK) and Nordrhein-Westfalen (MIWF). Additional simulations were carried out on the QPACE 3 Xeon Phi cluster of SFB/TRR-55 and the Regensburg Athene 2 Cluster. The authors also thank the JSC for their support and for providing services and computing time on the HDF Cloud cluster [134] at JSC, funded via the Helmholtz Data Federation (HDF) programme. Most of the ensembles were generated using openQCD [35] within the CLS effort. A few additional ensembles were generated employing the BQCD-code [39] on the QPACE supercomputer of SFB/TRR-55. For the computation of hadronic two- and three-point functions we used a modified version of the Chroma [135] software package along with the LibHadronAnalysis library and the multigrid solver implementation of Refs. [136,137] (see also Ref. [138]) as well as the IDFLS solver [139] of openQCD. We used Matplotlib [140] to create the figures.

APPENDIX A: FURTHER DETAILS OF THE THREE-POINT FUNCTION MEASUREMENTS

1. Comparison of the stochastic and sequential source methods

We computed the connected three-point functions for all the octet baryons utilizing the computationally efficient stochastic approach outlined in Sec. III C. This approach introduces additional stochastic noise on top of the gauge noise. In the analysis presented, for the nucleon, we make use of statistically more precise three-point correlation function measurements determined via the sequential source method as part of other projects. In the following, we compare the computational costs of the stochastic and the sequential source methods and the results for the ratios of the three-point over two-point functions for the nucleon.

As a typical example, we consider the measurements performed on ensemble N200 ($M_\pi = 286$ MeV and $a = 0.064$ fm). For our setup, illustrated in Figs. 6 and 7, a total of 4×12 solves are needed for the 4 source positions of the point-to-all propagators. To form the three-point functions for the nucleon an additional $N_{\mathrm{sto}} = 100$ light stochastic solves (for the time slice-to-all propagators connecting the sink and current time slices, the wiggly line in Fig. 6) are performed. This setup provides 8 measurements of the nucleon three-point function (as shown in Fig. 7, with the source-sink separations $t/a = 11$, 14, 16, 19) and includes all polarizations (and the unpolarized case) as well as a range of sink momenta (almost) for free. In principle, decuplet baryon three-point functions can also be constructed at the analysis stage. This setup is evaluated twice on each configuration leading to a total of 296 inversions. Similarly, an additional $(4 \times 12 + 100) \times 2$ strange solves are performed in order to form the three-point functions for all the (octet and decuplet) hyperons, including strangeness changing currents that we did not consider here.

In the sequential source setup, we compute the three-point function for the nucleon at rest, again for source-sink separations $t/a = 11$, 14, 16 and 19. Ten measurements are carried out per configuration (corresponding to 1, 2, 3 and 4 measurements for each t, respectively), where in each case the two light quark flavors (u and d) of the current and the four possible polarizations of the nucleon require 2×4 sequential sources to be constructed. This amounts to performing $(4 + 10 \times 2 \times 4) \times 12 = 1008$ light solves. The additional 4×12 inversions refer to the point-to-all propagators for 4 different source positions that connect the source to the sink (and the current). This is three-times the cost of the stochastic approach (for the nucleon three-point functions), which realizes a range of sink momenta.

The ratios of the three-point over two-point functions for the nucleon obtained from the two different approaches are compared in Fig. 36. A significant part of the gauge noise cancels in the ratio, while the (additional) stochastic noise remains. For our setup, this leads to larger statistical errors for the stochastic data compared to the sequential source results. This difference can clearly be seen for the ratio in the vector channel, for which the gauge noise is minimal, however, the difference is less pronounced for the other charges. For the sigma and cascade baryons we generally find a good statistical signal in the ratios employing the stochastic approach, see Fig. 37, although, also in this case the ratios for the hyperon vector charges suffer from large errors.

In the case of a large-scale analysis effort including high statistics, as presented in this article, the disk space required to store the stochastic three-point function data is significant. The individual spectator (S) and insertion (I) parts as defined in Eqs. (22) and (23), respectively, are stored with all indices open. In general this amounts to $N = N[S] + N[I]$ complex double precision floating point numbers for each gauge field configuration where

$$N[S] = N_F^S \cdot N_{\mathbf{p}'} \cdot N_{\mathrm{snk}} \cdot N_{\mathrm{src}} \cdot N_{\mathrm{sto}} \cdot N_c \cdot N_s^5, \qquad \text{(A1)}$$

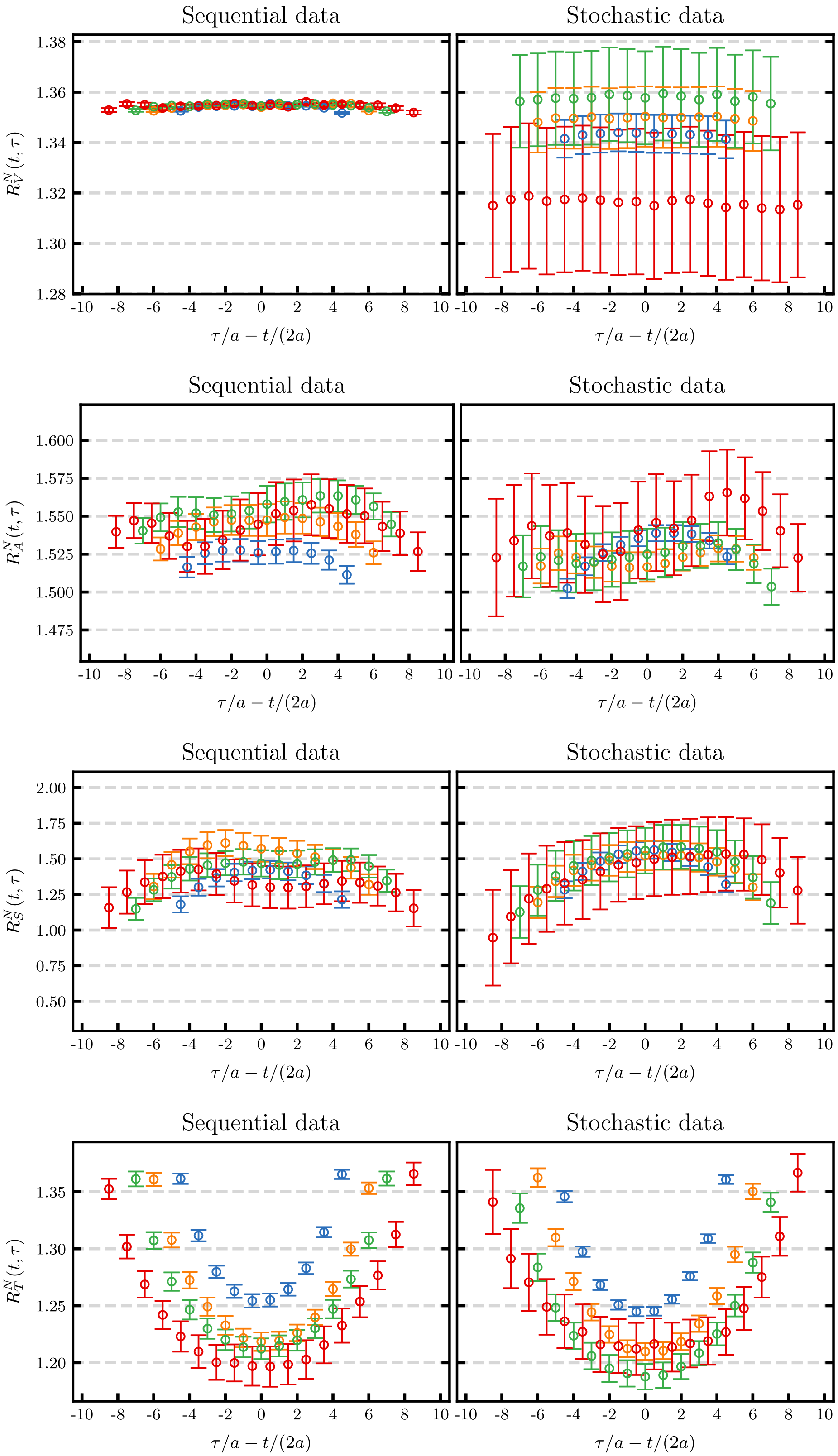

FIG. 36. Unrenormalized ratio of three-point over two-point functions for the nucleon vector, axial, scalar and tensor charge (from top to bottom) on ensemble N200. The left hand side shows the data from the sequential source method from 1, 2, 3 and 4 measurements (for increasing values of t) compared to the same measurements obtained from the stochastic approach with four measurements for each value of t on the right-hand side.

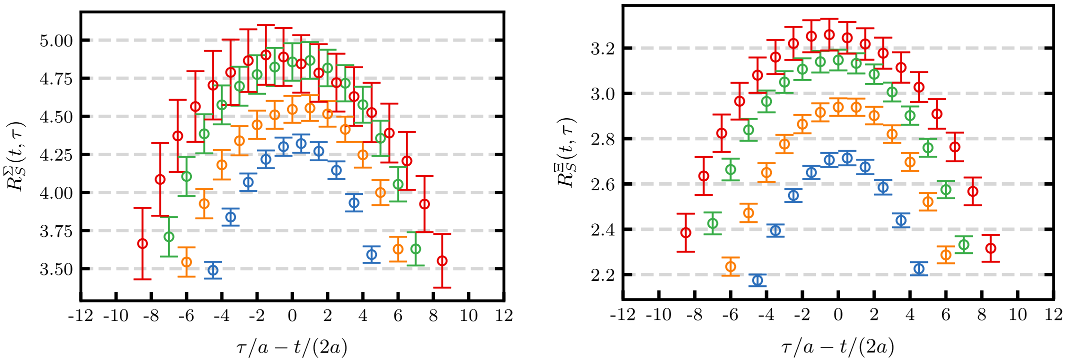

FIG. 37. Unrenormalized ratio of three-point over two-point functions for the Σ (left) and Ξ (right) scalar charge on ensemble N200.

$$N[I] = N_F^I \cdot N_{\mathbf{q}} \cdot N_{\partial_\mu} \cdot N_\tau \cdot N_{\rm src} \cdot N_{\rm sto} \cdot N_c \cdot N_s^2. \qquad \text{(A2)}$$

Here $N_F^{S/I}$ denotes the number of flavor combinations for the spectator and insertion parts (typically 4 and 2, respectively), $N_{\mathbf{p}}$ gives the number of momentum combinations for a maximum momentum $|\mathbf{p}|$ (with $\mathbf{p}$ either being the sink momentum $\mathbf{p}'$ or the momentum transfer $\mathbf{q}$), $N_{\rm src/snk}$ corresponds to the number of source (4) and sink (2) positions, $N_c = 3$ and $N_s = 4$ are the dimensions of color and spin space and N_τ is the number of current insertion time slices, usually the distance between the two sink time slices, see Figs. 6 and 7. N_{∂_μ} refers to the number of derivatives included in the current insertion. We consider all currents including up to one derivative ($N_{\partial_\mu} = 1 + 4$), although only the currents without derivatives are presented in this work. This adds up to a file size of the order of GBs for a single gauge field configuration and disk space usage of the order of TBs for a typical CLS gauge ensemble. Storing the data with all indices open allows for a very flexible analysis. Octet or decuplet baryon three-point functions can be constructed from the spectator and insertion parts for different polarizations, current insertions as well as for a large number of momentum combinations.

2. Treatment of outliers

When analysing the three-point functions on some of the ensembles, we observe a small number of three-point function results that are by many orders of magnitude larger than the rest. These outliers, whose origin currently remains unexplained, would have a significant impact on the analysis, as illustrated in Fig. 38 for ensemble D200 ($M_\pi = 202$ MeV and $a = 0.064$ fm). The three-point function for the scalar charge with source-sink separation $t/a = 16$ for a single source position is displayed. In this case one outlier is identified (according to the criterion given below) and one sees a substantial change in the configuration average and a reduction in the standard deviation if this measurement (on a particular configuration) is excluded. The Mainz group [141] reported similar outliers when determining the nucleon σ terms on a subset of the CLS

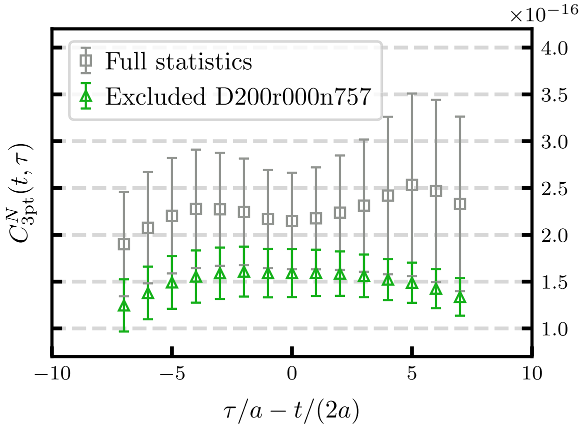

FIG. 38. Nucleon three-point function for the scalar channel with a source-sink separation $t/a = 16$ for a single source position on ensemble D200. The average and standard error is computed including and excluding one particular gauge configuration.

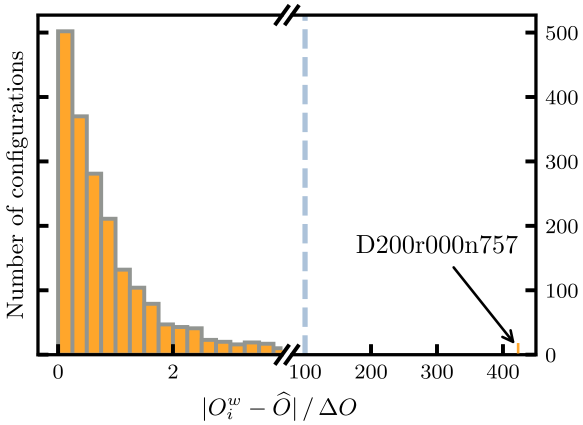

FIG. 39. The numbers of configurations separated by a distance $|O_i^w - \hat{O}|/\Delta O$ from the central value $\hat{O}$ for the three-point function data of Fig. 38 on the insertion time slice $\tau/a = 15$. The blue dashed line indicates the cutoff $K = 100$, which is exceeded by a single measurement. Note the cut and different scales of the ordinate. Due to this representation a few histogram entries are not shown.

gauge ensembles employed here. We remark that such outliers do not seem to occur in the distributions of the two-point function measurements. To overcome this obstacle we constrain the analyzed data and discard "outlier" configurations on which measurements give contributions that are very far away from the expected central value. As discussed in Sec. III A we employ the appropriate reweighting factors where $w_i = w_i^\ell w_i^s$ is the product of the light and strange reweighting factors, determined on each configuration i, see in particular the discussion in Appendix G. 2 of Ref. [17]. In order to have a robust estimate for the variance of the reweighted data

$$O_i^w = \frac{w_i O_i}{w}, \tag{A3}$$

where $w = N_{\mathrm{cnfg}}^{-1} \sum_i w_i$, we determine the lower and upper boundary values O_{low}^w and O_{up}^w of the central 68% interval of this distribution. We then remove configurations i with

$$|O_i^w - \hat{O}| > K\Delta O, \tag{A4}$$

where

$$\hat{O} = \frac{O_{\mathrm{up}}^w + O_{\mathrm{low}}^w}{2}, \qquad \Delta O = \frac{O_{\mathrm{up}}^w - O_{\mathrm{low}}^w}{2}, \tag{A5}$$

setting the cutoff K to a large value ($K = 100$). In Fig. 39 we show the distribution of the measurements for the nucleon three-point function for a scalar current (at a single source position and current insertion time) on the ensemble D200 discussed above (see Fig. 38). The outlier is more than 400 ΔO away from $\hat{O}$. Considering all the three-point function measurements across the different ensembles, we uniformly set the cutoff in Eq. (A4) to $K = 100$ and remove all configurations from the analysis on which at least one measurement satisfies this criterion.

APPENDIX B: ADDITIONAL TABLES

In Table XV we include further details on the gauge ensembles. In Tables XVI–XVIII the results for the unrenormalized charges for the three octet baryons are collected.

TABLE XV. The gauge ensembles utilized in this work: the light and strange hopping parameters κ_ℓ and κ_s, the gradient flow scale parameter t_0/a^2 and the pion (M_π) and kaon masses (M_K) [17].

Ensemble	κ_ℓ	κ_s	t_0/a^2	aM_π	aM_K
A653	0.1365716	0.1365716	2.1729(50)	0.21235(94)	0.21235(94)
A650	0.136600	0.136600	2.2878(72)	0.1833(13)	0.1833(13)
A654	0.136750	0.136216193	2.1950(77)	0.1669(11)	0.22714(91)
H101	0.13675962	0.13675962	2.8545(81)	0.18283(57)	0.18283(57)
U103	0.13675962	0.13675962	2.8815(57)	0.18133(61)	0.18133(61)
H107	0.13694566590798	0.136203165143476	2.7193(76)	0.15913(73)	0.23745(53)
H102r002	0.136865	0.136549339	2.8792(90)	0.15490(92)	0.19193(77)
U102	0.136865	0.136549339	2.8932(63)	0.15444(84)	0.19235(61)
H102r001	0.136865	0.136549339	2.8840(89)	0.15311(98)	0.19089(78)
rqcd021	0.136813	0.136813	3.032(15)	0.14694(88)	0.14694(88)
H105	0.136970	0.13634079	2.8917(65)	0.1213(14)	0.20233(64)
N101	0.136970	0.13634079	2.8948(39)	0.12132(58)	0.20156(30)
H106	0.137015570024	0.136148704478	2.8227(68)	0.1180(21)	0.22471(67)
C102	0.13705084580022	0.13612906255557	2.8682(47)	0.09644(77)	0.21783(36)
C101	0.137030	0.136222041	2.9176(38)	0.09586(64)	0.20561(33)
D101	0.137030	0.136222041	2.910(10)	0.0958(11)	0.20572(45)
S100	0.137030	0.136222041	2.9212(91)	0.0924(31)	0.20551(57)
D150	0.137088	0.13610755	2.9476(30)	0.05497(79)	0.20834(17)
B450	0.136890	0.136890	3.663(11)	0.16095(49)	0.16095(49)
S400	0.136984	0.136702387	3.6919(74)	0.13535(42)	0.17031(38)
B452	0.1370455	0.136378044	3.5286(66)	0.13471(47)	0.20972(34)
rqcd030	0.1369587	0.1369587	3.914(15)	0.12202(68)	0.12202(68)
N451	0.1370616	0.1365480771	3.6822(46)	0.11067(32)	0.17828(20)
N401	0.1370616	0.1365480771	3.6844(52)	0.10984(57)	0.17759(37)
N450	0.1370986	0.136352601	3.5920(42)	0.10965(31)	0.20176(18)
X450	0.136994	0.136994	3.9935(92)	0.10142(62)	0.10142(62)
D451	0.137140	0.136337761	3.6684(36)	0.08370(31)	0.19385(15)
D450	0.137126	0.136420428639937	3.7076(75)	0.08255(41)	0.18354(12)
D452	0.137163675	0.136345904546	3.7251(37)	0.05961(50)	0.18647(13)

(Table continued)

TABLE XV. *(Continued)*

Ensemble	κ_ℓ	κ_s	t_0/a^2	aM_π	aM_K
N202	0.137000	0.137000	5.165(14)	0.13388(35)	0.13388(35)
N204	0.137112	0.136575049	4.9473(79)	0.11423(33)	0.17734(29)
X250	0.137050	0.137050	5.283(28)	0.11319(39)	0.11319(39)
N203	0.137080	0.136840284	5.1465(63)	0.11245(30)	0.14399(24)
S201	0.137140	0.13672086	5.1638(91)	0.09379(47)	0.15220(37)
N201	0.13715968	0.136561319	5.0427(75)	0.09268(31)	0.17040(22)
N200	0.137140	0.13672086	5.1600(71)	0.09236(29)	0.15061(24)
X251	0.137100	0.137100	5.483(26)	0.08678(40)	0.08678(40)
D200	0.137200	0.136601748	5.1793(39)	0.06540(33)	0.15652(15)
D201	0.1372067	0.136546844	5.1378(66)	0.06472(42)	0.16302(18)
E250	0.137232867	0.136536633	5.2027(41)	0.04227(23)	0.159370(61)
N300	0.137000	0.137000	8.576(21)	0.10642(38)	0.10642(38)
N304	0.137079325093654	0.136665430105663	8.322(20)	0.08840(33)	0.13960(31)
N302	0.137064	0.1368721791358	8.539(19)	0.08701(41)	0.11370(36)
J304	0.137130	0.1366569203	8.497(12)	0.06538(18)	0.13181(14)
J303	0.137123	0.1367546608	8.615(14)	0.06481(19)	0.11975(16)
E300	0.137163	0.1366751636177327	8.6241(74)	0.04402(20)	0.12397(15)
J500	0.136852	0.136852	14.013(34)	0.08116(34)	0.08116(34)
J501	0.1369032	0.136749715	13.928(39)	0.06589(26)	0.08798(23)

TABLE XVI. Results for the unrenormalized nucleon charges $g_J^{N,\mathrm{latt}}$ for $J \in \{A, S, T, V\}$. #ES labels the number of excited states used to determine the ground state matrix element, see the discussion in Sec. III D.

#ES	1				2			
Ensemble	$g_A^{N,\mathrm{latt}}$	$g_S^{N,\mathrm{latt}}$	$g_T^{N,\mathrm{latt}}$	$g_V^{N,\mathrm{latt}}$	$g_A^{N,\mathrm{latt}}$	$g_S^{N,\mathrm{latt}}$	$g_T^{N,\mathrm{latt}}$	$g_V^{N,\mathrm{latt}}$
A653	1.563(17)	1.449(60)	1.273(13)	1.4140(24)	1.589(18)	1.43(10)	1.279(13)	1.4136(21)
A650	1.554(13)	1.468(68)	1.236(10)	1.4173(35)	1.581(18)	1.41(13)	1.243(12)	1.4171(32)
A654	1.545(22)	1.62(21)	1.216(30)	1.4353(85)	1.538(33)	1.76(34)	1.211(19)	1.4365(87)
H101	1.5662(88)	1.760(55)	1.221(13)	1.39160(46)	1.584(16)	1.795(88)	1.224(13)	1.39152(46)
U103	1.495(17)	1.61(11)	1.219(23)	1.39001(77)	1.511(26)	1.68(13)	1.227(18)	1.38990(66)
H107	1.630(37)	1.46(13)	1.248(19)	1.40067(98)	1.667(29)	1.34(17)	1.260(20)	1.40051(77)
H102r002	1.596(21)	1.70(15)	1.221(22)	1.3986(11)	1.616(29)	1.84(21)	1.231(21)	1.39817(87)
U102[a]	1.449(41)	1.42(17)	1.180(56)	1.3988(22)	1.448(41)	1.32(24)	1.194(31)	1.3982(11)
H102r001	1.582(15)	1.67(10)	1.230(21)	1.39706(67)	1.598(32)	1.78(19)	1.235(21)	1.39698(62)
rqcd021	1.546(16)	1.67(12)	1.188(22)	1.383(13)	1.567(30)	1.60(23)	1.190(22)	1.383(12)
H105	1.533(29)	1.44(20)	1.194(37)	1.4077(18)	1.524(51)	1.29(44)	1.199(32)	1.4074(15)
N101[a]	1.623(19)	1.662(87)	1.229(16)	1.40416(63)	1.670(32)	1.64(21)	1.236(18)	1.40411(53)
H106	1.589(34)	1.30(27)	1.223(35)	1.4084(20)	1.597(64)	1.20(50)	1.231(37)	1.4081(17)
C102	1.699(36)	1.70(32)	1.184(25)	1.4083(13)	1.755(58)	1.74(54)	1.198(29)	1.4083(12)
C101	1.675(37)	1.67(17)	1.214(17)	1.40908(85)	1.758(44)	1.76(40)	1.232(18)	1.40872(69)
D101[a]	1.647(51)	1.74(34)	1.222(40)	1.4091(18)	1.700(80)	2.09(77)	1.236(36)	1.4088(11)
S100[a]	1.86(98)	1.6(1.2)	1.27(21)	1.4091(49)	1.75(16)	1.6(1.5)	1.257(57)	1.4072(25)
D150[a]	1.49(21)	2.8(2.9)	0.88(23)	1.430(13)	1.39(31)	5.0(4.0)	0.92(14)	1.430(15)
B450	1.549(12)	1.642(72)	1.228(13)	1.3729(31)	1.587(18)	1.61(13)	1.233(14)	1.3724(27)
S400	1.525(13)	1.645(90)	1.191(22)	1.37682(65)	1.523(28)	1.63(17)	1.193(20)	1.37683(59)
B452	1.555(15)	1.49(10)	1.232(17)	1.3781(38)	1.568(30)	1.39(24)	1.235(19)	1.3781(36)
rqcd030	1.510(14)	1.531(92)	1.178(15)	1.3769(33)	1.553(27)	1.47(20)	1.182(16)	1.3769(30)
N451	1.595(14)	1.603(89)	1.212(15)	1.3828(35)	1.636(31)	1.49(21)	1.217(18)	1.3828(30)
N401	1.584(26)	2.00(27)	1.166(37)	1.3836(11)	1.603(51)	2.27(46)	1.180(31)	1.38328(91)
N450	1.598(13)	1.67(11)	1.208(17)	1.3840(29)	1.625(31)	1.58(26)	1.210(19)	1.3838(29)
X450	1.558(23)	1.99(18)	1.166(23)	1.3884(78)	1.606(51)	2.15(37)	1.174(24)	1.3873(69)

(Table continued)

TABLE XVI. *(Continued)*

#ES	1				2			
Ensemble	$g_A^{N,\text{latt}}$	$g_S^{N,\text{latt}}$	$g_T^{N,\text{latt}}$	$g_V^{N,\text{latt}}$	$g_A^{N,\text{latt}}$	$g_S^{N,\text{latt}}$	$g_T^{N,\text{latt}}$	$g_V^{N,\text{latt}}$
D451	1.583(25)	1.42(25)	1.175(36)	1.3807(78)	1.554(80)	0.88(77)	1.176(38)	1.379(10)
D450	1.623(25)	1.46(30)	1.201(22)	1.3761(90)	1.672(66)	1.04(77)	1.207(27)	1.3769(84)
D452[b]	1.54(21)	0.1(4.5)	0.95(19)	1.07(42)	1.53(32)	−1.0(5.1)	1.00(13)	1.13(22)
N202	1.537(12)	1.926(84)	1.170(17)	1.34793(29)	1.556(20)	2.03(11)	1.179(16)	1.34780(28)
N204	1.570(13)	1.694(91)	1.200(14)	1.35344(39)	1.587(25)	1.80(19)	1.205(15)	1.35335(37)
X250	1.5232(98)	1.814(80)	1.163(14)	1.3513(25)	1.546(19)	1.88(15)	1.167(14)	1.3512(23)
N203	1.532(10)	1.748(68)	1.176(16)	1.35169(27)	1.545(26)	1.69(15)	1.176(16)	1.35169(27)
S201[a]	1.436(25)	1.49(21)	1.155(41)	1.35576(78)	1.52(12)	0.82(98)	1.160(41)	1.3555(10)
N201	1.568(18)	1.67(16)	1.158(21)	1.35653(50)	1.594(36)	1.54(35)	1.162(23)	1.35649(49)
N200	1.565(21)	1.47(15)	1.174(19)	1.35533(37)	1.607(40)	1.33(32)	1.179(22)	1.35530(34)
X251	1.532(25)	1.94(16)	1.135(14)	1.3568(56)	1.604(25)	2.18(26)	1.149(14)	1.3558(41)
D200	1.582(24)	1.94(30)	1.136(32)	1.35952(43)	1.617(61)	2.37(72)	1.140(32)	1.35997(77)
D201	1.562(35)	1.60(41)	1.135(48)	1.35922(82)	1.597(91)	1.82(98)	1.141(45)	1.35922(67)
E250[a]	1.66(14)	1.8(1.2)	1.134(77)	1.353(28)	2.00(20)	3.2(3.8)	1.175(55)	1.358(13)
N300	1.479(12)	1.813(95)	1.149(20)	1.31543(19)	1.485(22)	1.83(14)	1.152(19)	1.31540(16)
N304	1.495(23)	1.64(18)	1.137(28)	1.31926(32)	1.501(36)	1.52(31)	1.140(27)	1.31924(31)
N302	1.498(19)	1.82(18)	1.097(29)	1.31893(29)	1.523(35)	1.83(30)	1.103(27)	1.31889(27)
J304	1.529(19)	1.77(22)	1.107(22)	1.32310(36)	1.567(39)	1.67(51)	1.113(23)	1.32305(37)
J303	1.518(17)	1.51(14)	1.096(29)	1.32206(21)	1.526(56)	1.16(53)	1.094(36)	1.32198(25)
E300	1.557(37)	1.67(36)	1.086(25)	1.3135(88)	1.646(61)	1.44(92)	1.100(33)	1.312(11)
J500	1.451(11)	1.858(92)	1.108(18)	1.29090(12)	1.453(18)	1.91(11)	1.114(13)	1.290855(87)
J501	1.484(37)	2.13(30)	1.072(59)	1.29352(16)	1.499(38)	2.10(28)	1.088(29)	1.29349(19)

[a] Ensemble only enters the analysis of the nucleon charges since no data for the hyperon charges are available.

[b] The nucleon three-point functions are computed with the “stochastic” approach. (For all the other ensembles the sequential source method was used.)

TABLE XVII. Results for the unrenormalized hyperon charges $g_J^{\Sigma,\text{latt}}$ for $J \in \{A, S, T, V\}$. #ES labels the number of excited states used to determine the ground state matrix element, see the discussion in Sec. III D. The three-point functions are computed employing the “stochastic” approach.

#ES	1				2			
Ensemble	$g_A^{\Sigma,\text{latt}}$	$g_S^{\Sigma,\text{latt}}$	$g_T^{\Sigma,\text{latt}}$	$g_V^{\Sigma,\text{latt}}$	$g_A^{\Sigma,\text{latt}}$	$g_S^{\Sigma,\text{latt}}$	$g_T^{\Sigma,\text{latt}}$	$g_V^{\Sigma,\text{latt}}$
A653	1.180(10)	4.40(14)	1.018(14)	2.8354(32)	1.189(16)	4.45(14)	1.023(12)	2.8347(27)
A650	1.1764(90)	4.46(12)	0.9968(95)	2.8381(39)	1.190(16)	4.49(15)	1.000(10)	2.8380(37)
A654	1.173(12)	4.01(16)	1.028(13)	2.852(12)	1.204(37)	4.11(30)	1.028(16)	2.850(14)
H101	1.1877(81)	5.03(12)	0.982(10)	2.78711(66)	1.198(13)	5.12(14)	0.987(10)	2.78686(65)
U103	1.137(13)	4.69(18)	0.983(16)	2.78535(89)	1.147(21)	4.75(18)	0.989(16)	2.78507(80)
H107	1.207(18)	4.25(19)	1.030(12)	2.823(15)	1.232(28)	4.35(27)	1.036(13)	2.820(11)
H102r002	1.177(13)	4.67(17)	0.988(13)	2.807(14)	1.199(25)	4.77(22)	0.992(14)	2.805(12)
H102r001	1.157(14)	4.73(19)	0.973(16)	2.788(11)	1.146(27)	4.79(28)	0.978(17)	2.788(11)
rqcd021	1.149(15)	5.27(24)	0.958(19)	2.790(14)	1.145(27)	5.35(33)	0.962(19)	2.790(13)
H105	1.147(22)	4.83(44)	0.958(23)	2.812(20)	1.162(40)	5.25(55)	0.969(21)	2.809(16)
H106	1.139(15)	4.24(20)	0.968(16)	2.796(15)	1.149(38)	4.27(48)	0.970(19)	2.796(15)
C102	1.140(19)	4.32(29)	0.950(27)	2.791(23)	1.133(45)	3.94(76)	0.952(22)	2.792(18)
C101	1.174(21)	4.58(43)	0.957(22)	2.837(21)	1.240(51)	4.80(94)	0.963(21)	2.834(17)
B450	1.1743(76)	4.80(14)	0.992(11)	2.7464(30)	1.195(15)	4.90(18)	0.997(11)	2.7460(28)
S400	1.159(16)	5.25(29)	0.945(17)	2.751(13)	1.180(23)	5.43(27)	0.962(16)	2.752(11)
B452	1.147(13)	4.33(18)	0.990(16)	2.764(13)	1.163(28)	4.45(33)	0.994(16)	2.763(12)
rqcd030	1.140(12)	5.20(22)	0.944(16)	2.7576(35)	1.157(22)	5.41(33)	0.950(15)	2.7573(33)
N451	1.168(15)	4.90(34)	0.976(14)	2.795(18)	1.193(30)	5.43(38)	0.988(11)	2.789(12)
N401	1.130(52)	5.22(68)	0.933(50)	2.781(42)	1.100(67)	5.23(82)	0.949(33)	2.776(31)

(Table continued)

TABLE XVII. *(Continued)*

#ES Ensemble	1				2			
	$g_A^{\Sigma,\mathrm{latt}}$	$g_S^{\Sigma,\mathrm{latt}}$	$g_T^{\Sigma,\mathrm{latt}}$	$g_V^{\Sigma,\mathrm{latt}}$	$g_A^{\Sigma,\mathrm{latt}}$	$g_S^{\Sigma,\mathrm{latt}}$	$g_T^{\Sigma,\mathrm{latt}}$	$g_V^{\Sigma,\mathrm{latt}}$
N450	1.148(18)	4.11(17)	0.994(20)	2.738(24)	1.154(43)	3.54(65)	0.992(17)	2.737(21)
X450	1.168(23)	6.05(38)	0.924(25)	2.7700(84)	1.195(49)	6.38(58)	0.933(25)	2.7690(79)
D451	1.143(53)	4.79(95)	0.955(38)	2.67(10)	1.18(15)	3.8(3.0)	0.948(45)	2.624(56)
D450	1.129(63)	4.9(1.1)	0.938(52)	2.721(77)	1.09(11)	3.9(2.1)	0.944(42)	2.730(48)
D452	1.115(52)	4.8(1.1)	0.923(52)	2.789(28)	1.07(14)	5.3(2.6)	0.935(44)	2.787(29)
N202	1.166(10)	5.68(20)	0.939(12)	2.69777(45)	1.182(16)	5.85(15)	0.955(13)	2.69721(41)
N204	1.1465(91)	4.30(12)	0.980(11)	2.686(11)	1.160(26)	4.22(30)	0.979(12)	2.686(12)
X250	1.1549(88)	5.85(20)	0.928(12)	2.7051(32)	1.167(16)	6.12(21)	0.940(12)	2.7046(27)
N203	1.156(12)	5.60(26)	0.941(10)	2.7246(96)	1.182(19)	6.05(22)	0.9623(87)	2.7184(69)
N201	1.150(17)	5.22(43)	0.953(18)	2.737(17)	1.163(42)	5.70(53)	0.965(17)	2.733(14)
N200	1.119(13)	5.03(21)	0.947(13)	2.721(11)	1.116(26)	5.37(36)	0.954(12)	2.720(10)
X251	1.145(16)	6.59(33)	0.903(13)	2.7165(69)	1.195(24)	7.06(37)	0.916(14)	2.7145(55)
D200	1.082(48)	6.4(1.4)	0.841(59)	2.774(26)	1.058(82)	7.7(1.8)	0.867(38)	2.777(29)
D201	1.125(34)	5.7(1.3)	0.924(37)	2.730(31)	1.133(62)	6.8(1.2)	0.944(24)	2.726(19)
N300	1.121(12)	5.52(19)	0.918(17)	2.63208(25)	1.126(19)	5.59(18)	0.925(16)	2.63197(23)
N304	1.106(18)	4.84(31)	0.925(21)	2.642(17)	1.130(30)	4.87(45)	0.928(20)	2.641(15)
N302	1.086(26)	5.41(35)	0.864(34)	2.668(25)	1.118(42)	5.38(49)	0.868(26)	2.666(21)
J304	1.091(29)	5.95(65)	0.864(30)	2.646(25)	1.149(54)	6.61(74)	0.879(23)	2.645(18)
J303	1.100(19)	5.23(59)	0.914(22)	2.671(31)	1.198(61)	5.88(96)	0.927(17)	2.669(26)
E300	1.047(93)	7.9(3.8)	0.853(57)	2.728(87)	1.04(12)	9.1(3.1)	0.884(41)	2.705(55)
J500	1.100(10)	5.78(20)	0.887(13)	2.58250(15)	1.106(15)	5.82(16)	0.894(11)	2.58241(12)
J501	1.053(35)	6.01(86)	0.857(46)	2.629(22)	1.038(54)	6.26(66)	0.878(22)	2.628(19)

TABLE XVIII. Results for the unrenormalized hyperon charges $g_J^{\Xi,\mathrm{latt}}$ for $J \in \{A, S, T, V\}$. #ES labels the number of excited states used to determine the ground state matrix element, see the discussion in Sec. III D. The three-point functions are computed employing the “stochastic” approach.

#ES Ensemble	1				2			
	$g_A^{\Xi,\mathrm{latt}}$	$g_S^{\Xi,\mathrm{latt}}$	$g_T^{\Xi,\mathrm{latt}}$	$g_V^{\Xi,\mathrm{latt}}$	$g_A^{\Xi,\mathrm{latt}}$	$g_S^{\Xi,\mathrm{latt}}$	$g_T^{\Xi,\mathrm{latt}}$	$g_V^{\Xi,\mathrm{latt}}$
A653	−0.399(16)	3.13(18)	−0.2495(54)	1.4229(30)	−0.401(11)	3.019(89)	−0.2534(38)	1.4206(21)
A650	−0.3849(96)	3.13(11)	−0.2375(43)	1.4213(28)	−0.3905(95)	3.109(92)	−0.2423(43)	1.4211(20)
A654	−0.3528(58)	2.65(12)	−0.2407(47)	1.4344(67)	−0.354(12)	2.63(17)	−0.2408(59)	1.4349(67)
H101	−0.3810(53)	3.331(91)	−0.2342(41)	1.39556(41)	−0.3854(82)	3.349(93)	−0.2371(48)	1.39528(40)
U103	−0.3580(67)	3.09(11)	−0.2389(48)	1.39547(47)	−0.362(12)	3.05(14)	−0.2380(43)	1.39563(47)
H107	−0.3602(71)	2.89(16)	−0.2413(41)	1.4165(82)	−0.3653(77)	2.93(12)	−0.2453(38)	1.4126(64)
H102r002	−0.3707(54)	3.122(91)	−0.2336(34)	1.4045(52)	−0.3708(92)	3.16(12)	−0.2357(42)	1.4038(48)
H102r001	−0.3671(52)	3.12(10)	−0.2362(35)	1.3987(55)	−0.3683(99)	3.16(14)	−0.2383(45)	1.3987(52)
rqcd021	−0.418(17)	3.93(22)	−0.2211(82)	1.415(15)	−0.425(16)	3.81(21)	−0.2275(71)	1.409(10)
H105	−0.370(11)	3.25(26)	−0.2214(68)	1.4050(86)	−0.372(11)	3.24(22)	−0.2261(72)	1.4047(73)
H106	−0.3448(45)	2.605(83)	−0.2347(27)	1.4052(42)	−0.3553(84)	2.56(22)	−0.2359(39)	1.4049(46)
C102	−0.3431(42)	2.672(96)	−0.2296(41)	1.4007(52)	−0.341(13)	2.52(28)	−0.2286(50)	1.4000(57)
C101	−0.373(23)	3.15(38)	−0.2398(58)	1.423(13)	−0.387(14)	3.19(35)	−0.2436(33)	1.4177(99)
B450	−0.3822(73)	3.321(81)	−0.2322(46)	1.3737(22)	−0.3914(98)	3.289(96)	−0.2352(56)	1.3737(19)
S400	−0.3560(57)	3.20(12)	−0.2332(41)	1.3774(56)	−0.3577(91)	3.28(13)	−0.2373(50)	1.3778(51)
B452	−0.3484(52)	2.873(96)	−0.2309(35)	1.3669(53)	−0.3523(85)	2.90(13)	−0.2333(45)	1.3680(57)
rqcd030	−0.384(11)	3.93(22)	−0.2249(65)	1.3819(34)	−0.394(14)	3.96(25)	−0.2313(67)	1.3807(28)
N451	−0.3693(57)	3.55(15)	−0.2183(42)	1.3969(68)	−0.3720(94)	3.74(17)	−0.2248(46)	1.3948(55)
N401	−0.372(13)	3.17(18)	−0.2296(58)	1.389(13)	−0.389(16)	3.07(32)	−0.2325(68)	1.388(12)
N450	−0.3489(63)	2.92(14)	−0.2294(42)	1.3764(77)	−0.351(14)	2.87(27)	−0.2297(59)	1.3759(78)
X450	−0.403(18)	4.29(31)	−0.2314(88)	1.3809(53)	−0.414(23)	4.39(34)	−0.2369(74)	1.3810(45)
D451	−0.308(19)	2.70(25)	−0.226(19)	1.361(35)	−0.286(36)	1.87(98)	−0.225(13)	1.351(24)

(Table continued)

TABLE XVIII. *(Continued)*

#ES	1				2			
Ensemble	$g_A^{\Xi,\mathrm{latt}}$	$g_S^{\Xi,\mathrm{latt}}$	$g_T^{\Xi,\mathrm{latt}}$	$g_V^{\Xi,\mathrm{latt}}$	$g_A^{\Xi,\mathrm{latt}}$	$g_S^{\Xi,\mathrm{latt}}$	$g_T^{\Xi,\mathrm{latt}}$	$g_V^{\Xi,\mathrm{latt}}$
D450	−0.365(21)	3.79(88)	−0.2334(98)	1.391(18)	−0.372(29)	4.27(62)	−0.2377(53)	1.391(11)
D452	−0.320(13)	3.75(66)	−0.2213(80)	1.399(13)	−0.292(33)	4.41(95)	−0.2268(84)	1.397(11)
N202	−0.3758(48)	3.78(10)	−0.2202(41)	1.34982(24)	−0.3759(89)	3.817(99)	−0.2244(50)	1.34959(23)
N204	−0.3365(44)	2.916(92)	−0.2262(35)	1.3484(47)	−0.326(11)	2.91(15)	−0.2252(46)	1.3479(51)
X250	−0.3753(54)	4.18(14)	−0.2195(43)	1.3541(24)	−0.3782(80)	4.26(14)	−0.2257(46)	1.3536(19)
N203	−0.3612(42)	3.652(95)	−0.2178(30)	1.3549(53)	−0.3649(75)	3.74(12)	−0.2220(36)	1.3542(47)
N201	−0.350(11)	3.44(32)	−0.2222(49)	1.377(12)	−0.355(10)	3.56(20)	−0.2285(47)	1.3714(79)
N200	−0.3515(42)	3.58(13)	−0.2147(38)	1.3665(49)	−0.3542(78)	3.73(16)	−0.2184(42)	1.3653(43)
X251	−0.3942(89)	4.68(18)	−0.2226(60)	1.3600(46)	−0.409(11)	4.84(21)	−0.2295(43)	1.3576(40)
D200	−0.347(16)	4.2(1.0)	−0.2127(76)	1.3738(89)	−0.350(15)	4.69(49)	−0.2237(51)	1.3707(70)
D201	−0.3393(78)	3.38(26)	−0.2082(60)	1.3647(83)	−0.344(17)	3.47(51)	−0.2100(74)	1.3645(84)
N300	−0.3596(58)	3.74(10)	−0.2246(45)	1.31662(16)	−0.359(10)	3.78(11)	−0.2279(49)	1.31649(12)
N304	−0.3307(51)	3.12(11)	−0.2196(43)	1.3182(66)	−0.325(10)	3.09(17)	−0.2169(42)	1.3175(70)
N302	−0.361(11)	3.77(19)	−0.2136(60)	1.341(11)	−0.373(15)	3.72(22)	−0.2170(66)	1.3383(89)
J304	−0.3366(73)	3.45(22)	−0.2090(50)	1.3286(83)	−0.346(11)	3.63(28)	−0.2143(58)	1.3277(67)
J303	−0.3416(75)	3.66(23)	−0.2133(48)	1.3306(94)	−0.358(15)	3.88(34)	−0.2208(59)	1.3298(81)
E300	−0.334(17)	3.75(49)	−0.194(13)	1.342(14)	−0.340(31)	3.5(1.0)	−0.195(14)	1.344(17)
J500	−0.3508(46)	3.89(11)	−0.2174(36)	1.291575(73)	−0.3454(91)	3.93(11)	−0.2198(38)	1.291515(71)
J501	−0.353(10)	4.14(25)	−0.2055(62)	1.314(11)	−0.356(13)	4.17(21)	−0.2071(55)	1.3135(98)

APPENDIX C: ADDITIONAL FIGURES

We provide additional figures (Figs. 40–47).

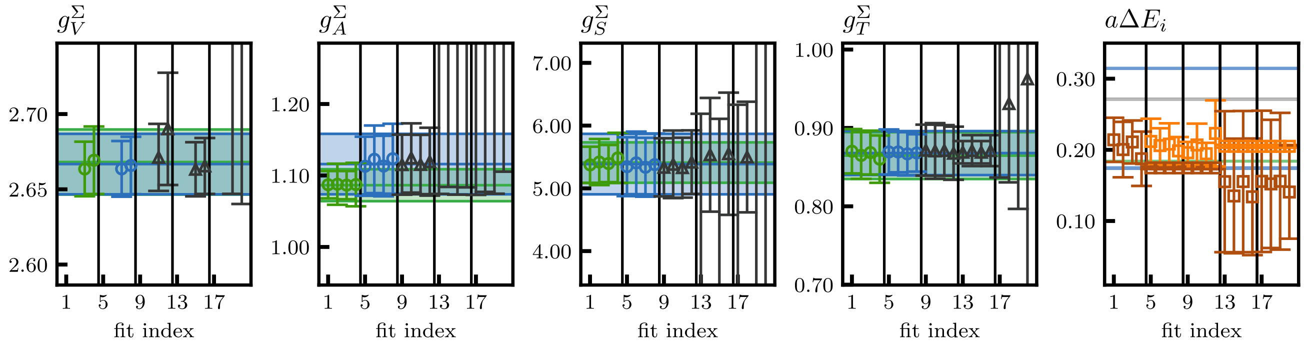

FIG. 40. The same as Fig. 10 for the sigma baryon.

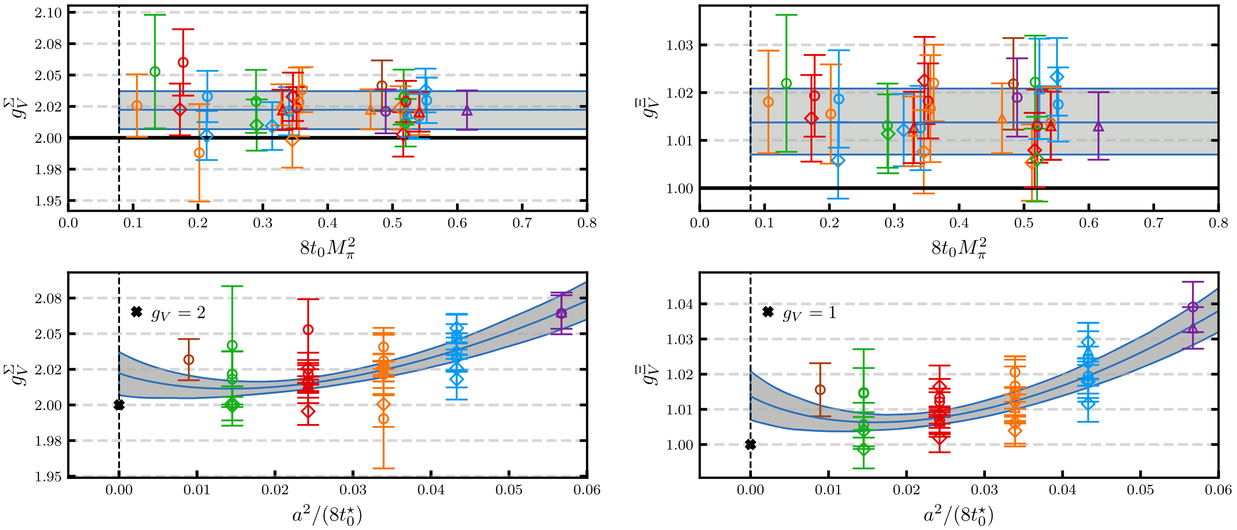

FIG. 41. The same as Fig. 13 for the isovector vector charges g_V^B of the sigma baryon (left) and the cascade baryon (right). For better visibility, the data points for ensemble D451, which have large errors (see Tables XVII and XVIII), are not displayed. See Tables XVII and XVIII for the set of ensembles used.

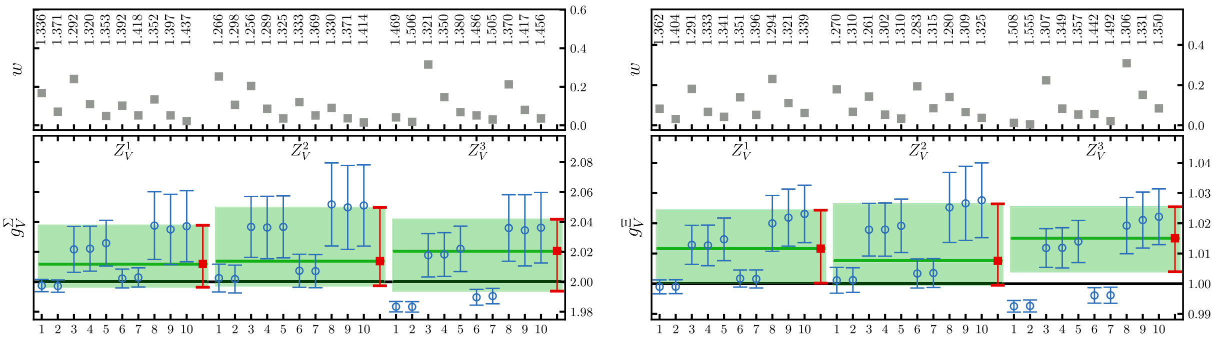

FIG. 42. The same as Fig. 15 for the vector charge g_V^B of the sigma (right) and cascade (left) baryon.

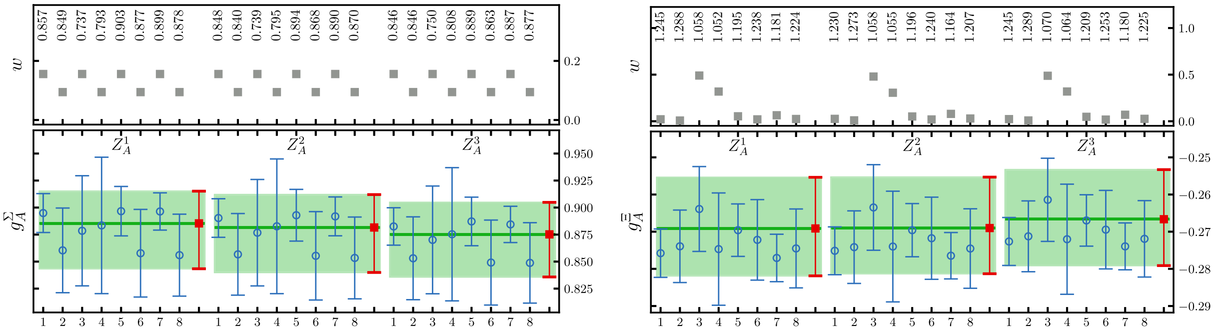

FIG. 43. The same as Fig. 19 for the axial charge g_A^B of the sigma (right) and cascade (left) baryon.

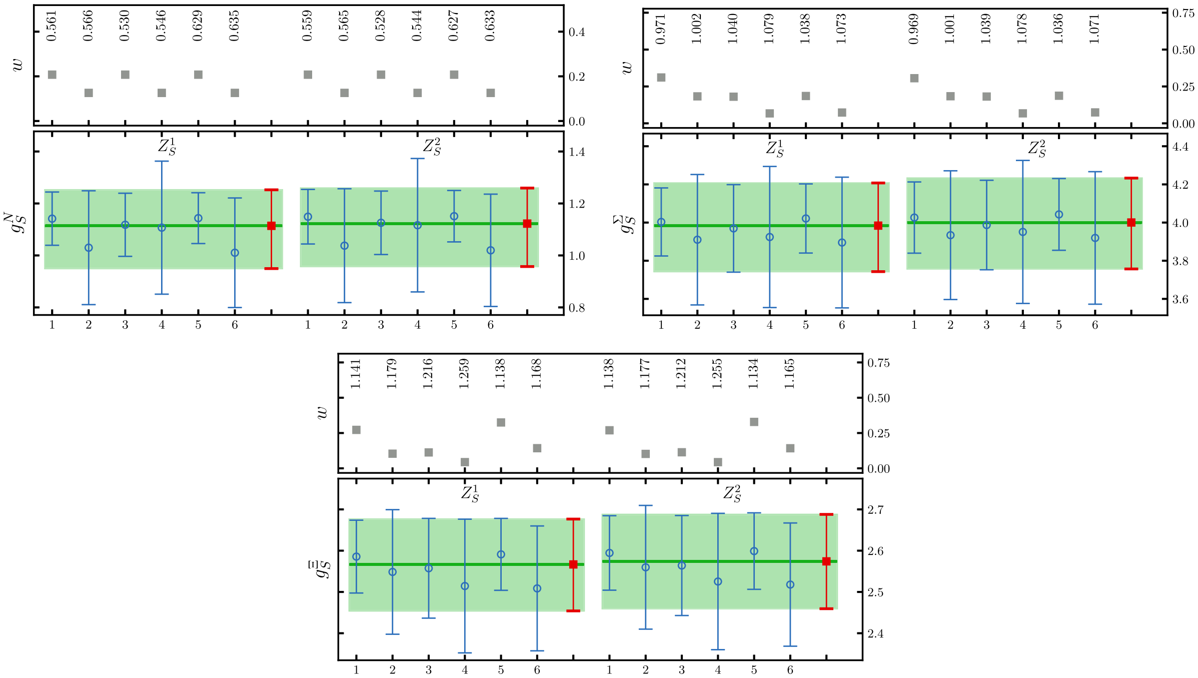

FIG. 44. The same as Fig. 19 for the scalar charge g_S^B of the nucleon (top, left), sigma (top, right) and cascade (bottom) baryons. The six fits correspond to two fit variations, see the text, applied to three datasets, $\mathrm{DS}(M_\pi^{<400\ \mathrm{MeV}})$, $\mathrm{DS}(M_\pi^{<400\ \mathrm{MeV}}, a^{<0.1\ \mathrm{fm}})$ and $\mathrm{DS}(M_\pi^{<400\ \mathrm{MeV}}, LM_\pi^{>4})$. The data are extracted using two excited states in the fitting analysis, see Sec. III D. Only two different sets of renormalization factors are used.

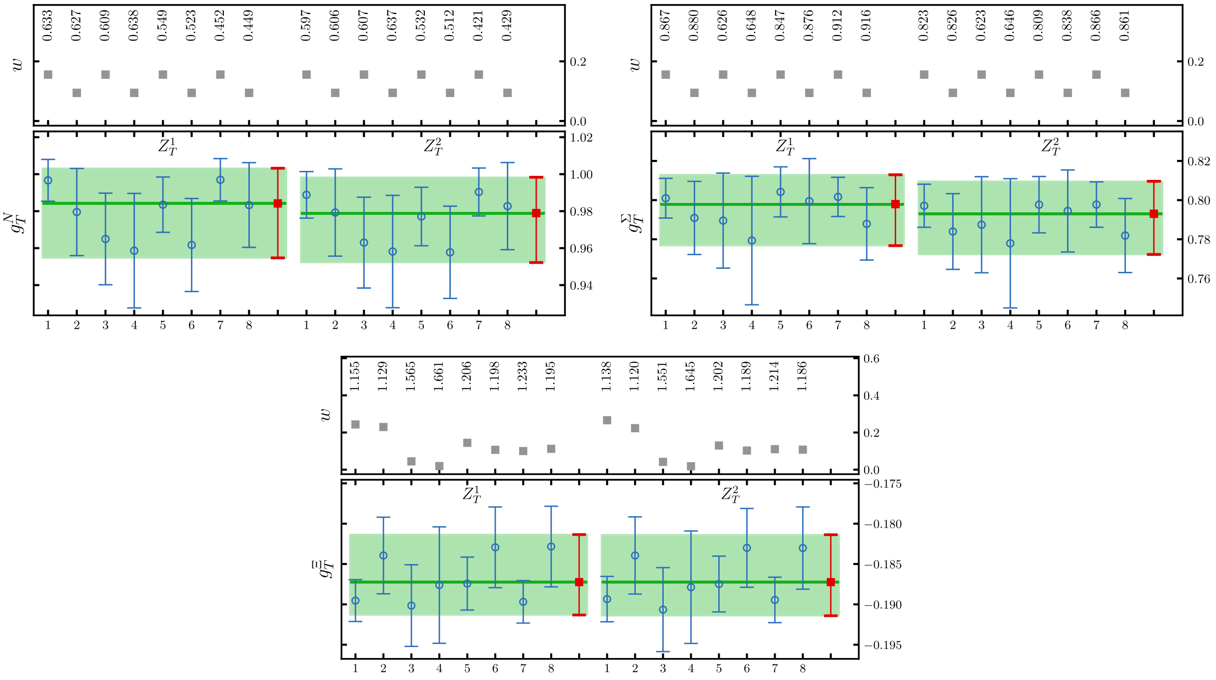

FIG. 45. The same as Fig. 19 for the tensor charge g_T^B for the nucleon (top, left), sigma (top, right) and cascade (bottom) baryons. The data are extracted using two excited states in the fitting analysis, see Sec. III D. Only two different sets of renormalization factors are used.

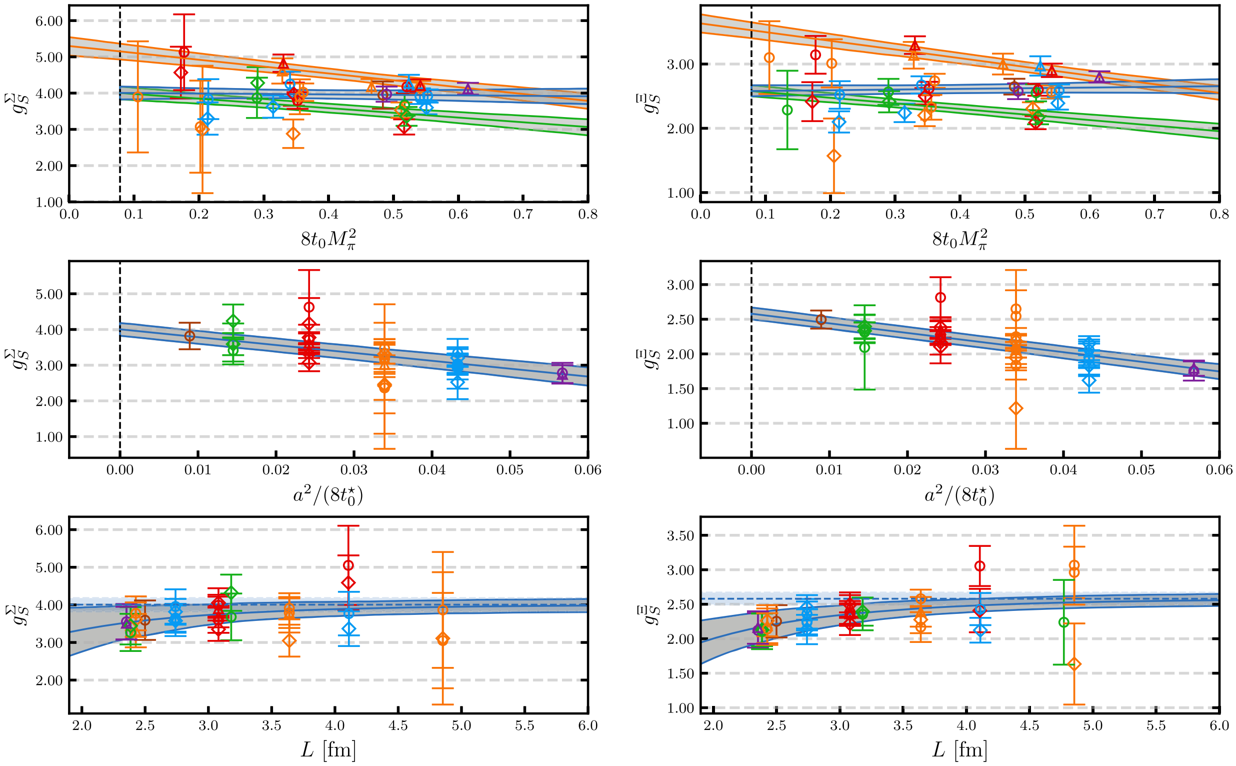

FIG. 46. The same as Fig. 21 for the isovector scalar charges g_S^B of the sigma baryon (left) and the cascade baryon (right). For better visibility, the data point for ensemble E300, which has a relatively large error (see Table XVII), is not displayed for the sigma baryon. See Tables XVII and XVIII for the set of ensembles used.

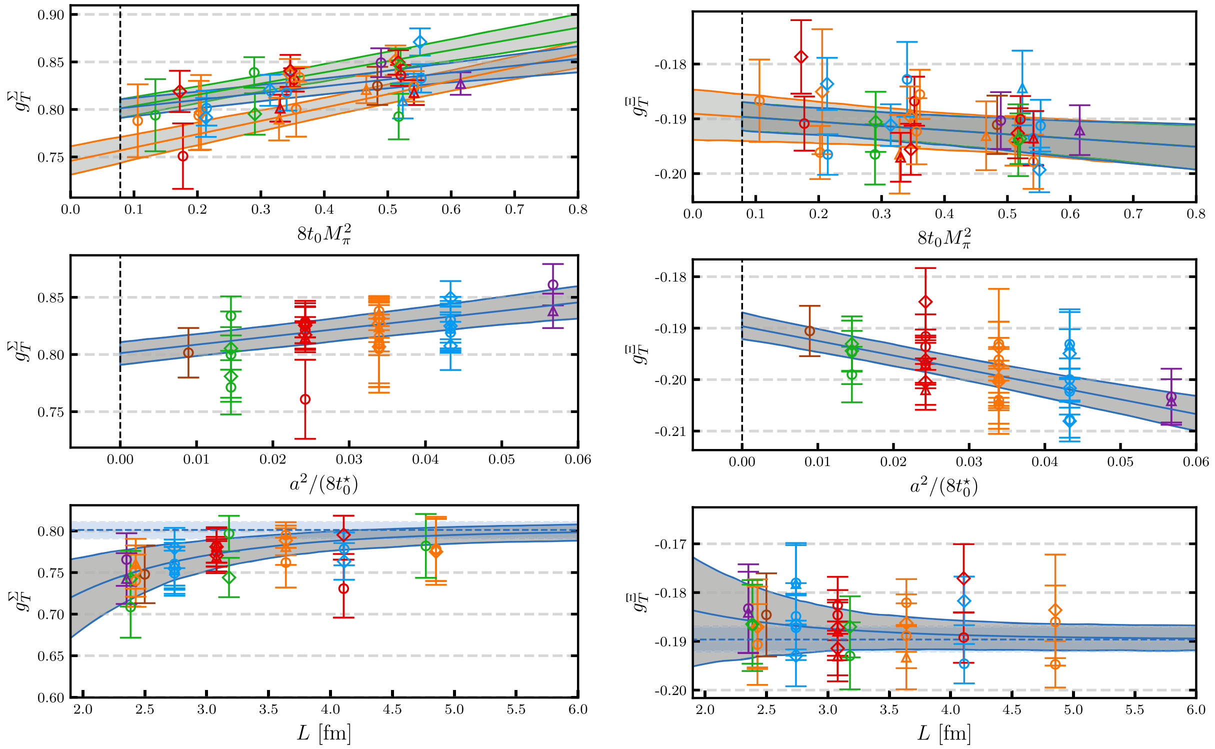

FIG. 47. The same as Fig. 23 for the isovector tensor charges g_T^B of the sigma baryon (left) and the cascade baryon (right). For better visibility, the data point for ensemble E300, which has a relatively large error (see Table XVIII), is not displayed for the cascade baryon. See Tables XVII and XVIII for the set of ensembles used.

[1] X.-D. Ji, Gauge-Invariant Decomposition of Nucleon Spin, Phys. Rev. Lett. **78**, 610 (1997).

[2] R. L. Jaffe and A. Manohar, The g_1 problem: Fact and fantasy on the spin of the proton, Nucl. Phys. **B337**, 509 (1990).

[3] G. S. Bali *et al.* (QCDSF Collaboration), Strangeness Contribution to the Proton Spin from Lattice QCD, Phys. Rev. Lett. **108**, 222001 (2012).

[4] M. Engelhardt, Strange quark contributions to nucleon mass and spin from lattice QCD, Phys. Rev. D **86**, 114510 (2012).

[5] M. Gong, Y.-B. Yang, J. Liang, A. Alexandru, T. Draper, and K.-F. Liu (χQCD Collaboration), Strange and charm quark spins from the anomalous Ward identity, Phys. Rev. D **95**, 114509 (2017).

[6] C. Alexandrou, M. Constantinou, K. Hadjiyiannakou, K. Jansen, C. Kallidonis, G. Koutsou, A. Vaquero Avilés-Casco, and C. Wiese (ETM Collaboration), Nucleon Spin and Momentum Decomposition Using Lattice QCD Simulations, Phys. Rev. Lett. **119**, 142002 (2017).

[7] J. Green, N. Hasan, S. Meinel, M. Engelhardt, S. Krieg, J. Laeuchli, J. Negele, K. Orginos, A. Pochinsky, and S. Syritsyn, Up, down, and strange nucleon axial form factors from lattice QCD, Phys. Rev. D **95**, 114502 (2017).

[8] S. Bürger, T. Wurm, M. Löffler, M. Göckeler, G. Bali, S. Collins, A. Schäfer, and A. Sternbeck (RQCD Collaboration), Lattice results for the longitudinal spin structure and color forces on quarks in a nucleon, Phys. Rev. D **105**, 054504 (2022).

[9] D. de Florian, R. Sassot, M. Stratmann, and W. Vogelsang, Global Analysis of Helicity Parton Densities and Their Uncertainties, Phys. Rev. Lett. **101**, 072001 (2008).

[10] J. Blümlein and H. Böttcher, QCD analysis of polarized deep inelastic scattering data, Nucl. Phys. **B841**, 205 (2010).

[11] E. R. Nocera, R. D. Ball, S. Forte, G. Ridolfi, and J. Rojo (NNPDF Collaboration), A first unbiased global determination of polarized PDFs and their uncertainties, Nucl. Phys. **B887**, 276 (2014).

[12] N. Sato, W. Melnitchouk, S. E. Kuhn, J. J. Ethier, and A. Accardi (JAM Collaboration), Iterative Monte Carlo analysis of spin-dependent parton distributions, Phys. Rev. D **93**, 074005 (2016).

[13] J. J. Ethier, N. Sato, and W. Melnitchouk (JAM Collaboration), First Simultaneous Extraction of Spin-Dependent Parton Distributions and Fragmentation Functions from a Global QCD Analysis, Phys. Rev. Lett. **119**, 132001 (2017).

[14] H.-W. Lin, W. Melnitchouk, A. Prokudin, N. Sato, and H. Shows (JAM Collaboration), First Monte Carlo Global Analysis of Nucleon Transversity with Lattice QCD Constraints, Phys. Rev. Lett. **120**, 152502 (2018).

[15] L. Gamberg, M. Malda, J. A. Miller, D. Pitonyak, A. Prokudin, and N. Sato (JAM Collaboration), Updated QCD global analysis of single transverse-spin asymmetries: Extracting $\tilde{H}$, and the role of the Soffer bound and lattice QCD, Phys. Rev. D **106**, 034014 (2022).

[16] T. Bhattacharya, V. Cirigliano, S. D. Cohen, A. Filipuzzi, M. Gonzalez-Alonso, M. L. Graesser, R. Gupta, and H.-W. Lin, Probing novel scalar and tensor interactions from (ultra)cold neutrons to the LHC, Phys. Rev. D **85**, 054512 (2012).

[17] G. S. Bali, S. Collins, P. Georg, D. Jenkins, P. Korcyl, A. Schäfer, E. E. Scholz, J. Simeth, W. Söldner, and S. Weishäupl (RQCD Collaboration), Scale setting and the light baryon spectrum in $N_f = 2 + 1$ QCD with Wilson fermions, J. High Energy Phys. 05 (2023) 035.

[18] H. Leutwyler, Theoretical aspects of chiral dynamics, Proc. Sci. CD15 (**2015**) 022 [arXiv:1510.07511].

[19] F. Fucito, G. Parisi, and S. Petrarca, First evaluation of g_A/g_V in lattice QCD in the quenched approximation, Phys. Lett. **115B**, 148 (1982).

[20] S. Güsken, U. Löw, K.-H. Mütter, R. Sommer, A. Patel, and K. Schilling, Nonsinglet axial vector couplings of the baryon octet in lattice QCD, Phys. Lett. B **227**, 266 (1989).

[21] R. M. Woloshyn and K.-F. Liu, A study of the nucleon axial current coupling in quenched lattice QCD, Nucl. Phys. **B311**, 527 (1989).

[22] H.-W. Lin and K. Orginos, First calculation of hyperon axial couplings from lattice QCD, Phys. Rev. D **79**, 034507 (2009).

[23] G. Erkol, M. Oka, and T. T. Takahashi, Axial charges of octet baryons in two-flavor lattice QCD, Phys. Lett. B **686**, 36 (2010).

[24] C. Alexandrou, K. Hadjiyiannakou, and C. Kallidonis (ETM Collaboration), Axial charges of hyperons and charmed baryons using $N_f = 2 + 1 + 1$ twisted mass fermions, Phys. Rev. D **94**, 034502 (2016).

[25] A. Savanur and H.-W. Lin, Lattice-QCD determination of the hyperon axial couplings in the continuum limit, Phys. Rev. D **102**, 014501 (2020).

[26] R. E. Smail *et al.* (QCDSF-UKQCD-CSSM Collaboration), Constraining beyond the Standard Model nucleon isovector charges, arXiv:2304.02866.

[27] B. Borasoy and U.-G. Meissner, Chiral expansion of baryon masses and σ-terms, Ann. Phys. (N.Y.) **254**, 192 (1997).

[28] A. N. Cooke, R. Horsley, Y. Nakamura, D. Pleiter, P. E. L. Rakow, G. Schierholz, and J. M. Zanotti, The effects of flavor symmetry breaking on hadron matrix elements, Proc. Sci. LATTICE2012 (**2012**) 116 [arXiv:1212.2564].

[29] J. M. Bickerton, R. Horsley, Y. Nakamura, H. Perlt, D. Pleiter, P. E. L. Rakow, G. Schierholz, H. Stüben, R. D. Young, and J. M. Zanotti (QCDSF-UKQCD-CSSM Collaboration), Patterns of flavor symmetry breaking in hadron matrix elements involving u, d, and s quarks, Phys. Rev. D **100**, 114516 (2019).

[30] E. E. Jenkins and A. V. Manohar, Chiral corrections to the baryon axial currents, Phys. Lett. B **259**, 353 (1991).

[31] R. F. Dashen and A. V. Manohar, $1/N_c$ corrections to the baryon axial currents in QCD, Phys. Lett. B **315**, 438 (1993).

[32] M. Bruno *et al.* (CLS Effort Collaboration), Simulation of QCD with $N_f = 2 + 1$ flavors of nonperturbatively improved Wilson fermions, J. High Energy Phys. 02 (2015) 043.

[33] M. Lüscher and S. Schaefer, Lattice QCD without topology barriers, J. High Energy Phys. 07 (2011) 036.

[34] S. Schaefer, R. Sommer, and F. Virotta (ALPHA Collaboration), Critical slowing down and error analysis in lattice QCD simulations, Nucl. Phys. **B845**, 93 (2011).

[35] M. Lüscher and S. Schaefer, Lattice QCD with open boundary conditions and twisted-mass reweighting, Comput. Phys. Commun. **184**, 519 (2013).

[36] M. A. Clark and A. D. Kennedy, Accelerating Dynamical Fermion Computations Using the Rational Hybrid Monte Carlo (RHMC) Algorithm with Multiple Pseudofermion Fields, Phys. Rev. Lett. **98**, 051601 (2007).

[37] D. Mohler and S. Schaefer, Remarks on strange-quark simulations with Wilson fermions, Phys. Rev. D **102**, 074506 (2020).

[38] G. S. Bali, E. E. Scholz, J. Simeth, and W. Söldner (RQCD Collaboration), Lattice simulations with $N_f = 2 + 1$ improved Wilson fermions at a fixed strange quark mass, Phys. Rev. D **94**, 074501 (2016).

[39] Y. Nakamura and H. Stüben, BQCD—Berlin quantum chromodynamics program, Proc. Sci. LATTICE2010 (**2010**) 040 [arXiv:1011.0199].

[40] M. Falcioni, M. L. Paciello, G. Parisi, and B. Taglienti (APE Collaboration), Again on SU(3) glueball mass, Nucl. Phys. **B251**, 624 (1985).

[41] L. Maiani, G. Martinelli, M. L. Paciello, and B. Taglienti, Scalar densities and baryon mass differences in lattice QCD with Wilson fermions, Nucl. Phys. **B293**, 420 (1987).

[42] J. D. Bratt *et al.* (LHP Collaboration), Nucleon structure from mixed action calculations using $2 + 1$ flavors of asqtad sea and domain wall valence fermions, Phys. Rev. D **82**, 094502 (2010).

[43] G. S. Bali, L. Barca, S. Collins, M. Gruber, M. Löffler, A. Schäfer, W. Söldner, P. Wein, S. Weishäupl, and T. Wurm (RQCD Collaboration), Nucleon axial structure from lattice QCD, J. High Energy Phys. 05 (2020) 126.

[44] R. Evans, G. Bali, and S. Collins, Improved semileptonic form factor calculations in lattice QCD, Phys. Rev. D **82**, 094501 (2010).

[45] G. S. Bali, S. Collins, B. Gläßle, M. Göckeler, J. Najjar, R. Rödl, A. Schäfer, A. Sternbeck, and W. Söldner, Nucleon structure from stochastic estimators, Proc. Sci. LATTICE2013 (**2014**) 271 [arXiv:1311.1718].

[46] G. S. Bali, S. Collins, P. Korcyl, R. Rödl, S. Weishäupl, and T. Wurm, Hyperon couplings from $N_f = 2 + 1$ lattice QCD, Proc. Sci. LATTICE2019 (**2019**) 099 [arXiv:1907.13454].

[47] G. S. Bali, S. Collins, B. Gläßle, S. Heybrock, P. Korcyl, M. Löffler, R. Rödl, and A. Schäfer, Baryonic and mesonic 3-point functions with open spin indices, EPJ Web Conf. **175**, 06014 (2018).

[48] M. Löffler, P. Wein, T. Wurm, S. Weishäupl, D. Jenkins, R. Rödl, A. Schäfer, and L. Walter (RQCD Collaboration), Mellin moments of spin dependent and independent PDFs of the pion and rho meson, Phys. Rev. D **105**, 014505 (2022).

[49] C. Alexandrou, S. Dinter, V. Drach, K. Jansen, K. Hadjiyiannakou, and D. B. Renner (ETM Collaboration), A stochastic method for computing hadronic matrix elements, Eur. Phys. J. C **74**, 2692 (2014).

[50] Y.-B. Yang, A. Alexandru, T. Draper, M. Gong, and K.-F. Liu (χQCD Collaboration), Stochastic method with low mode substitution for nucleon isovector matrix elements, Phys. Rev. D **93**, 034503 (2016).

[51] S.-J. Dong and K.-F. Liu, Stochastic estimation with Z_2 noise, Phys. Lett. B **328**, 130 (1994).

[52] S. Bernardson, P. McCarty, and C. Thron, Monte Carlo methods for estimating linear combinations of inverse matrix entries in lattice QCD, Comput. Phys. Commun. **78**, 256 (1993).

[53] T. Harris, G. von Hippel, P. Junnarkar, H. B. Meyer, K. Ottnad, J. Wilhelm, H. Wittig, and L. Wrang, Nucleon isovector charges and twist-2 matrix elements with $N_f = 2 + 1$ dynamical Wilson quarks, Phys. Rev. D **100**, 034513 (2019).

[54] P. Korcyl and G. S. Bali, Non-perturbative determination of improvement coefficients using coordinate space correlators in $N_f = 2 + 1$ lattice QCD, Proc. Sci. LATTICE2016 (**2016**) 190 [arXiv:1609.09477].

[55] G. S. Bali, K. G. Chetyrkin, P. Korcyl, and J. Simeth, Non-perturbative determination of quark-mass independent improvement coefficients in $n_f = 2 + 1$ lattice QCD (to be published).

[56] G. S. Bali *et al.* (RQCD Collaboration), Nonperturbative renormalization in lattice QCD with three flavors of clover fermions: Using periodic and open boundary conditions, Phys. Rev. D **103**, 094511 (2021); **107**, 039901(E) (2023).

[57] G. Martinelli, C. Pittori, C. T. Sachrajda, M. Testa, and A. Vladikas, A general method for nonperturbative renormalization of lattice operators, Nucl. Phys. **B445**, 81 (1995).

[58] C. Sturm, Y. Aoki, N. H. Christ, T. Izubuchi, C. T. C. Sachrajda, and A. Soni, Renormalization of quark bilinear operators in a momentum-subtraction scheme with a nonexceptional subtraction point, Phys. Rev. D **80**, 014501 (2009).

[59] B. A. Kniehl and O. L. Veretin, Bilinear quark operators in the RI/SMOM scheme at three loops, Phys. Lett. B **804**, 135398 (2020).

[60] A. Bednyakov and A. Pikelner, Quark masses: N3LO bridge from RI/SMOM to $\overline{\mathrm{MS}}$ scheme, Phys. Rev. D **101**, 091501 (2020).

[61] B. A. Kniehl and O. L. Veretin, Moments $n = 2$ and $n = 3$ of the Wilson twist-two operators at three loops in the RI′/SMOM scheme, Nucl. Phys. **B961**, 115229 (2020).

[62] S. Sint, The chirally rotated Schrödinger functional with Wilson fermions and automatic O(a) improvement, Nucl. Phys. **B847**, 491 (2011).

[63] M. Dalla Brida, T. Korzec, S. Sint, and P. Vilaseca, High precision renormalization of the flavour nonsinglet Noether currents in lattice QCD with Wilson quarks, Eur. Phys. J. C **79**, 23 (2019).

[64] G. S. Bali, S. Collins, W. Söldner, and S. Weishäupl (RQCD Collaboration), Leading order mesonic and baryonic SU(3) low energy constants from $N_f = 3$ lattice QCD, Phys. Rev. D **105**, 054516 (2022).

[65] E. E. Jenkins and A. V. Manohar, Baryon chiral perturbation theory using a heavy fermion Lagrangian, Phys. Lett. B **255**, 558 (1991).

[66] J. Bijnens, H. Sonoda, and M. B. Wise, On the validity of chiral perturbation theory for weak hyperon decays, Nucl. Phys. **B261**, 185 (1985).

[67] T. Ledwig, J. Martin Camalich, L. S. Geng, and M. J. Vicente Vacas, Octet-baryon axial-vector charges and

SU(3)-breaking effects in the semileptonic hyperon decays, Phys. Rev. D **90**, 054502 (2014).

[68] C. C. Chang *et al.*, A per-cent-level determination of the nucleon axial coupling from quantum chromodynamics, Nature (London) **558**, 91 (2018).

[69] R. Gupta, Y.-C. Jang, B. Yoon, H.-W. Lin, V. Cirigliano, and T. Bhattacharya (PNDME Collaboration), Isovector charges of the nucleon from $2 + 1 + 1$-flavor lattice QCD, Phys. Rev. D **98**, 034503 (2018).

[70] M. F. M. Lutz, U. Sauerwein, and R. G. E. Timmermans, On the axial-vector form factor of the nucleon and chiral symmetry, Eur. Phys. J. C **80**, 844 (2020).

[71] M. Lüscher, Properties and uses of the Wilson flow in lattice QCD, J. High Energy Phys. 08 (2010) 071; 03 (2014) 92(E).

[72] M. Bruno, T. Korzec, and S. Schaefer, Setting the scale for the CLS $2 + 1$ flavor ensembles, Phys. Rev. D **95**, 074504 (2017).

[73] S. Aoki *et al.*, Review of lattice results concerning low-energy particle physics, Eur. Phys. J. C **77**, 112 (2017).

[74] M. Ademollo and R. Gatto, Nonrenormalization Theorem for the Strangeness Violating Vector Currents, Phys. Rev. Lett. **13**, 264 (1964).

[75] R. L. Workman *et al.* (Particle Data Group), Review of particle physics, Prog. Theor. Exp. Phys. **2022**, 083C01 (2022).

[76] L. Hayen, Standard model $\mathcal{O}(\alpha)$ renormalization of g_A and its impact on new physics searches, Phys. Rev. D **103**, 113001 (2021).

[77] V. Cirigliano, J. de Vries, L. Hayen, E. Mereghetti, and A. Walker-Loud, Pion-Induced Radiative Corrections to Neutron β Decay, Phys. Rev. Lett. **129**, 121801 (2022).

[78] Y. Aoki *et al.* (Flavour Lattice Averaging Group (FLAG)), FLAG review 2021, Eur. Phys. J. C **82**, 869 (2022).

[79] J. Liang, Y.-B. Yang, T. Draper, M. Gong, and K.-F. Liu (χQCD Collaboration), Quark spins and anomalous Ward identity, Phys. Rev. D **98**, 074505 (2018).

[80] M. González-Alonso and J. Martin Camalich, Isospin Breaking in the Nucleon Mass and the Sensitivity of β Decays to New Physics, Phys. Rev. Lett. **112**, 042501 (2014).

[81] N. Yamanaka, S. Hashimoto, T. Kaneko, and H. Ohki (JLQCD Collaboration), Nucleon charges with dynamical overlap fermions, Phys. Rev. D **98**, 054516 (2018).

[82] E. Shintani, K.-I. Ishikawa, Y. Kuramashi, S. Sasaki, and T. Yamazaki (PACS Collaboration), Nucleon form factors and root-mean-square radii on a $(10.8\ \mathrm{fm})^4$ lattice at the physical point, Phys. Rev. D **99**, 014510 (2019); **102**, 019902(E) (2020).

[83] N. Hasan, J. Green, S. Meinel, M. Engelhardt, S. Krieg, J. Negele, A. Pochinsky, and S. Syritsyn (LHPC Collaboration), Nucleon axial, scalar, and tensor charges using lattice QCD at the physical pion mass, Phys. Rev. D **99**, 114505 (2019).

[84] S. Park, R. Gupta, B. Yoon, S. Mondal, T. Bhattacharya, Y.-C. Jang, B. Jo'o, and F. Winter (NME Collaboration), Precision nucleon charges and form factors using $(2 + 1)$-flavor lattice QCD, Phys. Rev. D **105**, 054505 (2022).

[85] K. Ottnad, D. Djukanovic, T. Harris, H. B. Meyer, G. von Hippel, and H. Wittig, Improved analysis of nucleon isovector charges and twist-2 matrix elements on CLS $N_f = 2 + 1$ ensembles, Proc. Sci. LATTICE2021 (**2022**) 343 [arXiv:2110.10500].

[86] R. Tsuji, N. Tsukamoto, Y. Aoki, K.-I. Ishikawa, Y. Kuramashi, S. Sasaki, E. Shintani, and T. Yamazaki (PACS Collaboration), Nucleon isovector couplings in $N_f = 2+1$ lattice QCD at the physical point, Phys. Rev. D **106**, 094505 (2022).

[87] T. Bhattacharya, V. Cirigliano, S. Cohen, R. Gupta, H.-W. Lin, and B. Yoon (PNDME Collaboration), Axial, scalar and tensor charges of the nucleon from $2 + 1 + 1$-flavor lattice QCD, Phys. Rev. D **94**, 054508 (2016).

[88] E. Berkowitz *et al.*, An accurate calculation of the nucleon axial charge with lattice QCD, arXiv:1704.01114.

[89] C. Alexandrou, S. Bacchio, M. Constantinou, J. Finkenrath, K. Hadjiyiannakou, K. Jansen, G. Koutsou, and A. Vaquero Aviles-Casco (ETM Collaboration), Nucleon axial, tensor, and scalar charges and σ-terms in lattice QCD, Phys. Rev. D **102**, 054517 (2020).

[90] A. Walker-Loud *et al.*, Lattice QCD determination of g_A, Proc. Sci. CD2018 (**2020**) 020 [arXiv:1912.08321].

[91] Y.-C. Jang, R. Gupta, T. Bhattacharya, B. Yoon, and H.-W. Lin (PNDME Collaboration), Nucleon isovector axial form factors, arXiv:2305.11330.

[92] H.-W. Lin, Nucleon structure and hyperon form factor from lattice QCD, arXiv:0707.3844.

[93] C. Alexandrou, K. Hadjiyiannakou, K. Jansen, and C. Kallidonis, Sigma-terms and axial charges for hyperons and charmed baryons, Proc. Sci. Lattice2013 (**2014**) 279 [arXiv:1404.6355].

[94] M. Göckeler, P. Hägler, R. Horsley, Y. Nakamura, D. Pleiter, P. E. L. Rakow, A. Schäfer, G. Schierholz, H. Stüben, and J. M. Zanotti (QCDSF-UKQCD Collaboration), Baryon axial charges and momentum fractions with $N_f = 2 + 1$ dynamical fermions, Proc. Sci. LATTICE2010 (**2010**) 163 [arXiv:1102.3407].

[95] K.-S. Choi, W. Plessas, and R. F. Wagenbrunn, Axial charges of octet and decuplet baryons, Phys. Rev. D **82**, 014007 (2010).

[96] X. Y. Liu, D. Samart, K. Khosonthongkee, A. Limphirat, K. Xu, and Y. Yan, Axial charges of octet and decuplet baryons in a perturbative chiral quark model, Phys. Rev. C **97**, 055206 (2018).

[97] R. Qi, J.-B. Wang, G. Li, C.-S. An, C.-R. Deng, and J.-J. Xie, Investigations on the flavor-dependent axial charges of the octet baryons, Phys. Rev. C **105**, 065204 (2022).

[98] G.-S. Yang and H.-C. Kim, Hyperon semileptonic decay constants with flavor SU(3) symmetry breaking, Phys. Rev. C **92**, 035206 (2015).

[99] F. Herren and M. Steinhauser, Version 3 of RunDec and CRunDec, Comput. Phys. Commun. **224**, 333 (2018).

[100] M. Bruno, M. Dalla Brida, P. Fritzsch, T. Korzec, A. Ramos, S. Schaefer, H. Simma, S. Sint, and R. Sommer (ALPHA Collaboration), QCD Coupling from a Nonperturbative Determination of the Three-Flavor Λ Parameter, Phys. Rev. Lett. **119**, 102001 (2017).

[101] P. A. Baikov, K. G. Chetyrkin, and J. H. Kühn, Five-Loop Running of the QCD Coupling Constant, Phys. Rev. Lett. **118**, 082002 (2017).

[102] P. A. Baikov, K. G. Chetyrkin, and J. H. Kühn, Five-loop fermion anomalous dimension for a general gauge group

from four-loop massless propagators, J. High Energy Phys. 04 (2017) 119.

[103] Y. Schröder and M. Steinhauser, Four-loop decoupling relations for the strong coupling, J. High Energy Phys. 01 (2006) 051.

[104] T. Liu and M. Steinhauser, Decoupling of heavy quarks at four loops and effective Higgs-fermion coupling, Phys. Lett. B **746**, 330 (2015).

[105] P. Marquard, A. V. Smirnov, V. A. Smirnov, M. Steinhauser, and D. Wellmann, $\overline{\mathrm{MS}}$-on-shell quark mass relation up to four loops in QCD and a general SU(N) gauge group, Phys. Rev. D **94**, 074025 (2016).

[106] M. Abramczyk, T. Blum, T. Izubuchi, C. Jung, M. Lin, A. Lytle, S. Ohta, and E. Shintani (RBC and UKQCD Collaborations), Nucleon mass and isovector couplings in $2+1$-flavor dynamical domain-wall lattice QCD near physical mass, Phys. Rev. D **101**, 034510 (2020).

[107] L. Liu, T. Chen, T. Draper, J. Liang, K.-F. Liu, G. Wang, and Y.-B. Yang (χQCD Collaboration), Nucleon isovector scalar charge from overlap fermions, Phys. Rev. D **104**, 094503 (2021).

[108] Z. Fodor, C. Hoelbling, S. Krieg, L. Lellouch, T. Lippert, A. Portelli, A. Sastre, K. K. Szabo, and L. Varnhorst, Up and Down Quark Masses and Corrections to Dashen's Theorem from Lattice QCD and Quenched QED, Phys. Rev. Lett. **117**, 082001 (2016).

[109] S. Borsanyi *et al.*, *Ab initio* calculation of the neutron-proton mass difference, Science **347**, 1452 (2015).

[110] D. Horkel, Y. Bi, M. Constantinou, T. Draper, J. Liang, K.-F. Liu, Z. Liu, and Y.-B. Yang (χQCD Collaboration), Nucleon isovector tensor charge from lattice QCD using chiral fermions, Phys. Rev. D **101**, 094501 (2020).

[111] T. Bhattacharya, V. Cirigliano, S. Cohen, R. Gupta, A. Joseph, H.-W. Lin, and B. Yoon (PNDME Collaboration), Iso-vector and iso-scalar tensor charges of the nucleon from lattice QCD, Phys. Rev. D **92**, 094511 (2015).

[112] C. Alexandrou *et al.* (ETM Collaboration), Moments of the nucleon transverse quark spin densities using lattice QCD, Phys. Rev. D **107**, 054504 (2023).

[113] M. Anselmino, M. Boglione, U. D'Alesio, S. Melis, F. Murgia, and A. Prokudin, Simultaneous extraction of transversity and Collins functions from new SIDIS and e^+e^- data, Phys. Rev. D **87**, 094019 (2013).

[114] Z.-B. Kang, A. Prokudin, P. Sun, and F. Yuan, Extraction of quark transversity distribution and Collins fragmentation functions with QCD evolution, Phys. Rev. D **93**, 014009 (2016).

[115] M. Radici and A. Bacchetta, First Extraction of Transversity from a Global Analysis of Electron-Proton and Proton-Proton Data, Phys. Rev. Lett. **120**, 192001 (2018).

[116] J. Benel, A. Courtoy, and R. Ferro-Hernandez, A constrained fit of the valence transversity distributions from dihadron production, Eur. Phys. J. C **80**, 465 (2020).

[117] J. Cammarota, L. Gamberg, Z.-B. Kang, J. A. Miller, D. Pitonyak, A. Prokudin, T. C. Rogers, and N. Sato (JAM Collaboration), Origin of single transverse-spin asymmetries in high-energy collisions, Phys. Rev. D **102**, 054002 (2020).

[118] W. N. Cottingham, The neutron proton mass difference and electron scattering experiments, Ann. Phys. (N.Y.) **25**, 424 (1963).

[119] R. F. Dashen, Chiral $\mathrm{SU}(3)\times\mathrm{SU}(3)$ as a symmetry of the strong interactions, Phys. Rev. **183**, 1245 (1969).

[120] J. Gasser, A. Rusetsky, and I. Scimemi, Electromagnetic corrections in hadronic processes, Eur. Phys. J. C **32**, 97 (2003).

[121] D. Giusti, V. Lubicz, C. Tarantino, G. Martinelli, F. Sanfilippo, S. Simula, and N. Tantalo (RM123 Collaboration), Leading isospin-breaking corrections to pion, kaon and charmed-meson masses with twisted-mass fermions, Phys. Rev. D **95**, 114504 (2017).

[122] A. Bazavov *et al.* (Fermilab Lattice and MILC Collaborations), B- and D-meson leptonic decay constants from four-flavor lattice QCD, Phys. Rev. D **98**, 074512 (2018).

[123] S. Basak *et al.* (MILC Collaboration), Lattice computation of the electromagnetic contributions to kaon and pion masses, Phys. Rev. D **99**, 034503 (2019).

[124] J. Gasser, H. Leutwyler, and A. Rusetsky, On the mass difference between proton and neutron, Phys. Lett. B **814**, 136087 (2021).

[125] M. G. Endres, A. Shindler, B. C. Tiburzi, and A. Walker-Loud, Massive Photons: An Infrared Regularization Scheme for Lattice $\mathrm{QCD}+\mathrm{QED}$, Phys. Rev. Lett. **117**, 072002 (2016).

[126] D. A. Brantley, B. Joó, E. V. Mastropas, E. Mereghetti, H. Monge-Camacho, B. C. Tiburzi, and A. Walker-Loud, Strong isospin violation and chiral logarithms in the baryon spectrum, arXiv:1612.07733.

[127] R. Horsley *et al.* (CSSM-QCDSF-UKQCD Collaboration), Isospin splittings in the decuplet baryon spectrum from dynamical $\mathrm{QCD}+\mathrm{QED}$, J. Phys. G **46**, 115004 (2019).

[128] R. Horsley, J. Najjar, Y. Nakamura, H. Perlt, D. Pleiter, P. E. L. Rakow, G. Schierholz, A. Schiller, H. Stüben, and J. M. Zanotti (QCDSF-UKQCD Collaboration), Lattice determination of Sigma-Lambda mixing, Phys. Rev. D **91**, 074512 (2015).

[129] S. Dürr *et al.*, Lattice Computation of the Nucleon Scalar Quark Contents at the Physical Point, Phys. Rev. Lett. **116**, 172001 (2016).

[130] N. Salone, P. Adlarson, V. Batozskaya, A. Kupsc, S. Leupold, and J. Tandean, Study of CP violation in hyperon decays at super-charm-tau factories with a polarized electron beam, Phys. Rev. D **105**, 116022 (2022).

[131] P. L. J. Petrak, G. Bali, S. Collins, J. Heitger, D. Jenkins, and S. Weishäupl, Sigma terms of the baryon octet in $N_\mathrm{f}=2+1$ QCD with Wilson quarks, Proc. Sci. LATTICE2022 (**2023**) 112 [arXiv:2301.03871].

[132] Jülich Supercomputing Centre, JUWELS: Modular tier-$0/1$ supercomputer at the Jülich Supercomputing Centre, J. Large-Scale Res. Facil. **5**, A135 (2019).

[133] Jülich Supercomputing Centre, JURECA: Modular supercomputer at Jülich Supercomputing Centre, J. Large-Scale Res. Facil. **4**, A132 (2018).

[134] Jülich Supercomputing Centre, HDF cloud—Helmholtz data federation cloud resources at the Jülich Supercomputing Centre, J. Large-Scale Res. Facil. **5**, A137 (2019).

[135] R. G. Edwards and B. Joó (SciDAC, LHP, and UKQCD Collaborations), The Chroma software system for lattice QCD, Nucl. Phys. B, Proc. Suppl. **140**, 832 (2005).

[136] S. Heybrock, M. Rottmann, P. Georg, and T. Wettig, Adaptive algebraic multigrid on SIMD architectures, Proc. Sci. LATTICE2015 (**2016**) 036 [arXiv:1512.04506].

[137] P. Georg, D. Richtmann, and T. Wettig, DD-αAMG on QPACE 3, EPJ Web Conf. **175**, 02007 (2018).

[138] A. Frommer, K. Kahl, S. Krieg, B. Leder, and M. Rottmann, Adaptive aggregation based domain decomposition multigrid for the lattice Wilson Dirac operator, SIAM J. Sci. Comput. **36**, A1581 (2014).

[139] M. Lüscher, Deflation acceleration of lattice QCD simulations, J. High Energy Phys. 12 (2007) 011.

[140] J. D. Hunter, Matplotlib: A 2d graphics environment, Comput. Sci. Eng. **9**, 90 (2007).

[141] A. Agadjanov, D. Djukanovic, G. von Hippel, H. B. Meyer, K. Ottnad, and H. Wittig, The nucleon sigma terms with $N_f = 2 + 1$ O(a)-improved Wilson fermions, arXiv:2303.08741.